Title

Experimental and Numerical Study of Mixed-convection Magnetohydrodynamic (MHD) Flows for Liquid-metal Fusion Blankets

Author

Yan, Yi

Publication Date

2024

Peer reviewed|Thesis/dissertation

UNIVERSITY OF CALIFORNIA

Los Angeles

Experimental and Numerical Study of Mixed-convection Magnetohydrodynamic (MHD) Flows for Liquid-metal Fusion Blankets

A dissertation submitted in partial satisfaction of the

requirements for the degree Doctor of Philosophy

in Mechanical Engineering

by

Yi Yan

2024

ABSTRACT OF THE DISSERTATION

Experimental and Numerical Study

of Mixed-convection Magnetohydrodynamics (MHD) Flows

for Liquid-metal Fusion Blankets

by

Yi Yan

Doctor of Philosophy in Mechanical Engineering

University of California, Los Angeles, 2024

Professor Mohamed A. Abdou, Chair

The liquid-metal fusion blanket constitutes a pivotal element in the infrastructure of magnetic field confined fusion nuclear power plants, undertaking a multifaceted role crucial to their operation. Its responsibilities span from breeding tritium, essential fuel for fusion reactions, to converting the energy from high-energy neutrons and plasma into electricity, while also shielding structural components from the impact of high-energy species produced during fusion processes. Specifically engineered for this purpose, a liquid metal fusion blanket employs materials such as lithium or lithium alloys, serving as coolants and breeding materials simultaneously. Within the domain of liquid-metal (LM) blankets, mixed-convection presents a significant challenge, emerging as the dominant flow phenomenon in most fusion LM blanket designs. The magnetohydrodynamics (MHD) flows of liquid breeders, like PbLi, within blanket

conduits experience notable buoyancy forces due to heightened temperature gradients resulting from intense heat loads. The intricate interplay of MHD effects and buoyant forces gives rise to strongly coupled phenomena. Understanding and predicting the complex flow behaviors arising from the interaction of these multiple effects necessitate both experimental data and numerical investigations of three-dimensional mixed-convection MHD flows for advancing LM blanket designs.

Chapter two of this thesis outlines the establishment of the MaPLE-U facility, dedicated to high-temperature liquid metal experiments under intense magnetic fields and various flow orientations with respect to gravity. Subsequently, the first experimental dataset is presented, focusing on PbLi, a prominent blanket breeding candidate, to elucidate mixed-convection MHD flow behaviors and heat transfer phenomena. The findings challenge the assumption of complete flow laminarization under strong MHD effects, widely adopted in LM MHD R&D strategy, emphasizing the need for simultaneous consideration of multiple effects.

Chapter three delves into numerical investigations employing COMSOL Multiphysics, where flow predictions are validated against analytical solutions, benchmarked experimental data, and results from other MHD codes. A novel MHD-heat transfer flow model is developed to address the lack of numerical simulation tools for wall-bounded fully developed flows concurrently coupling MHD flow and heat transfer equations under harsh nuclear fusion reactor conditions ($Ha \sim 10^4, Gr \sim 10^{11}$). Building upon this groundwork, chapter four provides further insights into mixed-convection MHD flows within complex LM blanket geometries under fusion-relevant conditions, showcasing the versatility and computational accuracy of the COMSOL Multiphysics platform, particularly in scenarios surpassing existing experimental and numerical studies.

The dissertation of Yi Yan is approved.

Jeffrey D. Eldredge

Adrienne G. Lavine

Xiaolin Zhong

Mohamed A. Abdou, Committee Chair

University of California, Los Angeles

2024

TABLE OF CONTENTS

LIST OF FIGURES

LIST OF TABLES

VITA

2016 – Present	**Ph.D. in Mechanical Engineering**
	University of California, Los Angeles (UCLA)
2013 – 2016	**M.S. in Aerospace Engineering**
	University of California, Los Angeles (UCLA)
2011 – 2013	**M.S. in Mechanical Engineering**
	University of Southern California
2007 – 2011	**B.S. in Mechanical Engineering**
	Shanghai Jiao Tong University, China

PEER-REVIEWED PUBLICATIONS

[1] Y, Yan, A. Ying, and M. Abdou, "Numerical study of magneto-convection flows in a complex prototypical liquid-metal fusion blanket geometry," *Fusion Engineering and Design*. **159,** 111688 (2020)

[2] S. Smolentsev, T. Rhodes, Y. Yan, A. Tassoune, C. Mistrangelo, L. Bühler, and F. R. Urgorri, "Code-to-Code Comparison for a PbLi Mixed-Convection MHD Flow," *Fusion Science and Techonoloty*, **76**, 653-669, (2020)

[3] S. Smolentsev, M. Abdou, C. Courtessole, G. Pulugundla, FC. Li, N. Morley, R. Munipali, P. Huang, C. Kaczynski, J. Young, T. Rhodes, and Y. Yan, "Review of Recent MHD Activities for Liquid Metal Blankets in the US," *Magnetohydrodynamics*, **53(2)**, 411-422, (2017)

CHAPTER ONE: INTRODUCTION

1.1 Background

In the realm of fusion reactors, the breeding blanket stands out as a pivotal component, undertaking the crucial responsibilities of safeguarding the magnetic coils and vacuum vessels from unbearable radiation doses. Its role extends to the absorption of fast neutrons, converting their energy into heat, and the breeding of tritium—a key reactant essential for achieving self-sustainable fusion reactions. Over the past four decades, a variety of blanket concepts have been proposed globally, with liquid metal (LM) and solid breeder concepts emerging as primary candidates, extensively explored in major fusion programs. Additional concepts, such as the hybrid blanket advocated by India and molten salts concepts pursued by Japan, contribute to the diverse landscape of potential solutions [1].

Comparative analysis reveals that liquid metal blanket concepts offer significant advantages over alternative candidates. They present the potential for higher power density and significantly reduced susceptibility to radiation damage. Within the domain of liquid metal concepts, various options are considered based on different coolant systems. However, the consistent element across these concepts is the use of lithium or lithium-containing alloys (such as PbLi) as breeder materials. Lithium's role is critical for tritium breeding, while PbLi serves as the neutron multiplier in corresponding nuclear reactions.

Despite these advantages, the presence of strong plasma-confining magnetic fields introduces formidable challenges. The highly electrically conducting flow of liquid metal undergoes strong Magnetohydrodynamics (MHD) effects, presenting feasibility issues across all liquid metal blanket concepts [1]. Beyond MHD effects, the flowing liquid metals in blanket conduits contend with robust buoyancy forces linked to high temperature gradients arising from

steep volumetric and/or surface heat loads. The interaction between MHD and buoyancy forces necessitates a thorough investigation, as MHD mixed convection could emerge as the dominant flow phenomenon in most fusion LM blanket designs. Moreover, many previous analyses, focused on the study of solitary effects, often neglect interactions between multiple factors, rendering them insufficient for predicting flow behavior in LM fusion blankets.

1.2 Literature Reviews

In the exploration of Magnetohydrodynamics (MHD) flows coupled with heat transfer effects, the concurrent influence of buoyancy and electromagnetic forces was initially examined in the 1960s. Pioneering works by Y. Mori [2] and E.M. Sparrow, and R.D. Cess [3] focused on the flow between vertical plates, revealing that applied magnetic fields significantly impact heat transfer in laminar flows. Building on this, H. K. Yang and C. P. Yu [4] studied the effect of imposed magnetic fields on entrance length in MHD channel flows in 1973. Their findings indicated a substantial reduction in the development length of velocity with an applied transverse field, while the temperature boundary layer development remained largely unaffected.

Transitioning into the mid-1970s, researchers expanded their investigations to three-dimensional MHD flows in cubic enclosures with natural convection. Experimental studies by I. Michiyoshi et al. [5], M. Seki et al. [6], O. Takahashi et al. [7], K. Okada and H. Ozoe [8], and T. Tagawa and H. Ozoe [9] explored the effect of imposed magnetic fields on heat transfer rates. Concurrently, numerical studies by N. O. Weiss [10] delved into the development of flow instability, and H. Ozoe et al. [11] tested a two-equation turbulence model. H. Ozoe and K. Okada [12], R. Mößner, and U. Müller [13] analyzed the effect of the orientation of applied magnetic fields.

The first two decades in 21st century marked a shift towards the numerical exploration of MHD flows with mixed-convection effects in vertical channel flow. Notable contributions include studies by S. Smolentsev et al. [14], G. Sposito et al. [15], N. Vetcha et al. [16-17], H. Saleh and I. Hashim [18], C. Mistrangelo and L. Bühler [19], H. Sun et al. [20], R. Alizadeh et al. [21], A. Gul et al. [22], and X. Zhang and O. Zikanov [23]. While three-dimensional MHD flows garnered experimental attention, with studies by I. A. Melnikov et al. [24] and I. R. Kirillov et al. [25] in a vertical round tube and a vertical rectangular duct, respectively, numerical simulations in vertical round tubes were conducted by O. Zikanov and Y. Listratov [26]. Additionally, X. Zhang and O. Zikanov [27,28] simulated mixed-convection MHD flows in horizontal ducts.

To date, numerical data for 3D mixed-convection MHD flows in the harsh environment relevant to fusion reactors remains unpublished, and laboratory experiments investigating such flows have exclusively utilized room temperature liquid metal. Moreover, prior studies have predominantly concentrated on uncomplicated geometries, such as ducts and pipes, characterized by low to moderate flow parameters ($Gr < 10^8, Ha < 10^3$). Particularly noteworthy is the absence of exploration into the dynamics of mixed convection MHD flows within fusion LM blankets at elevated flow parameters ($Gr \sim 10^{12}, Ha \sim 10^4$). This discernible knowledge gap underscores the imperative for additional research endeavors aimed at unraveling the intricate complexities of these flows within the specific context of fusion energy applications.

1.3 Objectives and Scopes

One of the primary aims of this thesis research is to leverage the experimental capabilities of the recently constructed MaPLE-U facility to systematically observe and characterize mixed convection MHD flow behaviors across an extensive spectrum of flow parameters. This investigation centers specifically on vertical downward duct flows featuring electrically

conducting walls and a uniform surface heating scheme. The constraints on heating power and applied magnetic field strength are set at $10\ \mathrm{W/cm^2}$ and 1.5 T, respectively. Additionally, the scope of this research extends to advancing diagnostic instrumentation, notably the development of a novel translational probing scheme designed for the measurement of local quantities.

In the domain of numerical investigations concerning mixed-convection MHD flows in Liquid Metal (LM) blankets, the research comprises three essential components: first, the validation and comparison of 3D flow predictions from a commercial simulation software, COMSOL Multiphysics, against experimental data and other computational MHD codes; second, the establishment of a groundbreaking model to simultaneously compute the heat transfer equation and MHD equations for fully developed flows, contributing a novel perspective to the field; third, the assessment of the modeling capability of COMSOL Multiphysics for simulating 3D mixed-convection MHD flows in simple geometries, focusing on blanket-relevant dimensionless MHD and heat transfer parameters.

The overarching goal is to conduct 3D computations in COMSOL at blanket conditions expected in fusion DEMO and reactors, subsequently comparing the results with available experimental data and those obtained using the HIMAG code, which are presently accessible at $Gr \sim 10^8, Ha = 660$. The realization of this ambitious goal is contingent on the computational capabilities available at UCLA, as achieving simultaneous high Gr and Ha values necessitates sophisticated computational resources.

CHAPTER TWO: EXPERIMENTAL FACILITY AND FIRST EXPERIMENTAL STUDY

For 30 years of investigating fusion LM blanket designs, the prevailing treatment of MHD buoyant flows involved categorizing them within a laminar regime in the presence of strong magnetic fields. This conventional understanding held that any fluctuations would be dampened and dissipated within thin Hartmann boundary layers. However, the assumption of a singular effect was challenged in many publications such as N. Vetcha et al. [29], revealing that robust buoyancy forces, arising from steep nuclear heating and temperature gradients, could surpass damping effects, giving rise to an unstable mixed convection flow regime. The implications of such flow instabilities on critical behaviors (pressure drops, flow reversal, "hot spots") and transport phenomena (heat and mass transport, corrosion) in all LM blanket systems cannot be understated. Consequently, there arises a crucial need for the observation and characterization of mixed-convection MHD phenomena, aiming to unveil new occurrences across a diverse range of flow parameters through experimental endeavors.

2.1 Introduction to Experimental Facility

In 2011, the establishment of the MaPLE facility (Magnetohydrodynamics PbLi Experiment) at UCLA marked the commencement of efforts to conduct comprehensive experiments on mixed convection MHD flows [30,31]. Despite various iterations aimed at enhancing the practicality of the original loop, the fixed horizontal orientation of the flow test section, dictated by spatial constraints within the magnetic field zone, imposes limitations on experimental research. This constraint inhibits addressing the interplay of multiple MHD and buoyancy effects with diverse flow orientations, analogous to distinct sectors within a fusion reactor's breeding blanket.

Recognizing these constraints, significant enhancements led to the transformation of the MaPLE facility into MaPLE-U. The major modifications include the replacement of the magnet-positional frame with a hydraulic lifting and tilting system (depicted in Picture A in Appendix A). This upgrade enables a vertical lift of up to 2 m and a tilt angle ranging from -90° to 90°, facilitating experiments with various flow angles relative to gravity. The second substantial change involves the complete reconstruction of the MaPLE-U PbLi flow loop (illustrated in Picture B in Appendix A), achieving the maximum operating temperature from 350 °C to 500 °C to align with the LM breeding blanket design requirements [31]. This upgrade also entails an increase in the maximum allowable pressure from 0.2 MPa to 0.9 MPa and in the maximum flow rate from 35 to 120 l/min.

Further improvements (shown in pictures in Appendix A) extend to the data acquisition and control system, ensuring precise temperature control across different loop segments while effectively managing other processes, including flow rate, heat exchange, and loop pressure levels. Designed with versatility in mind, the MaPLE-U facility can accommodate experiments with replaceable test articles. Consequently, the construction of the test section, along with the associated instrumentation, is treated as a separate facet and is detailed in the subsequent section.

2.2 First Experimental Study

2.2.1 Test section

Inside the magnetic field enclosure, nestled between two parallel coils, resides a gap domain measuring 15 cm x 15 cm x 80 cm. This region boasts a consistent magnetic field with a strength reaching up to 1.8 T. The MaPLE-U loop incorporates a 2-meter long, 5 cm square stainless-steel duct with a 2 mm wall thickness that traverses this magnetic gap (refer to Picture D in Appendix A). On the external side wall, running parallel to the external magnetic field

direction, three strip heaters (20 cm x 5 cm each) have been affixed. Calorimetry measurements are conducted using two temperature integrators, positioned 7 cm upstream and downstream of the heaters.

Within the heating zone, at four distinct axial locations on both Hartmann walls (oriented perpendicular to the external magnetic field), a total of forty thermocouples (five per Hartmann wall per axial location) are strategically placed. These thermocouples facilitate the measurement of temperature distribution along the heated direction at the exterior surface of the duct. This comprehensive setup allows for monitoring and analysis of the thermal behavior within the magnetized environment of the MaPLE-U loop.

2.2.2 First Experimental Results

During the initial 6 months of operation, the integrated MaPLE-U facility underwent a comprehensive commissioning test. The primary objective was to assess the functionality of each component within this newly constructed facility, allowing for subsequent iterations and improvements. As part of this phase, the test article integrated into the loop did not feature instrumentation for measuring local variables within the flow, apart from temperature integrators. Throughout this period, experiments focused on vertical downward mixed-convection MHD flows, incorporating input variables such as inlet velocity (U_0), surface heating power (q''), and external magnetic field strength (B_0). The range of input parameters explored in this experiment is detailed in Table 1 below.

***Table 1**: Operating Parameter Map for Mixed Convection MHD Flow in MaPLE-U Loop*

q''	U_0 (cm/s) at $B_0 = 0$ T	U_0 (cm/s) at $B_0 = 0.53$ T	U_0 (cm/s) at $B_0 = 1.0$ T
$2\ W/cm^2$	0.64	0.64	0.68
	1.78	1.76	1.86
	2.70	Missing	2.56
	3.63	3.90	3.81
	4.66	4.66	4.70
	9.63	9.71	9.63
	14.55	14.53	14.68
$4\ W/cm^2$	0.10	0.58	0.63
	1.70	1.80	1.68
	2.59	2.59	2.69
	3.60	3.77	3.63
	4.74	4.54	4.60
	9.60	9.35	9.80
	14.59	14.62	14.55
$5\ W/cm^2$	0.73	0.30	0.71
	1.64	1.73	1.73
	2.63	2.59	2.70
	3.63	3.73	3.72
	4.68	4.60	4.69
	9.73	9.55	9.61
	14.66	14.52	14.47

2.2.2.1 Temperature distribution on Hartmann walls

The instantaneous temperatures at forty locations on both Hartmann walls are acquired with sampling rate of 60 samples per second for a period of 60 seconds for each input variable combination. The corresponding temporal averaged temperature distributions along the flow direction are calculated and plotted in Fig. 1(a)-(c) below.

In laminar duct flows with a single-side surface heating scheme, the expected behavior of the temporally averaged temperature distribution along the flow direction is a linear increase within the heating area due to energy conservation. However, this trend may be interrupted by

flow reversal induced by a sufficiently strong buoyancy opposing force, leading to a maximal temperature peak inside the heating zone while maintaining the same surface heating power.

***Figure 1**: Time Averaged Temperature Measurement on Hartmann Walls of MaPLE-U First Experiment Data*

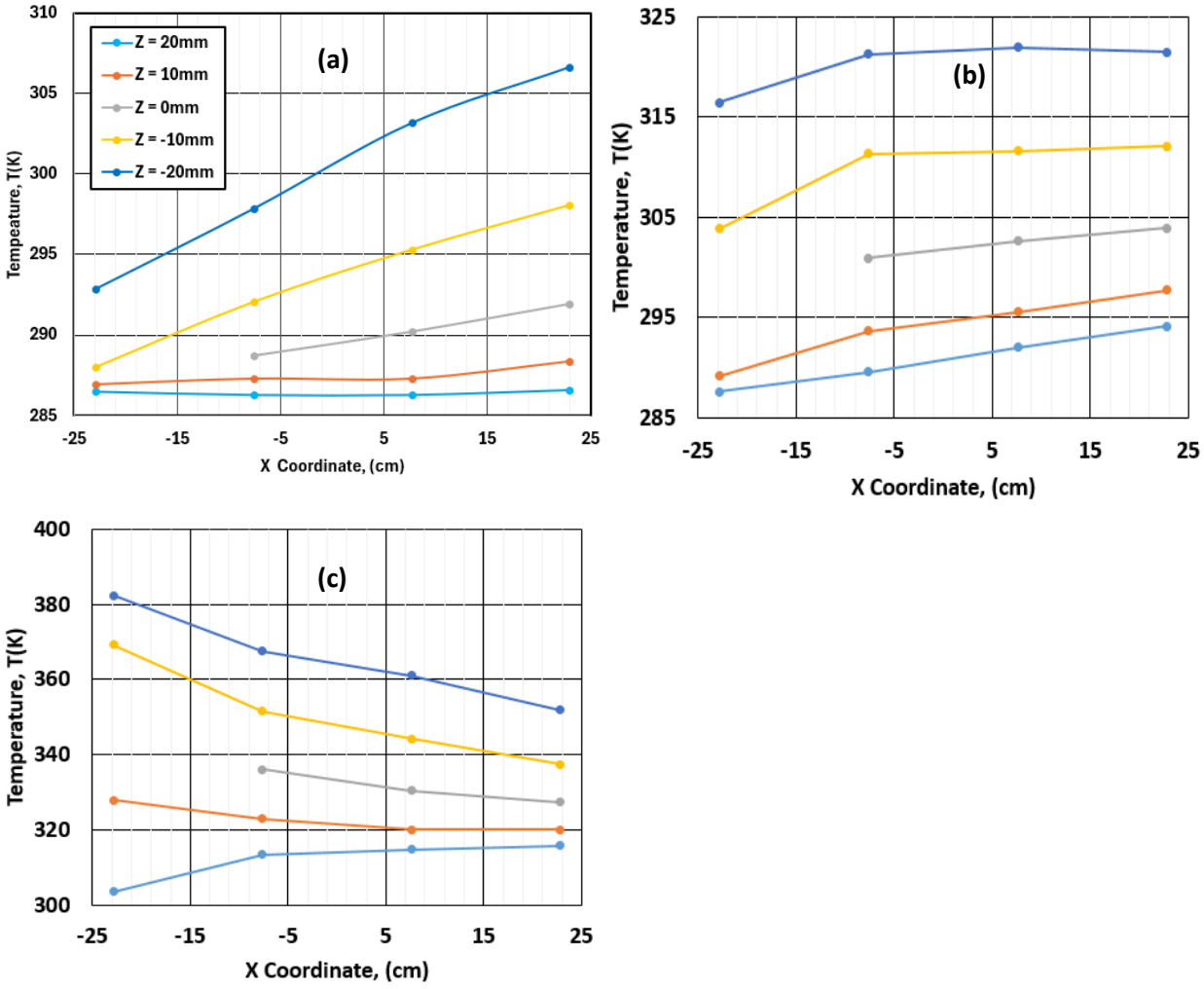

Note. Time averaged temperature measurements on Hartmann walls at different flow parameters (a) $U_0 = 2$ cm/s, $B_0 = 0.53$ T, $q'' = 2$ W/cm^2, (b) $U_0 = 1$ cm/s, $B_0 = 0.53$ T, $q'' = 2$ W/cm^2, (c) $U_0 = 1$ cm/s, $B_0 = 0.53$ T, $q'' = 4$ W/cm^2. Flow direction is from negative X to positive X location and X = 0 mm is the center of the heating zone.

Such reversal and the associated trend are observed in this experiment without the magnetic field strength and with a strength of 0.53 T. With a higher magnetic field strength, the occurrence of flow reversal requires a much stronger buoyancy effect to overcome the additional Magnetohydrodynamics (MHD) force. This feature is also evident in this experiment where the location of the maximal temperature peak is pushed downstream with the increase of external magnetic field strength, and no flow reversal (characterized by the temperature distribution) is observed with a strength of 1.0 T. The flow regime (observance of flow reversal) on the full parameter map is summarized in Chart 1-3 in Appendix B.

Another notable feature of MHD flow in an electrically insulating duct is the quasi-two-dimensionality, which suppresses flow variation in the direction of the applied magnetic field, resulting in a uniform flow distribution along this direction, except for the steep velocity slope within thin Hartmann boundary layers. In the case of electrically conducting ducts, as observed in this experiment, despite the formation of high-velocity jets near Hartmann boundary layers that disrupt the uniformity of flow along the magnetic field direction, the flow distribution remains symmetric with respect to the center plane perpendicular to the applied magnetic field direction when the MHD effect is strong. Consequently, the temperature distribution on the two Hartmann walls is expected to be increasingly identical with enhanced magnetic field strength. However, under weak MHD effects, the flow is susceptible to various impacts, including the configuration of the upstream temperature integrator and the non-uniformity of the heating flux of strip heaters, causing non-symmetric variations in flow and temperature distribution across the duct perpendicular to the heating flux direction.

Indeed, this symmetry formation and breakage feature is captured in this experiment. At no magnetic field, the temperature distribution on the two Hartmann walls remains mostly

identical at high inlet velocities, while this symmetry is disrupted at the site of non-monotonous change of the axial temperature distribution in cases of transitional flow and reversal flow (as outlined in Table B.1 in Appendix B). However, with the introduction of magnetic fields, the non-symmetric flow variation is significantly dampened by the MHD effect, resulting in well-matched temperature distributions on the two Hartmann walls, even when flow reversal is clearly captured in cases with an applied magnetic field of 0.53 T (as detailed in Table B.2 in Appendix B).

2.2.2.2 Thermal Energy Conservation Balance in the Heating Region

The thermal energy balance in the heating region is estimated through the integral form of thermal energy conservation equation of incompressible flow (Eq. 1). The rate of change in thermal

$$\rho_0 C_p \left(\iiint \frac{dT}{dt} dV + \iint T\vec{u} \cdot \vec{n}\, dA\right) = \iint (\overrightarrow{q''} \cdot \vec{n}) dA + Q_{volume} + Q_{loss} \quad (1)$$

energy in this equation (first term) approximately vanishes when the flow development time in the test article is sufficiently long and the temperature measurements on the Hartmann walls reach the statistical steady state. The second term in this equation is the difference in net thermal energy carried by the fluid in the control volume bounded by upstream and downstream cross section planes where the temperature integrators are located. The third term denotes the thermal energy gained by the surface heating scheme and the last two terms indicate the volumetric energy gain due to viscous and joule heating mechanisms, and energy loss through the structural walls as the thermal insulating condition there is not exactly satisfied. In the characterization of thermal energy balance in this experiment, the volumetric energy gain and heating loss are neglected so that Eq. 1 is then simplified as

$$-\iint u(y,z)T(y,z)dA|_{upstream} + \iint u(y,z)T(y,z)dA|_{downstream} = \frac{q_0'' A_q}{\rho_0 C_p} \quad (2)$$

where q_0'' is the uniform heating flux, $A_q$is the heating area, and $u(y,z)$, $T(y,z)$ are the axial velocity and temperature distributions respectively on the planes where temperature integrators are installed. The thermal energy conservation balance in this experiment is evaluated by comparing the difference of bulk temperature $\bar{T}$, defined in Eq. 3 between two temperature integrator planes.

$$\bar{T} = \frac{\iint u(y,z)T(y,z)dA}{\iint u(y,z)dA} = \frac{\iint u(y,z)T(y,z)dA}{u_0 A_c} \quad (3)$$

In this experiment, with the same data acquisition procedure as in the Hartmann wall temperature measurement, upstream and downstream temperature fields are temporally averaged and applied in Eq. 3. The axial velocity fields on both planes are far from the heating zone and therefore considered fully developed flow condition in which the exact solutions are available through the MHD model developed in Chapter 3.3. Consequently, the bulk temperature difference in the experiment is calculated using temperature measurements and explicit velocity field solutions as shown in Eq. 4.

$$\Delta\bar{T}_{theoretical} = \bar{T}|_{downstream} - \bar{T}|_{upstream} = \frac{q_0'' A_q}{\rho_0 C_p u_0 A_c} \quad (4)$$

This value is then plotted in Fig. 2 depicting variations in inlet velocity at different surface heating fluxes and external magnetic field strengths and is compared against theoretical values. The anticipated trend is a decrease in the bulk temperature difference with an increase in inlet velocity, owing to enhanced convective heat transfer near the external heating surface. However, at low inlet velocities, the convective heat transfer effect may be suppressed or even altered, particularly when the flow near the heating surface becomes stagnant or undergoes reversal, leading to higher thermal energy loss through the structural walls. Consequently, the bulk

temperature difference in this experiment is notably lower than the theoretical value at slow inlet flow rates. Specifically, this variation exceeds 10% when the inlet velocity is below 3 cm/s, and 2 cm/s with external magnetic field strengths of 0 T and 0.53 T, respectively. This trend aligns with the occurrence of flow reversal inside the heating zone. When the external magnetic field strength is further increased to 1 T, it is expected that the bulk temperature difference will approach the theoretical value even at low velocity situations, as no reversed flow is formed. However, a variation of at least 10% persists across all flow rate inputs, indicating that the usage of a fully developed MHD flow profile may not accurately represent the velocity distribution in the experiment. This discrepancy is attributed to the fact that the thermocouple locations are not near the boundary layers, resulting in velocity field values smaller than the inlet velocity, especially in the compensation of flow jets near the Hartmann walls when the MHD effect is significant. Consequently, the net thermal energy carried by the fluid will reflect a reduced value when only flow and temperature fields in the core region are considered.

***Figure 2**: Averaged Temperature Difference Between Flow Inlet and Outlet of MaPLE-U First Experiment Data*

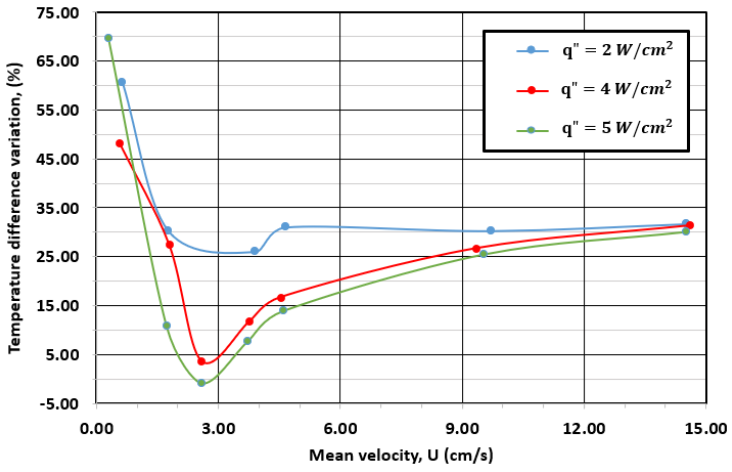

Note. Temperature difference variation under $B_0 = 0.53$ T at different inlet mean velocity and heating flux power.

The phenomenon of flow reversal in mixed-convection MHD flows is of significant interest in both theoretical studies and practical applications, such as in fusion Liquid Metal (LM) blankets. The corresponding heat loss is no longer negligible and necessitates presentation through direct measurement, such as with heat flux sensors, which are planned for installation in the new test article described in the following section.

2.3 New Test Article and Instrumentation

2.3.1 Local Velocity Components Measurement

To comprehend the physics and flow phenomena in MHD flows with mixed-convection effects, it is crucial to have knowledge of local variable fields, including temperature and velocity, within the flowing LM. While measuring temperature fields is relatively straightforward, limited techniques are available for local velocimetry in opaque materials, and even fewer options exist when dealing with temperatures above 450 °C, as is the case in this experiment.

To address this challenge, the LM Electromagnetic Velocimetry Instrument (LEVI) is employed in the new test article to measure the local electric potential and deduce local velocity components via Ohm's law. The concept of this technique is straightforward. As illustrated in Fig. 3 below, a LEVI probe with three electric potential measurement tips is immersed in the fluid flow under a transverse magnetic field. These three tips are positioned on the same plane perpendicular to the applied magnetic field direction.

In this experiment, given that the fluid flow is highly electrically conductive, the static current density from the electric potential gradient in Ohm's law is predominantly balanced by the induced current density from the Lorentz force. As a result, the local velocity components orthogonal to the magnetic field directions can be deduced from the electric potential gradients.

In Fig. 3, where the external magnetic field is applied along the y-axis, the velocity components x and z measured by the LEVI probe are approximated from Eq. 5 as shown below:

$$u_{LEVI} = \frac{1}{2B_0}\left(\frac{\phi_2-\phi_1}{Z_2-Z_1} + \frac{\phi_3-\phi_2}{Z_3-Z_2}\right),\ w_{LEVI} = \frac{1}{2B_0}\left(\frac{\phi_2-\phi_1}{x_2-x_1} + \frac{\phi_2-\phi_3}{x_2-x_3}\right), \quad (5)$$

Figure 3: *LEVI probe illustration.*

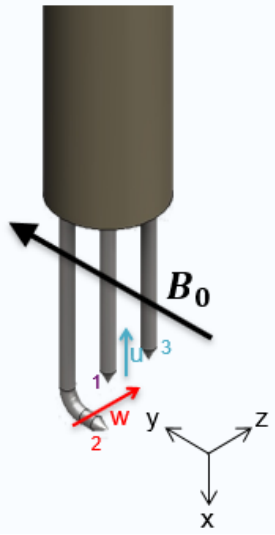

The accuracy of the local velocity calculation approximation is further confirmed through numerical simulations utilizing the fully developed Magnetohydrodynamics (MHD) flow model. The error in deduced velocity from electric potential gradients is found to be less than 8%, lower than the exact axial velocity, particularly in the case with an external magnetic field strength of 1 T (as depicted in Fig. 4).

However, practical implementation of this technique in experiments presents challenges, particularly in measuring voltages of very low amplitude. For instance, at an external magnetic field of 1 T and an inlet velocity of 1 cm/s, the electric potential difference between two neighboring tips with a distance of 2 mm is on the order of microvolts. Hence, dedicated care must be taken to shield the cables, and the thermoelectric effects may need to be considered for such low-amplitude signals. While this technique has been successfully applied in room

temperature LM flows, its performance in high-temperature environments has not yet been demonstrated with sufficient reliability. Challenges include finding suitable coating materials for electrodes and addressing mechanical issues, such as maintaining a sealed condition when employing movable translation probes. In Fig. 4, comparisons are made for the induced voltage between the two sidewalls. A simple estimate based on Ohm's law suggests that without buoyancy effects at the flow velocity of 0.03 m/s and a 0.5 T magnetic field, the induced voltage in the PbLi flow would be tens of millivolts. The computations directly confirm this estimate, with all codes predicting a maximum voltage of about 60 mV.

Figure 4: *Ohm's Law Separated Term Contribution of Fully Developed MHD Flow in Rectangular Duct*

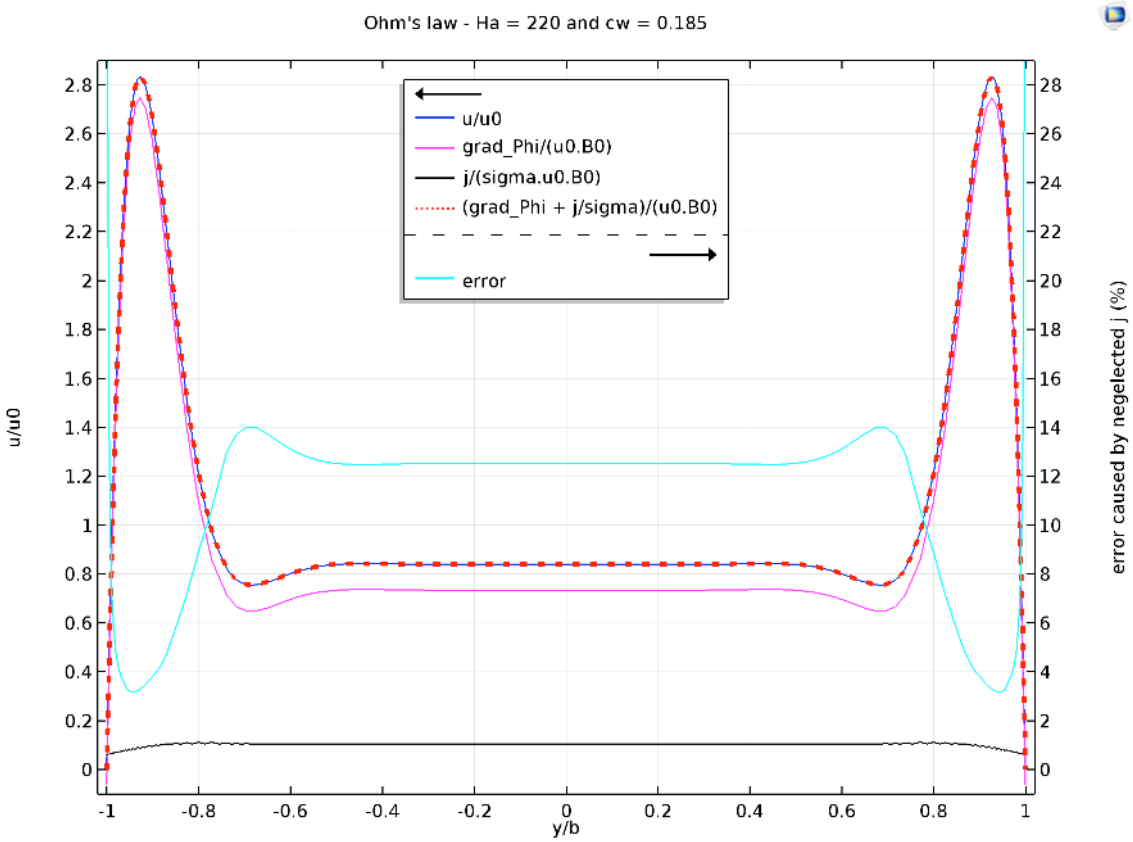

Note. Comparison of magnitude of each term in Ohm's law for estimating the accuracy of LEVI probe for velocity measurement.

2.3.2 Development of LEVI Probe Working in High Temperature Environment

A new movable LEVI probe assembly (depicted in Picture E in Appendix A) has been designed and fabricated for the simultaneous measurement of local temperature and electric potential. The assembly incorporates a probe wire-embedded tube made of alumina to electrically insulate the wire from the surrounding LM fluid. A Grafoil stack is utilized to seal the test section measurement port from the atmosphere during the motion of translation probes. Additional components, including two Teflon O-rings and a compression piston, contribute to reinforcing the sealed condition.

To maintain the melting point temperature of PbLi in the measurement port, a strip heater is wrapped around the top area of the port, monitored by a thermocouple. The rest of the port area is embedded in thermal insulators. The automatic translation of the LEVI probe wire is facilitated by a DC-micromotor with an associated motion controller from the company Micromo®. The translation mechanism, equipped with an automatic programmed actuator (Picture F in Appendix A), and the new sealing scheme were tested by translating the probe-carrying alumina tube in and out a full distance of 50 mm at a speed of 9.75 mm/min into the testing chamber (Picture G in Appendix A). This simulation was performed in static PbLi at temperatures up to 450 ºC, replicating the translation period when the probes measure local flow quantities in the experiment.

The feasibility and reliability of this new assembly were verified by monitoring a steady trend of motor torque (305 mN·m ±15 mN·m) over 100 cycles, with a one-minute pause between changes in translation direction. Unfortunately, in-situ testing of this LEVI instrumentation installed in the new test article under flowing fluid conditions is not available due to the closure of the MaPLE-U facility.

2.3.3 Other Components in New Test Article Design

Six transverse LEVI probe assemblies are scheduled for installation in the new test article, as illustrated in Picture F, to facilitate local flow and temperature quantity measurements. While temperature profiles along the duct perimeter offer valuable insights into identifying flow features, the temporal response of temperature measurements can sometimes be delayed due to the thermal inertia of the system. Electric potential measurements, on the other hand, exhibit a much faster response time, enabling the measurement of rapid flow fluctuations. Consequently, a Dual Temperature-Electric Potential Probe has been designed for installation on all four sides of the test article structure wall, enabling simultaneous measurements of temperature and electric potential.

As depicted in Picture G in Appendix B, 1-mm type-K thermocouples are employed to measure temperature, with their stainless-steel sheath serving as an electrode for electric potential measurement. Each electrode is insulated using fiberglass sleeving. To ensure reliable contact between the thermocouple and the structure wall, the tip of the thermocouple is pressed against the wall using a spring mechanism. Seven sets of Dual Temperature-Electric Potential Probes are installed in the new test article, with a separation distance of 60 cm. To achieve high spatial resolution, 32 probes are utilized at each axial location, with 9 probes on each Hartmann wall (5 mm spacing) and 7 probes on each side wall (6.25 mm spacing on the heater side and 7 mm on the cold side).

Given the significant interest in flow reversal within mixed convection MHD flows, both in theoretical studies exploring instability mechanisms and practical design considerations for fusion LM blankets, the new test article is meticulously designed to capture this flow behavior across a broader parameter range compared to the initial experiment. To induce flow reversal at

higher inlet velocities (for improved velocity measurement accuracy and reduced heat loss) and stronger magnetic field strengths (to enhance the MHD effect and potentially trigger hybrid flow instability mechanisms), the surface heating flux must be elevated. Drawing insights from the first experiment study and the characteristic relationships revealed in numerical simulations (Chapter 3.4), a new heating element (depicted in Picture H) has been designed with higher heating power (17.5 W/cm^2). This element comprises six copper blocks, each 99 mm long, with eight heating cables brazed into machined slots. To prevent fluid flow-induced currents from entering the copper blocks and stainless-steel clamps, a thin mica sheet with a thickness of 0.1 mm is inserted for electrical insulation between the connecting metal materials and the test article channel.

Continuing from the first experiment, two temperature integrators with the same configuration are employed for calorimetry measurements, providing insights into the liquid metal flow regime. Six thermal flux meters, with a sensitivity of 12.66 W/m^2 per mV and 2% accuracy (sourced from International Thermal Instrument Company, Inc.), are strategically installed on the interface of the heaters and thermal insulators to quantify heat loss from the heater to the surroundings. Heat loss on the other sides of the test article walls is anticipated to be negligible.

Ultimately, the new test section will be thermally insulated using custom-shaped calcium silicate blocks (ZIRCAL-18) with a thermal conductivity of 0.08 W/(mK). This insulation ensures an effective thermal barrier for precise control and analysis of the temperature and heat transfer phenomena within the test article.

CHAPTER THREE: VALIDATION AND VERIFICATION OF NUMERICAL TOOL

Understanding the key magnetohydrodynamic (MHD) phenomena in liquid metal (LM) flows within the strong magnetic fields encountered in fusion environments is crucial for designing highly efficient LM blankets. These intense magnetic fields, utilized to confine burning plasma in the fusion reactor core, introduce significant MHD effects on flowing LMs within the surrounding blankets, resulting in notable changes in velocity profiles and associated pressure and temperature distributions. Given the limitations of operating conditions and instrumentation in experimental studies, numerical explorations of MHD flows under harsh fusion environments are preferred for a more comprehensive understanding of flow behaviors and heat/mass transfer phenomena in fusion LM blankets.

A distinctive feature of MHD effects on LM duct flows is the suppression and flattening of the flow velocity in the core region, leading to steep velocity gradients within thin boundary layers. Although this phenomenon has been investigated in numerical, analytical, and asymptotic solutions, these approaches have limited applicability to simple geometries, specific boundary conditions, and no heat transfer coupling. To extend the scope of numerical investigations, numerous MHD computational simulations have been conducted since the 1970s, with limited Hartmann numbers, possibly due to challenges in maintaining local electric current conservation. A widely employed solution to this challenge was introduced through a current density conservative scheme [33], enabling numerical simulations of LM duct flows with high Hartmann numbers ($\sim 10^4 - 10^5$) relevant to fusion LM blanket environments.

Initially, in fusion blankets, it was believed that buoyancy effects in LM flows were mostly suppressed by strong MHD forces, resulting in insignificant impacts on MHD flow profiles from buoyancy forces. Consequently, fluid flow and heat transfer equations were often

solved without reciprocal coupling in many numerical simulations. However, this conclusion was revised following the discovery of the significant influence on MHD flow profiles and behaviors from high temperature gradients [17]. These gradients are expected to be prominent in fusion blanket environments due to strong volumetric and/or surface heating mechanisms. Therefore, computational MHD tools for fusion LM blanket designs must possess the modeling capability to simulate MHD flow and heat transfer equations with instantaneous coupling.

3.1 Introduction of Numerical Explorations on MHD LM flows

Various MHD codes have been developed to address MHD flow problems, either from scratch within laboratory settings, by incorporating built-in MHD packages, or by modifying existing simulation platforms with available non-MHD models. In the realm of lab-made codes, HIMAG and MTC were created using a finite difference approach, while FEMPAR utilized the finite element method. All three codes have undergone validation against analytical solutions and benchmarked experimental and numerical results, specifically for simulating LM MHD flows in rectangular ducts. However, the complete coupling of MHD and heat transfer has only been demonstrated and verified in HIMAG.

Some commercial computational fluid dynamics (CFD) companies have extended their codes, such as Fluent, CFX, and FLUDYN, to incorporate dedicated built-in MHD models with intentional coupling capabilities between the MHD model and other models, such as heat transfer. Other simulation software may not have a built-in MHD model but can be adapted by users for MHD flow simulations. OpenFoam, an example in this category, has been tested and applied for MHD simulations under fusion technology conditions and MHD-heat transfer simulations in laboratory conditions. Another notable candidate in the semi-user-developed code category is COMSOL Multiphysics, serving as a design and analysis tool in fusion cooling applications. The

inherent advantage of the finite element approach, which is the foundation of the solver in COMSOL, makes it suitable for handling complex geometry problems. The flexibility of modifying existing modules in COMSOL, covering various basic physics (e.g., electromagnetism, fluid dynamics, heat transfer), allows users to develop new models with specific requirements and couple different built-in modules for multi-physics simulations. The COMSOL code has gained increasing attention in numerical studies related to fusion LM blankets and has been chosen as the numerical simulation tool in this thesis research.

3.2 Numerical Code Validation and Verification

This section outlines the numerical methodology employed to solve MHD-heat transfer flow problems in COMSOL Multiphysics. The description follows the sequence of setting up governing equations, prescribing boundary conditions, constructing an appropriate mesh, and adjusting simulation solvers. This structure aligns with the modeling tree in the COMSOL Model Builder interface.

3.2.1 Numerical Methodology

MHD flows with heat transfer are defined by three nondimensional parameters: Reynolds number ($Re = \frac{\rho \cdot U \cdot L}{\mu}$), Hartmann number ($Ha = B \cdot L \cdot \sqrt{\frac{\sigma}{\mu}}$), and Grashof number ($Gr = \frac{g \cdot \beta \cdot \Delta T \cdot L^3}{\nu^2}$), where ρ, μ, ν, σ, β are flow parameters of density, dynamic viscosity, kinematic viscosity, electric conductivity, and thermal expansion coefficient respectively; $U, B, L, \Delta T$, are characteristic velocity, magnetic field strength, length, and temperature difference; g is the gravitational constant. These parameters provide a basis for the simulations conducted in this study.

In COMSOL, three built-in physics modules, along with appropriately selected boundary conditions, are employed for the simulations. Additionally, user-defined features are implemented to create a new model specifically designed for fully developed flows. For clarity and consistency with COMSOL formulations, all mathematical equations and expressions presented in the following sections are written in dimensional forms.

3.2.1.1 Governing equations

Liquid metal flows are commonly treated as incompressible, and in many laboratory experiments and fusion reactor blankets, the magnetic Reynolds number ($\mathrm{R_m} = U \cdot L \cdot \mu_0 \cdot \sigma$, where μ_0 is vacuum permeability) is significantly smaller than unity. This implies that the induced magnetic field can be neglected when compared to the applied field. Furthermore, if the applied magnetic field remains constant over time, the electric field is curl-free and equals the negative gradient of the electric potential. When considering non-isothermal liquid metals, the density variations with temperature change are minimal, allowing the use of the Boussinesq approximation. Combining these approximations with the assumption of constant flow properties, the system of equations governing mixed-convection MHD flows is as follows:

$$\nabla \cdot (\mathbf{u}) = 0 \tag{6}$$

$$\rho \frac{\partial \mathbf{u}}{\partial t} + \rho(\mathbf{u} \cdot \nabla)\mathbf{u} = -\nabla p + \mu \nabla^2 \mathbf{u} + \mathbf{J} \times \mathbf{B} + \rho \mathbf{g}(1 - \beta(T - T_o)) \tag{7}$$

$$\nabla \cdot \mathbf{J} = 0 \tag{8}$$

$$\mathbf{J} = \sigma(-\nabla \phi) + \sigma(\mathbf{u} \times \mathbf{B}) \tag{9}$$

$$\rho C_p \frac{\partial T}{\partial t} + \rho C_p (\mathbf{u} \cdot \nabla) T = \kappa \nabla^2 T + q_v \tag{10}$$

where κ is thermal conductivity of the fluid and T_o is a reference temperature. q_v in Eq.10 stands for volumetric heating power that can be explicitly defined by users. Variables $\mathbf{u}, p, \phi, T$

represent velocity field, pressure, electrical potential and temperature that need to be calculated in COMSOL, while **J** is not a computational variable as it will be eliminated with the combination of Eq. 8 and Eq. 9 in calculation.

3.2.1.2 Boundary Conditions

Various problems will involve the application of appropriate boundary conditions, classified as either Dirichlet or Neumann conditions, selected from the options provided in COMSOL. In contrast to the discretized approximation common in finite difference methods for Neumann conditions, variables on these boundaries will be precisely calculated as exact solutions in finite element solvers, given that the flux is formulated in an integral manner. This distinction holds the potential to improve the robustness of schemes and the accuracy of solutions in COMSOL in comparison to finite difference codes.

3.2.1.3 Meshing Strategy

The geometries of all current domains are uncomplicated, typically in the form of ducts or pipes, making structured grids well-suited for implementation. In MHD flows, the boundary layer thickness exhibits an inverse relationship with Ha for Hartmann walls and a square root dependency on Ha for sidewalls. To effectively capture the significant velocity gradients near these boundaries without imposing excessive computational demands on the central bulk region, a hyperbolic function, described in Eq.11, is utilized to stretch the mesh. This is done with the preliminary condition of ensuring a minimum of five elements within all boundary layers.

$$x = 0.5 * (1 + \frac{\tanh(s*(\eta-0.5))}{\tanh(0.5*s)} \quad (11)$$

where s is stretching ratio, η and x are grid point position before and after stretching, both of which are non-dimensional ranging from 0 to 1.

3.2.1.4 Study and Solvers

The equations governing this study are solved in a segregated manner, and the system of discretized equations in each module undergoes linearization using the Newton-Raphson method. Various linear solvers, both in direct and iterative methods, have been examined and ultimately chosen for different problems, considering the accuracy of solutions and computational efficiency.

3.2.2 Code Validation and Verification Activities

MHD flows exhibit extremely thin boundary layers and internal shear layers, at times even thinner than the Kolmogorov length. Additionally, they display a distinctive form of 2D turbulence under a strong magnetic field, wherein fluctuations along the magnetic field direction are significantly suppressed, allowing large flow structures to dominate in the plane perpendicular to the field line. To ensure the appropriate choice of solvers and numerical schemes in COMSOL, it is imperative to address the specific physics of MHD flows and accurately resolve the interesting and crucial flow behaviors. These features in MHD flows necessitate extensive testing against available analytical solutions, two-dimensional, quasi-two-dimensional, three-dimensional numerical data, and experimental studies. Smolentsev et al. [35] proposed an initiative for the verification and validation of MHD codes for fusion applications. This initiative comprises a series of benchmark problems with known results from experimental data or trusted analytical and numerical solutions. Notably, these five problems cover a broad spectrum of MHD flows relevant to fusion applications.

3.2.2.1 Two-Dimensional Fully Developed Laminar Steady MHD Flow

The analysis focuses on the laminar, fully developed, and incompressible flow of a conductive fluid subjected to a pressure gradient within a rectangular duct under the influence of

an imposed transverse magnetic field. Shercliff [36] and Hunt [37] independently addressed this scenario using distinct boundary conditions. In Shercliff's case, all four duct walls are considered non-conductive, while in Hunt's case, the two walls perpendicular to the magnetic field (referred to as Hartmann walls) are conductive, and the walls parallel to the magnetic field vector (denoted as side walls) are electrically insulated. The parameter of interest is the wall conductance ratio is defined as $c_w = \frac{\sigma_w t_w}{\sigma L}$, which indicates the ratio between the electrical conductivity σ_w (S/m) and thickness t_w (m) of the walls and the electrical conductivity of the fluid and the characteristic length of the flow. In Shercliff's case, $c_w = 0$ for all the four walls, whereas in Hunt's case, $c_w = 0$ for the side walls, but non-zero for the Hartmann walls. Following the suggestion of [35], a wall conductance ratio of c_w = 0.01 is considered. Four distinct values of the Hartmann number were chosen: Ha = 500, 5000, 10,000, 15,000.

Figure 5: *Computational Geometry and Mesh of Hunt's Flow*

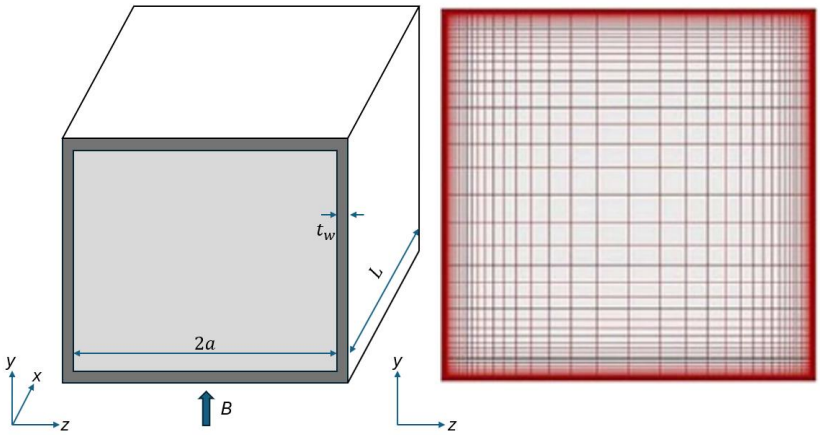

Note. Left figure shows computation geometry in Cartesian coordinate and right figure shows the structured mesh on y-z plane.

The problem was solved in dimensional form in COMSOL, using structured mesh, similar to the one proposed by Yan et al. [38], shown in Fig. 5. Following a grid convergence

analysis, the mesh is composed of 40 elements in the y-direction and 80 in the z-direction for Ha = 500, 60 × 100 for Ha = 5000, and 80 × 120 for Ha = 10,000 and 15,000.

A minimum of five cells is maintained within the Hartmann layers, and seven cells are consistently provided within the side layers. The velocity boundary conditions applied in the study include non-slip conditions at the duct walls and periodic flow conditions at the inlet and outlet of the duct. Electrical boundary conditions involve electrical insulation for the side walls and a thin wall condition represented by $\vec{J} \cdot \hat{n} = c_w \nabla^2 \phi$, with $\hat{n}$ the unit vector perpendicular to the wall, indicating the conservation of electric charge in the wall's plane. The flow solution for a specific case is illustrated in Fig.6 below.

Figure 6: *Velocity Distribution of Hunt's Flow*

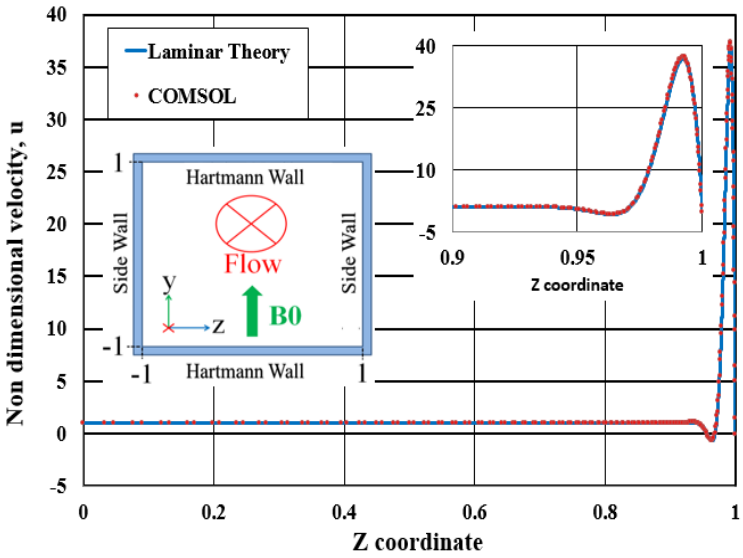

Note. Velocity distribution along z coordinate at center y is simulated at Ha = 15000 with electrical insulating on side wall and $c_w = 0.01$ of conducting ratio on Hartmann wall. The small, embedded figure on the right top corner shows the zoom-in results near one side wall (z = 1)

To facilitate a comparison with the findings presented in Smolentsev [35], the dimensionless flow rate $\tilde{Q}$ as the parameter is depicted, which is defined as

$$\tilde{Q} = \frac{4}{b^2} * \frac{\mu u}{(-\partial \mathrm{p}/\partial \mathrm{x})} \tag{12}$$

Here u (m/s) represents the x-component of the velocity vector, b (m) is half the Hartmann wall length and $\partial p/\partial x$ (Pa/m) denotes the imposed pressure gradient in the direction of the flow. The relative error between COMSOL results and the analytical solutions by Shercliff and Hunt is evaluated as:

$$\epsilon_{rel} = \left|1 - \frac{\tilde{Q}}{\tilde{Q}_{ana}}\right| \tag{13}$$

where $\tilde{Q}$ is the COMSOL solution and $\tilde{Q}_{ana}$ is the analytical solution. The calculations are reported in Table 2. The table presented illustrates a notable agreement between the analytical and numerical results.

Table 2: *Comparison of Dimensionless Flow Rate Between Analytical and COMSOL Results*

		Dimensionless Flow Rate $\tilde{Q}$		Relative Error, ϵ_{rel}
Ha	Flow type	Analytical	COMSOL	
500	Shercliff	7.679e-3	7.666e-3	0.176%
5000		7.902e-3	7.812e-3	0.384%
10000		3.965e-3	3.952e-3	0.337%
15000		2.648e-3	2.638e-3	0.359%
500	Hunt	1.405e-3	1.406e-3	0.050%
1000		1.907e-3	1.901e-3	0.295%
10000		5.169e-3	2.145e-3	0.468%
15000		2.425e-3	2.413e-3	0.486%

3.2.2.2 Three-dimensional Laminar, Steady Development MHD Flow in a Non-uniform Magnetic Field

In the second benchmark scenario, a conductive fluid traverses through two distinct ducts—one with a rectangular cross-section and the other with a circular cross-section—under

the influence of a nonuniform magnetic field emanating from a magnet exit. This case underwent experimental scrutiny at the Argonne National Laboratory within the ALEX (Argonne's Liquid metal EXperiment) facility [39, 40]. Eutectic NaK served as the working fluid within a closed-loop system at room temperature. In this scenario, the changing magnetic field, $\vec{B} = B(x) \cdot \hat{y}$ with $\hat{y}$ unit vector in the y-direction as shown in Fig. 7, necessitates additional domain discretization in the x-direction, building upon the previously analyzed 2D case. The velocity boundary conditions adopted in the study include non-slip conditions at the duct walls and an imposed average velocity at the inlet. The electrical boundary condition is a thin wall condition applied to the walls.

Figure 7: *Transverse Applied Magnetic Field Distribution*

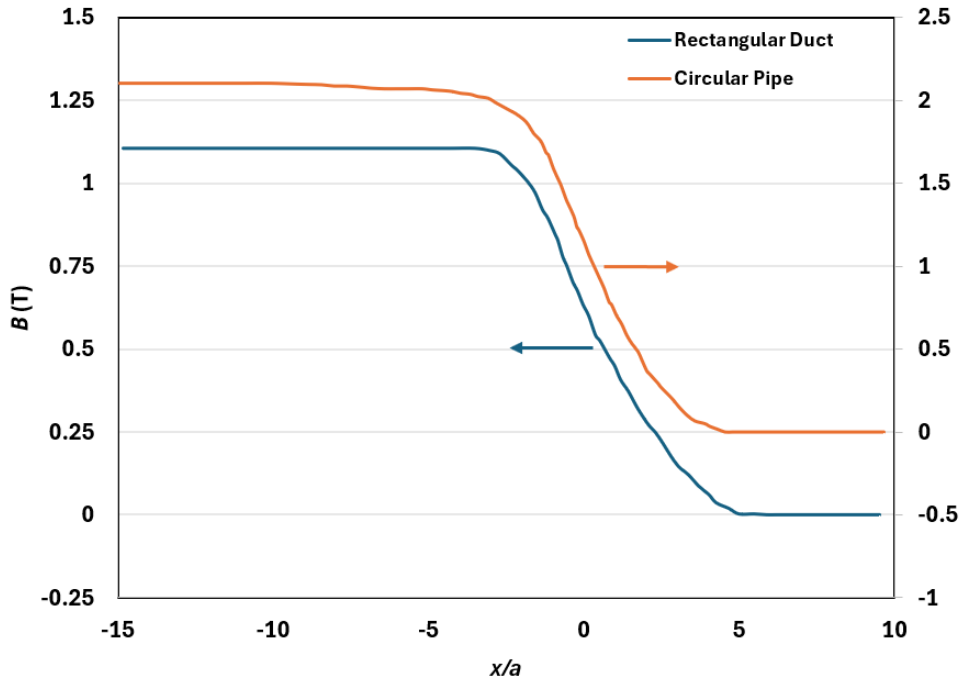

Note. This figure displays the transverse applied magnetic field distribution along the flow direction in ALEX experiment with MHD flow in rectangular duct and circle pipe.

3.2.2.2.1 Rectangular Duct

The symmetry of the problem is leveraged, considering only half of the duct cross-section similar to the study of Shercliff and Hunt flows in the previous section. The mesh is structured with a symmetric distribution of elements in the flow direction, maximizing cell density in the central region where the magnetic field undergoes the most change. In the y and z directions, the mesh follows a similar pattern as proposed in the previous section (3.2.2.1). The total number of elements is 3.4×10^5, and the equations are solved in dimensionless form.

For the study, the selected parameters are Ha = 2900, N = 540 and c_w = 0.07. The comparison metric with the experimental results is the dimensionless axial pressure gradient, i.e., the pressure gradient developed along the duct axis, scaled by $\sigma U B_0^2$. The results are presented in Fig. 8, displaying the axial pressure difference obtained by Picologlou et al. [39] in comparison with the present work. The curves exhibit good agreement, with the main deviation occurring in the region $-5 < x/L < 0$, where COMSOL tends to slightly overestimate the pressure difference probably due to the 3D local effect which breaks the assumption of flow symmetry on the plane at z = 0. This behavior is also found in work by Sahu [41] and Alberghi, et al. [42], and from the HIMAG Code calculations [43]. The difference between the two solutions is calculated using the integral of the curves with the following relation, called integral error index:

$$\epsilon_{int} = \left| 1 - \frac{\int_{x_{min}}^{x_{max}} \Delta p(x) dx}{\int_{x_{min}}^{x_{max}} \Delta p_A(x) dx} \right| \tag{14}$$

where $\Delta p_A \; and \; \Delta p$ are respectively, the ALEX experiment and the COMSOL nondimensional axial pressure difference. The integrals are computed numerically, using the trapezoidal rule, and the resulting error is 1.52 %.

Figure 8: *Axial Pressure Gradient for MHD Flows in a Rectangular Duc under Fringing Transverse Magnetic Field*

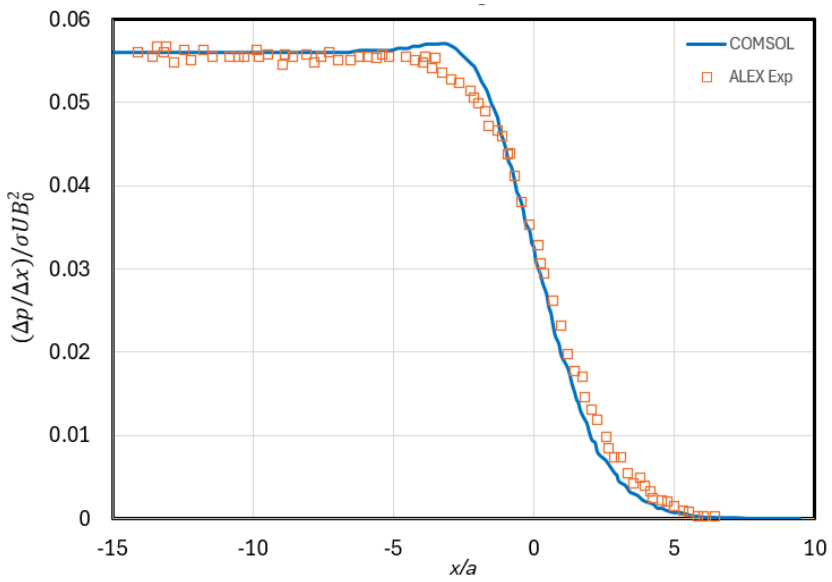

Note. Comparison of axial pressure gradient between COMSOL simulation and ALEX experiment data for rectangular duct at Ha = 2900, N = 540 and c_w = 0.07.

3.2.2.2.2 Circular Duct

In the x-direction, the mesh used is equivalent to the previous case. However, in the y and z planes, 25 boundary layers are considered, generated from the first layer with a thickness of 10^{-6} m and a growth rate of 1.3. The total number of elements is 3.5×10^5. The parameters adopted for the study are Ha = 6600, N = 10,700 c_w = 0.027, and Ha = 6600. In figure 9, the results are presented, showing excellent agreement between the curves, with an integral error index of 1.07 %.

Figure 9: *Axial Pressure Gradient for MHD Flows in a Circular Pipe under Fringing Transverse Magnetic Field*

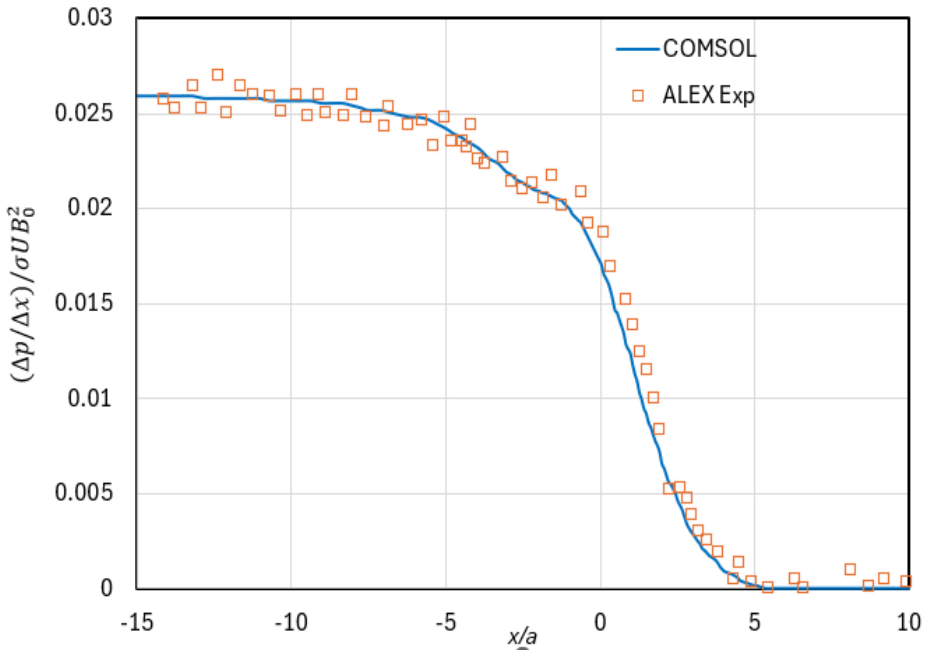

Note. Comparison of axial pressure gradient between COMSOL simulation and ALEX experiment data for rectangular duct at Ha = 6600, N = 10,700 and c_w = 0.027.

3.2.2.3 Magneto-Convection Flow

The subsequent benchmark cases were formulated with the intention of encompassing representative scenarios for liquid metal breeding blankets characterized by non-isothermal conditions and internal volumetric heating. The study addresses the flow of an electrically conducting fluid within a long horizontal channel of rectangular cross-section [44]. Flow is induced by buoyancy forces resulting from non-isothermal conditions, a phenomenon known as the mixed-convection effect. As illustrated in Fig.10, the imposed magnetic field is $\vec{B} = B_0 \cdot \hat{z}$ and the gravitational acceleration $\vec{g} = -g \cdot \hat{y}$, is aligned with the channel axis. In this context, two cases are examined: steady state case with $Ra = 10^4$, and unsteady state case with $Ra = 3 \times 10^5$. In both cases, the Ha = 200.

Figure 10: *Axial Average Temperature Distribution Along Vertical Axis of Steady MHD Flows in a Cavity with Uniform Heating from Bottom.*

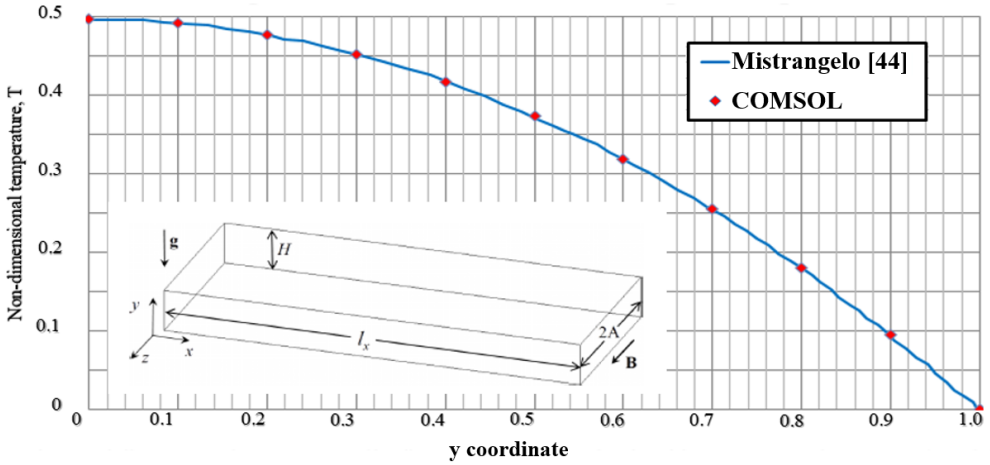

Note. This figure displays the computation geometry and the temperature distribution averaged in x and z along the y direction with Ha = 200, and Ra = 10^4. The flow under such parameters is in a steady state condition. The result from COMSOL overlaps exactly with the results from Mistrangelo simulations [44].

3.2.2.4 Quasi-Two-Dimensional MHD Turbulent Flow

This case regards a quasi-two-dimensional MHD turbulent flow as proposed in [35]. Burr et al. [45] developed an experimental setup consisting of a rectangular stainless-steel channel of side length 0.04 m and wall thickness 6 mm where the eutectic sodium–potassium alloy is circulated under the presence of a magnetic field. NaK, with density $865\ \mathrm{kg/m^3}$ and kinetic viscosity $9.5 \times 10^{-7}\mathrm{m^2/s}$, flows in the x-direction, and $\vec{B}$ is oriented in z and can be varied from 0.25 T to 2.5 T. The electric conductivity of the wall is $1.39 \times 10^6\ \mathrm{S/m}$, whereas the one of the NaK is $2.8 \times 10^6\ \mathrm{S/m}$, from which it results in wall conductance ratios of $c_w = 0.05$. The Hartmann number investigated is 200 and Reynolds numbers are 3000 and 8000.

Figure 11: *Vertical Velocity Plot at y-z Plane of Unsteady MHD Flows in a Cavity with Uniform Heating from Bottom.*

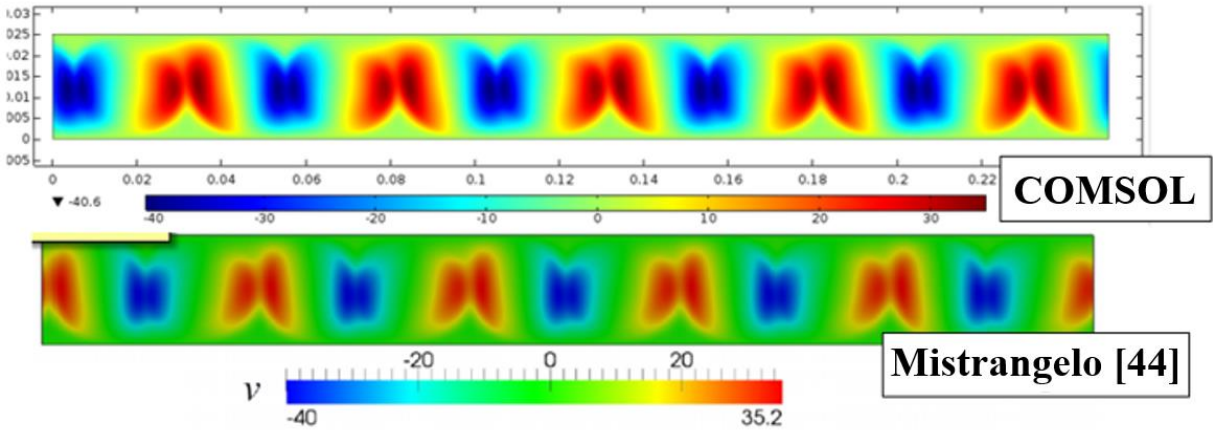

Note. This figure displays the instantaneous contours of vertical velocity v at y-z plane with Ha = 200, and Ra = $3X10^5$. The flow turns unsteady and there is a good quantitative and qualitative agreement between COMSOL and Mistrangelo simulations [44].

The main characteristics of the flow are well expressed, and the influence of the Reynolds number on the flow is evident. This is a characteristic of turbulent MHD flows, while the velocity distribution of laminar MHD flows is governed only by Hartmann number. Turbulence smooths out velocity peaks in the side walls that are reduced for increasing Reynolds numbers, and the width of the side layer increases with Reynolds number due to turbulent transfer of momentum.

As shown by the results in Fig. 12 and Fig. 13, the code can tackle quasi-two-dimensional MHD flow problems, giving reliable results, particularly in the side layer region. Further improvements are needed to better compute the bulk turbulence that is underestimated by the code.

Figure 12: *Base Velocity Distribution at y-z Plane and Mean Velocity Distribution Along z Axis of MHD Flows in a Squared Duct with the Finite Wall Electric Conductivity*

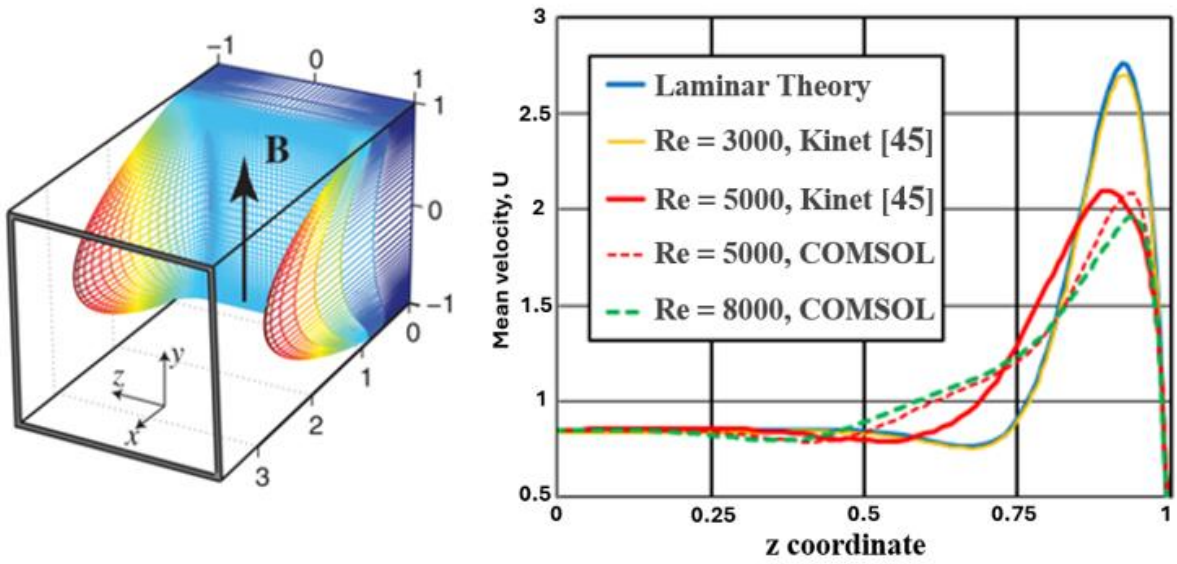

Note. The picture on the left shows the base flow distribution from laminar flow theory. The right figure shows the results comparison between COMSOL and Kinet [45] in which COMSOL predicts similar flow jet features, but over-estimates the mean flow near the flow jet leg region (z is from 0.6 to 0.75) indicating the underestimate of flow turbulence in that region probably due to insufficient mesh resolution in COMSOL.

Figure 13: *Instantaneous Contours of Axial Velocity* $\boldsymbol{u}$ *and Transverse Velocity Disturbance w' of Unsteady MHD Flows in a Squared Duct with the Finite Wall Electric Conductivity*

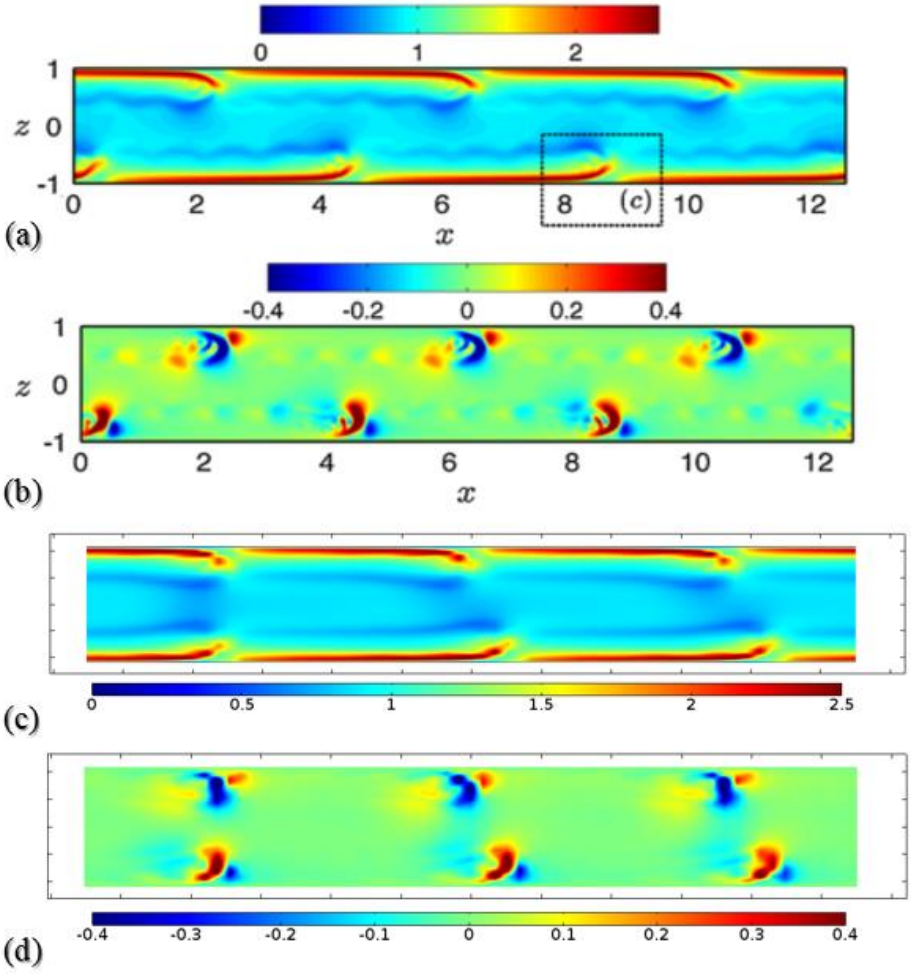

Note. These four pictures show instantaneous contours of axial component of (a), (c) the total axial velocity u and (b), (d) the transverse disturbance velocity w' for Re = 5000 from Kinet [45] and COMSOL respectively. Again, the computational results from COMSOL demonstrate good qualitative and quantitative agreement with the simulations by Kinet [45], while less flow turbulence features are captured in COMSOL near the flow jet leg region probably due to insufficient mesh resolution and additional artificial viscosity in COMSOL solver.

3.3 Development and Application of Fully Developed MHD/heat transfer Flow Model

In the evaluation of different LM blanket designs, the results from fully developed flows are often applied for estimation of important flow behaviors such as pressure drop, flow reversal, and for demonstration of velocity and temperature distribution when 3D simulation results are not available. However, previous estimations have either been calculated without heat transfer effects [46] or without simultaneous coupling between MHD and heat transfer equations [47,48]. In this study, a new model is established to complete, for the first time, the simultaneous coupling of MHD buoyant interaction of fully developed flows. Buoyancy effect on pressure drop estimation and prediction of flow reversal in fusion LM blankets are characterized using this model. These results can also work as reference data for code development. Moreover, part of the mesh sensitivity studies in next section will also rely on results from this model.

3.3.1 Modification of mathematical model

As the computational variable in the heat transfer equation in COMSOL, the absolute temperature T in fully developed flows will increase linearly along the axial direction if there is a positive net energy gain from applied heating. In order to obtain results independent of flow direction, the absolute temperature needs to be decomposed into mean temperature $\bar{T}$ and a fluctuation component θ as shown in Eq. 15 such that the net energy gain is taken over by $\bar{T}$, while the integral of θ remains unchanged along flow direction.

$$T(x,y,z) = \bar{T}(x) + \theta(y,z) \tag{15}$$

where $\bar{T}(x) = T_0 + \frac{Q(x)}{\dot{m}C_p}$, ($x$ is the flow direction)

Therefore, buoyancy force in Navier-Stoke equations can be rewritten as $\rho\mathbf{g}(1-\beta\theta)$, and the heat transfer equation will be reformulated in terms of θ with the derivation from Eq. 16 to Eq. 18.

$$\rho c_p u\left(\frac{1}{\dot{m}c_p}\frac{dQ(x)}{dx}\right) = \kappa\left(\frac{\partial^2\theta}{\partial y^2}+\frac{\partial^2\theta}{\partial z^2}\right)+q_v \tag{16}$$

$$\dot{m} = \rho\iint u dA = \rho U_m A,\ \ Q(x) = \left(\iint q_v dA + \int q_s dL\right)x \tag{17}$$

$$\kappa\left(\frac{\partial^2\theta}{\partial y^2}+\frac{\partial^2\theta}{\partial z^2}\right) = q_v\ -\frac{u}{U_m A}\left(\iint q_v dA + \int q_s dL\right) \tag{18}$$

Periodic boundary conditions for momentum and energy equations are applied on inlet and outlet boundaries for variable u, ϕ and θ. As periodic flows are strictly pressure driven in COMSOL, an additional user-defined equation will be used to prescribe flow rate instead of pressure drop.

3.3.2 Model validation

Neither analytical solution, nor numerical data of mixed-convection MHD flows with electrically conducting walls is available for comparison with the present model. Asymptotic solutions, derived by L. Bühler [46] of MHD flows driven purely by differential temperature (constant temperature difference between two opposite walls) will then be considered as reference data. Specifically, fully developed, laminar, MHD flows in a vertical, square, perfectly electrically conducting duct in the presence of a strong transverse magnetic field and a constant wall temperature difference, are simulated using this model. Non-dimensionalized results of velocity distributions are compared with asymptotic solutions at four different Hartmann numbers. As shown in Fig. 14, great match-up is performed for Ha>100 while a slightly lower velocity jet is predicted by COMSOL at Ha=25. This discrepancy may be due to the asymptotic solution becoming invalid at lower Ha which was mentioned by the author already [46].

Figure 14: *Axial Velocity Distribution of MHD Flows in a Square Duct under Buoyancy Effect due to a Constant Temperature Difference Two Side Walls*

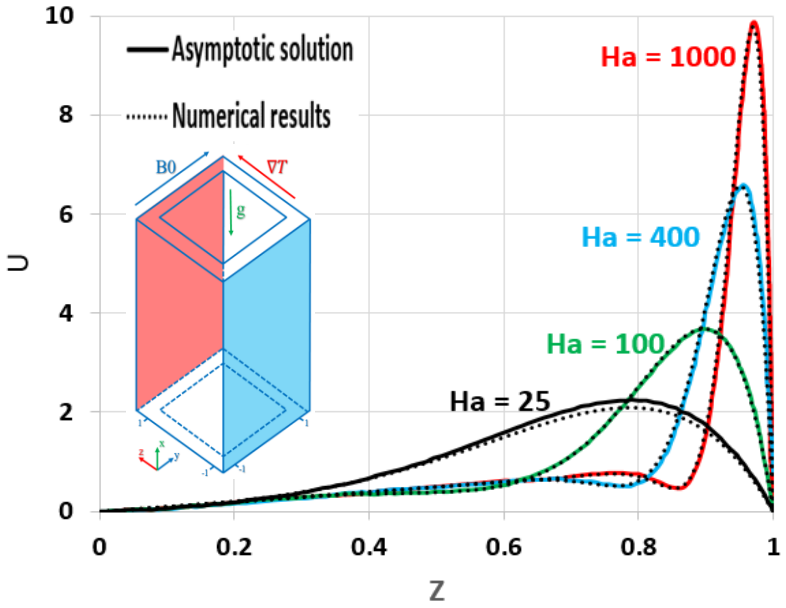

Note. Axial velocity u distribution along the z coordinate is compared between COMSOL simulations and asymptotic solutions at different Hartmann number from 25 to 1000.

3.3.3 Application of fully developed MHD/heat transfer flow model

In this section, the fully developed flow model will be used to 1) characterize the flow reversal and 2) improve the estimation of pressure drops in mixed-convection MHD flows with opposed buoyancy force. This model is also applied for mesh sensitivity studies.

3.3.3.1 Characterization of flow reversal

In LM blanket designs, locally high temperature (also called hot spots) and flow instability, as two critical issues, are highly affected by the flow reversal when the opposing buoyancy effect is strong enough. In this section, the first occurrence of flow reversal, determined by zero friction coefficient averaged on hot wall, is characterized as a critical value with respect to Gr, Re and Ha such that $\frac{Gr}{ReHa^n}\Big|_{critical} = F(c_w)$, where F is a function of wall

electrical conductivity ratio c_w, and $n = 1$ or 2 corresponds to electrically insulating ducts or conducting ducts respectively. The results are shown in Fig. 15, in which, two different values of wall electrical conductivity ratio ($c_w = 0.12, 0.012$) are considered in addition to the case of insulating ducts ($c_w = 0$) where the analytical solution is available for comparison. The flow parameters range from experimental environment to fusion blanket relevant conditions.

3.3.3.2 Evaluation of buoyancy effects on pressure drops

In the development of fusion LM blanket designs, an analytical solution of pressure drop in MHD duct flows is often applied as shown in Eq. 19

$$\frac{\Delta p}{\frac{1}{2}\rho U^2} = \lambda \cdot \frac{L_p}{2L}, \lambda = \frac{8}{Re}\frac{Ha^2}{C_w+1}\frac{C_w \cdot Ha + \tanh(Ha)}{Ha - \tanh(Ha)} \quad (19)$$

where λ is called the pressure drop coefficient and L_p is the duct length.

From this equation, the MHD pressure drop is assumed with no effect from buoyancy forces because it will strongly depend on Lorentz force which would be slightly altered by buoyancy effect. However, no quantitative comparison is available so far for pressure drops between mixed-convection MHD flows (dp_{MC}) and purely MHD flows (dp_{MHD}). Therefore, in this section, such a comparison will be given in order to evaluate buoyancy effects on MHD pressure drops.

As an example, for this evaluation, fully developed mixed-convection MHD vertical downward flows in electrically conducting square duct are studied (geometry of flow and coordinate system is shown in figure (7) in Appendix B) with the change of Gr/Re at different Ha in the range from laboratory to LM blankets conditions. As can be seen in figure (8)-(9) in Appendix B, buoyancy forces would strongly alter the velocity profiles but slightly affect the

pressure drops even if flows start to be reversed near hot walls. If Gr/Re keeps increasing and exceeds a certain value, a steep rise of pressures drops is observed where dp_{MC} is several times

Figure 15: *Prediction of Flow Reversal in Terms of Gr/Re and* $\boldsymbol{Ha^2}$ *Using a Novel MHD/Heat Transfer Flow Model*

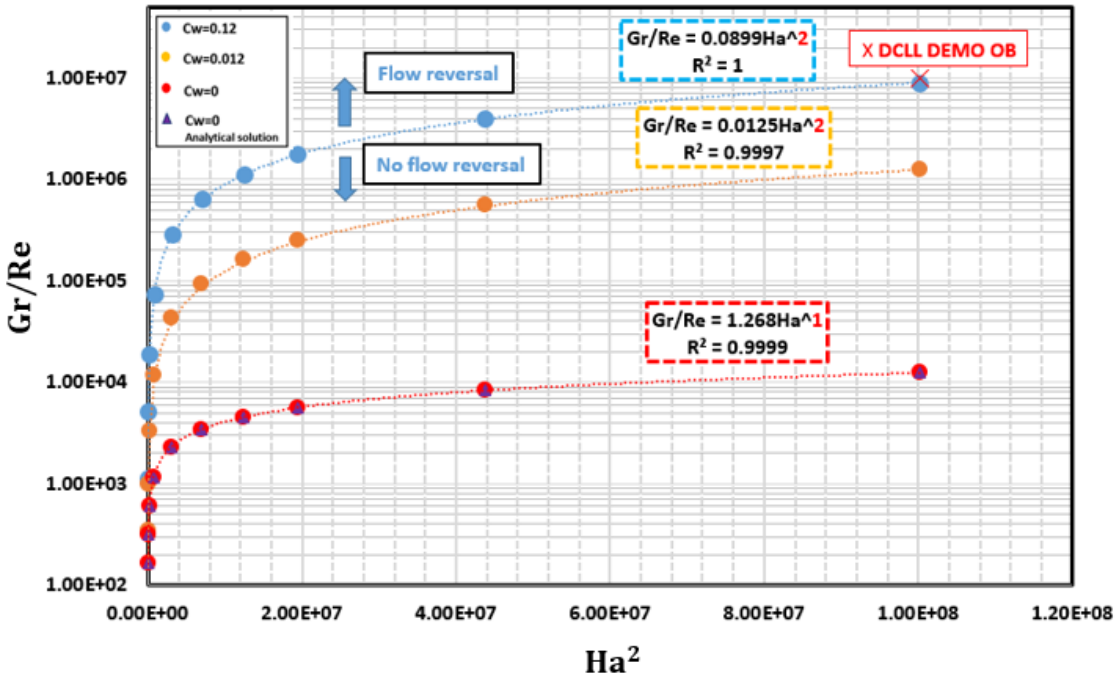

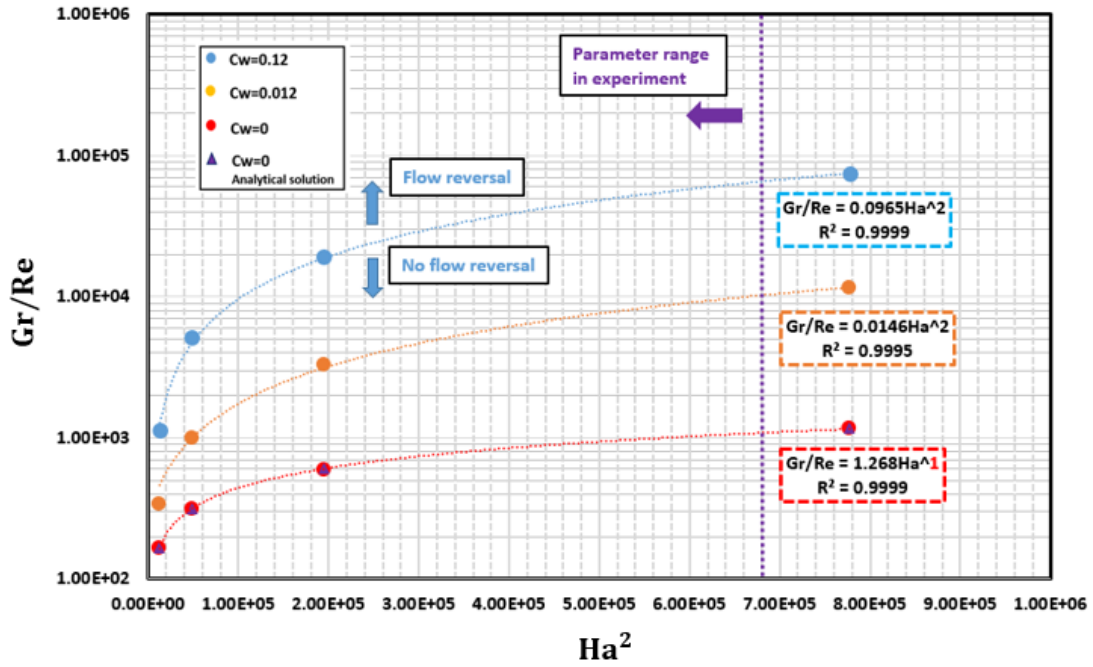

Note. Flow reversal critical value is characterized by the combination of Gr, Re and Ha with the parameter range covering both fusion reactor conditions (top) and laboratory environment (bottom).

larger than dp_{MHD}. At the same time, a pair of almost symmetric high flow jets is created on hot and cold walls. However, such an observation may not be seen in reality as the formation of the asymmetric flow jets is a paradox called "elevator mode" by Liu and Zikanov [49].

As an example, for this evaluation, fully developed mixed-convection MHD vertical downward flows in electrically conducting square duct are studied (geometry of flow and coordinate system is shown in Fig. 16) with the change of Gr/Re at different Ha in the range from laboratory to LM blankets conditions.

Figure 16: *Flow Geometry and Coordinate of a Selected Mixed-Convection MHD Flow Study*

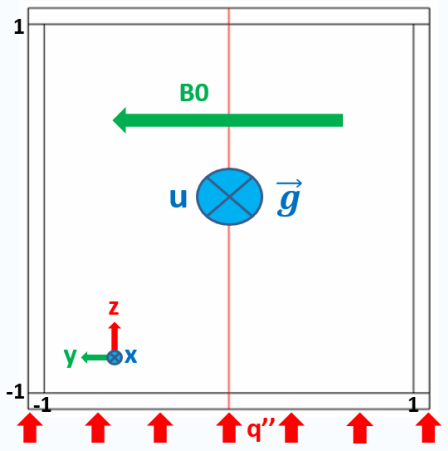

As can be seen in Fig. 17 and Fig. 18, buoyancy forces would strongly alter the velocity profiles but slightly affect the pressure drops even if flows start to be reversed near hot walls. If Gr/Re keeps increasing and exceeds a certain value, a steep rise of pressures drops is observed where dp_{MC} is several times larger than dp_{MHD}. At the same time, a pair of almost symmetric high flow jets is created on hot and cold walls. However, such an observation may not be seen in

reality as the formation of the asymmetric flow jets is a paradox called “elevator mode” by Liu and Zikanov [49].

Figure 17: *Pressure Drop Ratios Between Mixed-convection MHD Flows and Purely MHD Flows*

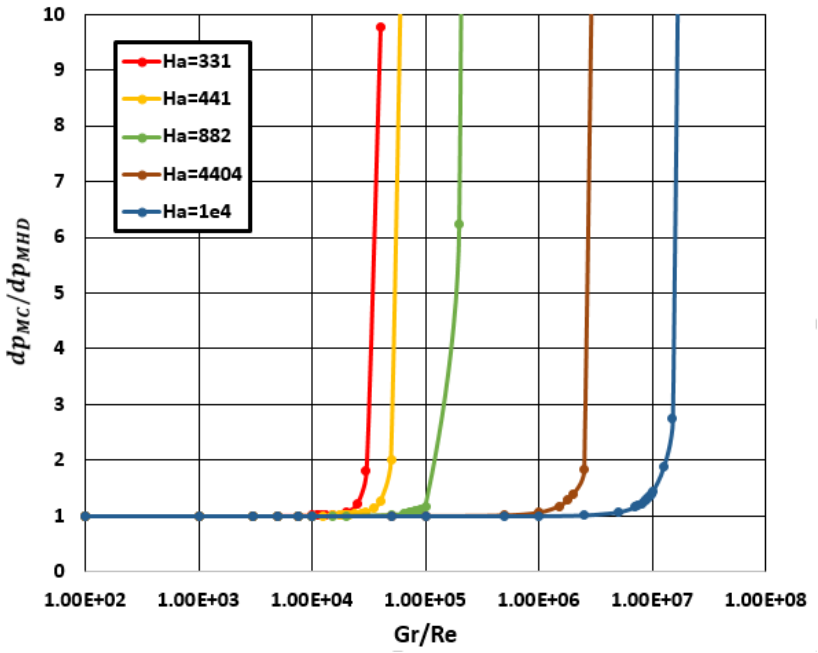

Note. Pressure drop ratios of MHD flows with and without buoyancy driving flow effect are compared in this figure for different Hartmann numbers. Clearly, the pressure drops in mixed-convection MHD flows would greatly overcome the ones in purely MHD flows at high Gr/Re to reach eventually the paradox of elevator mode of flows that would not physically exist.

3.4 Numerical Simulations for Mixed Convection MHD Flow in MaPLE-U Loop

3.4.1 Properties and Phenomena of Mixed-convection MHD Flow in Fusion Blanket

As an expanded benchmarking case to the database of validation and verification of MHD simulation tools [35], the buoyancy-driven MHD flows are targeted where buoyancy forces collaborate with forced flow, resulting in a mixed-convection flow pattern. These buoyancy-induced flows, with velocities typically ranging between 10 to 20 cm/s (depending on

specific blanket configurations and gravitational orientations), hold significance for various liquid metal (LM) blanket designs currently under exploration. For instance, in dual-coolant lead-lithium (DCLL) blankets, the eutectic PbLi alloy circulates at approximately 10 cm/s in lengthy poloidal ducts for tritium breeding and cooling, where the flow velocity due to pressure-driven circulation is comparable to the buoyancy-induced velocity [50]. Buoyancy effects also play a vital role in helium-cooled PbLi and water-cooled PbLi blankets, where PbLi circulates at extremely low velocities in the order of millimeters per second for tritium breeding, while helium gas or water functions as the coolant. Even in self-cooled PbLi blankets, where PbLi velocity is considerably higher (around 0.5 to 1 m/s) compared to other PbLi blankets, buoyancy effects remain significant.

Figure 18: *Velocity Distribution Along Heating Direction of a Fully Developed MHD/Heat Transfer Flows in a Vertical Square Duct*

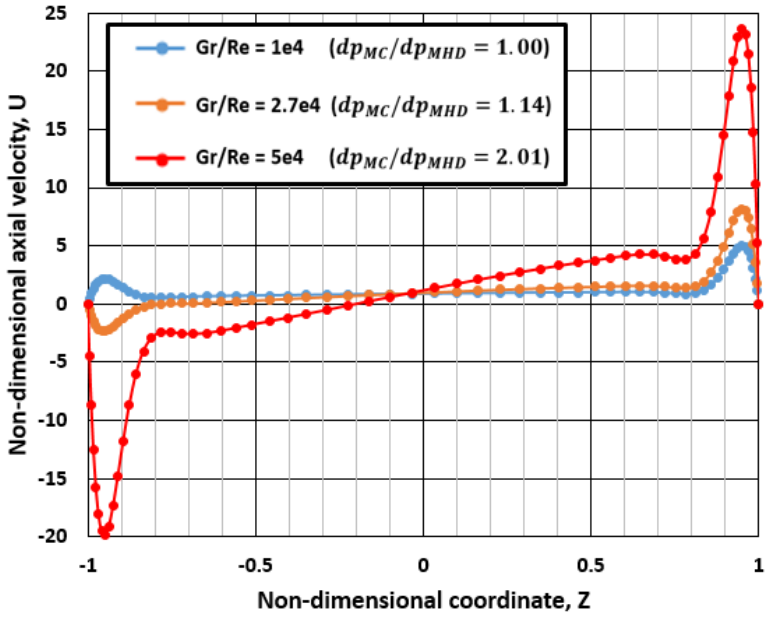

Note. The elevator mode can be much easier to identify in the figure of plotting the axial velocity along the heating direction z, as the flow jets near the walls would keep increasing in opposite directions without being bounded.

Research on mixed-convection MHD flows in both horizontal and vertical ducts have garnered considerable attention in recent literature among computational modelers and experimentalists, although studies focusing on vertical flows are relatively scarce. The behavior of flow in a vertical duct varies significantly depending on the flow direction relative to the gravitational vector (upward/buoyancy-assisted or downward/buoyancy-opposed), heating scheme (surface or volumetric), and wall electrical conductivity. These variations influence factors such as instabilities, the transition to turbulence, the prevalence of two-dimensional or three-dimensional (3-D) characteristics, and the formation of distinct flow patterns. Known instabilities, often attributed to Kelvin-Helmholtz type phenomena, are typically associated with inflection points in the velocity profile. Recent experiments on mixed-convection vertical flows in the presence of a transverse magnetic field have revealed significant low-frequency, high-magnitude temperature fluctuations in both circular pipe and rectangular duct flows heated from the wall. Analytical solutions derived for fully developed mixed-convection flows in nonconducting ducts with nonuniform, exponential volumetric heating suggest that locally reversed flows near the hot wall can occur if the main flow is downward and the Grashof number is sufficiently high. Numerical simulations based on both full 3-D flow models and quasi-two-dimensional (Q2D) flow models also predict instabilities and flow reversals under the influence of a strong magnetic field. It is noteworthy that nearly all 3-D studies of mixed-convection MHD flows demonstrate the dominance of Q2D flow dynamics.

3.4.2 Reference Case of Benchmark Mixed Convection MHD Flow

The selected benchmark scenario involves a vertical downward flow within a square duct, replicating the geometry of a Dual-Coolant Lead-Lithium (DCLL) blanket. The elongated flow path in this reference case permits a potentially fully developed flow regime, mirroring

conditions expected in a real blanket. In practical blanket designs, the poloidal flow length ranges from approximately 2 m (for modular blankets) to a complete "banana" segment of about 10 m [50]. In this reference case, the vertical length is set at 2 m. The cross-sectional dimensions in this reference scenario are about four times smaller than those in a typical blanket, measuring 5 × 5 cm, which includes a thin steel wall ($t_w = 2$ mm). These dimensions were carefully selected to accommodate the workspace of the electromagnet in the MaPLE-U facility [31]. It's noteworthy that all dimensions and parameters in the reference case adhere to the specifications of the experimental MaPLE-U facility, facilitating potential benchmarking experiments on mixed-convection flows in the future. However, as of the writing of this thesis, experimental data for this reference case is not yet fully available.

In the reference scenario, a flow of PbLi enters a vertical square duct from the top and proceeds downward. One of the duct walls is uniformly heated over a length of 0.6 m, as depicted in Fig. 19 (a). All other walls are thermally insulated. The flow experiences a transverse magnetic field, with its distribution along the axial coordinate shown in Fig. 19 (b). The magnetic field distribution includes two fringing zones at the entry and exit from the magnet, where the magnetic field transitions from zero to a constant value. The length of the uniform magnetic field is approximately 0.8 m, and its magnitude is denoted as B_0 = 0.5 T. In computations, the magnetic field was approximated using a formula that incorporated a $tanh$ function to accurately represent both the uniform and fringing field regions. It's worth mentioning that the heated section is 20 cm shorter than the uniform magnetic field length, and the entire duct is longer than the magnet, ensuring that the flow at the entry and exit from the duct remains purely hydrodynamic without magnetic field influence.

Table 3 presents the thermophysical properties of PbLi and stainless steel (SS-394) at an inlet temperature of 300°C. The computational parameters include a flow velocity U_0 of 0.03 m/s and an applied surface heat flux q'' of 0.04 $\mathrm{MW/m^2}$. Utilizing the dimensional data, key dimensionless parameters are computed: Hartmann number of 220, Reynolds number of 3040, and Grashof number of $2.88\ X\ 10^7$. These dimensionless parameters are constructed using the duct halfwidth (b = 0.023 m) as a length scale. Another noteworthy dimensionless parameter, not directly employed in the computations, is the wall conductance ratio $c = \frac{t_w \sigma_w}{b \sigma_{PbLi}} = 0.12$, where it is noteworthy that $c \gg 1/Ha$. This observation suggests that a significant portion of the electric current generated in the bulk flow completes its circuit through the electrically conductive wall.

Figure 19: *Geometry and Operation Conditions of a Reference Study Case for Code-to-Code Comparison*

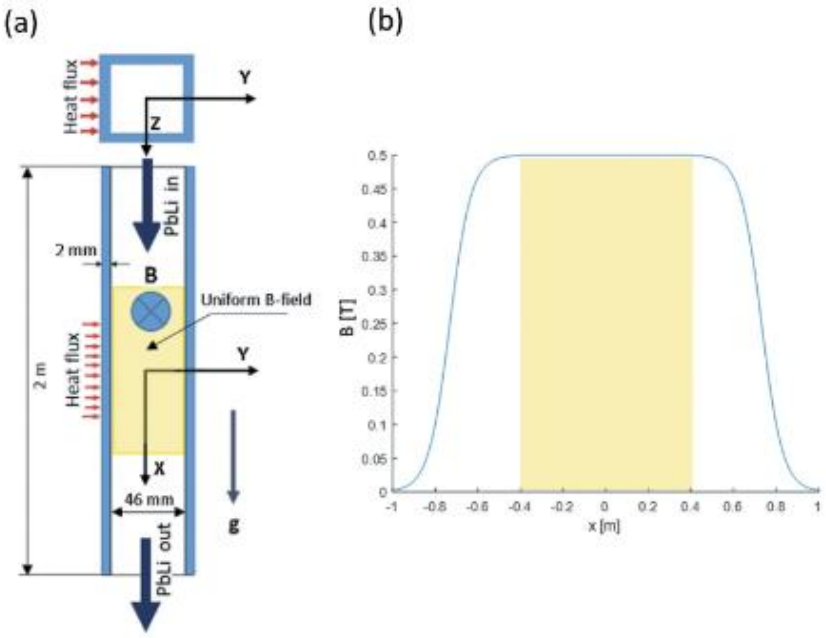

Note. Reference Case of a downward mixed-convection MHD flow includes (a) schematic diagram for the flow geometry and conditions. (b) Space variant applied magnetic field distribution [51].

Table 3: *Physical Properties of PbLi and SS-394 at 300°C*

Physical Property	PbLi	Stainless steel 394
Density, ρ (kg/m^3)	9486	7800
Kinematic viscosity, ν (m^2/s)	2.27e-7	NA
Electrical conductivity, σ (S/m)	7.89e5	1.09e6
Specific heat capacity, C_p (J/kgK)	200.2	500.0
Thermal conductivity, k (W/mK)	13.1	19.0
Volumetric expansion coefficient, β $(1/K)$	1.774e-4	NA

3.4.3 Characterization of Mixed-convection MHD Flows in COMSOL

This section presents a detailed depiction of the flow and temperature fields based on recent investigations of mixed convection flows employing both the COMSOL and HIMAG codes. In Fig. 20, downstream variations of velocity and temperature, including instantaneous and time-averaged fields, are illustrated. The uniform, isothermal flow of PbLi enters from the top (Fig. 20, x = −1 m) and undergoes hydrodynamic development as it progresses downstream. Upon entering the magnetic field zone, MHD effects begin to influence the flow. The transversely applied magnetic field (B_0) interacts with the LM flow, generating circulations of electric current (j) and associated electromagnetic Lorentz forces ($= j \times B_0$) significantly impacting the fluid's motion. As the flow enters the uniform magnetic field region, the initial isothermal flow exhibits an M-shaped velocity profile (Fig. 20, x = −0.25 m). This profile is characterized by a uniform velocity within a central core or bulk region, very thin Hartmann boundary layers attached to walls perpendicular to the magnetic field, and thin jets attached to sidewalls running parallel to the magnetic field. The formation of sidewall jets is a consequence of rotational electric currents (curl(j) ≠ 0) closing through the electrically conducting walls.

Figure 20: *Time Averaged Velocity and Temperature Distribution Along z Coordinate at y = 0*

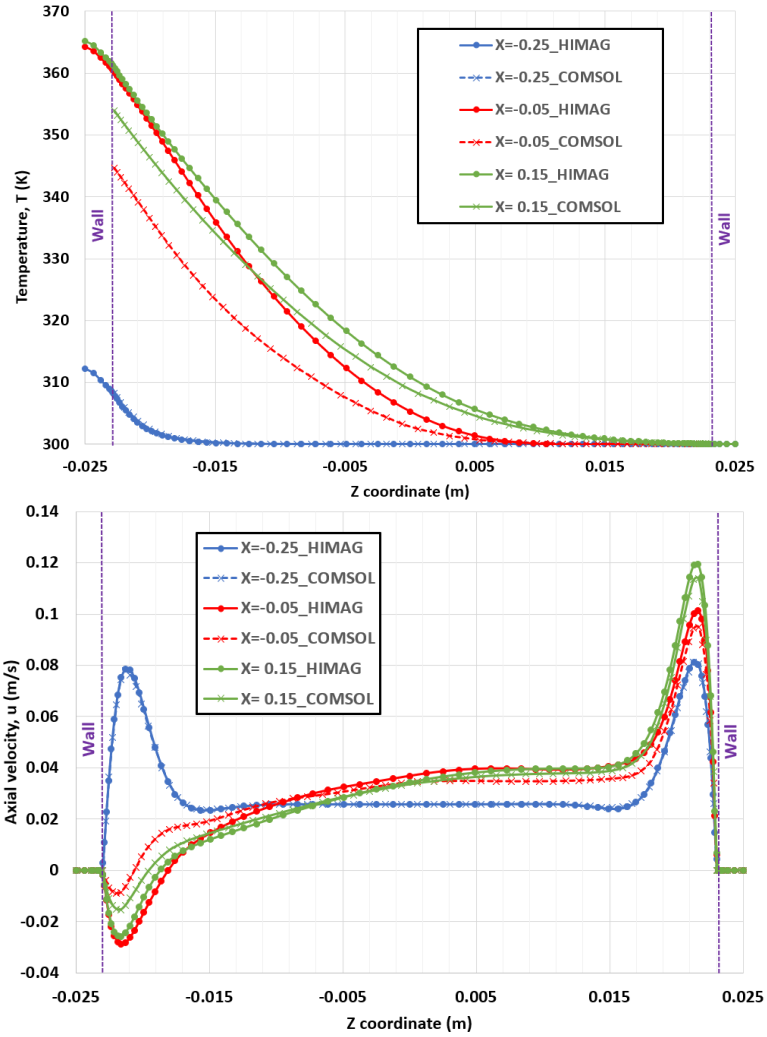

Note. Comparison of 1D distributions of time averaged velocity u and temperature T are plotted between COMSOL and HIMAG codes at different axial location.

Figure 21: *Contour Plots of Temperature and Flow Distribution of Mixed-Convection Downward Flow in a Vertical Duct*

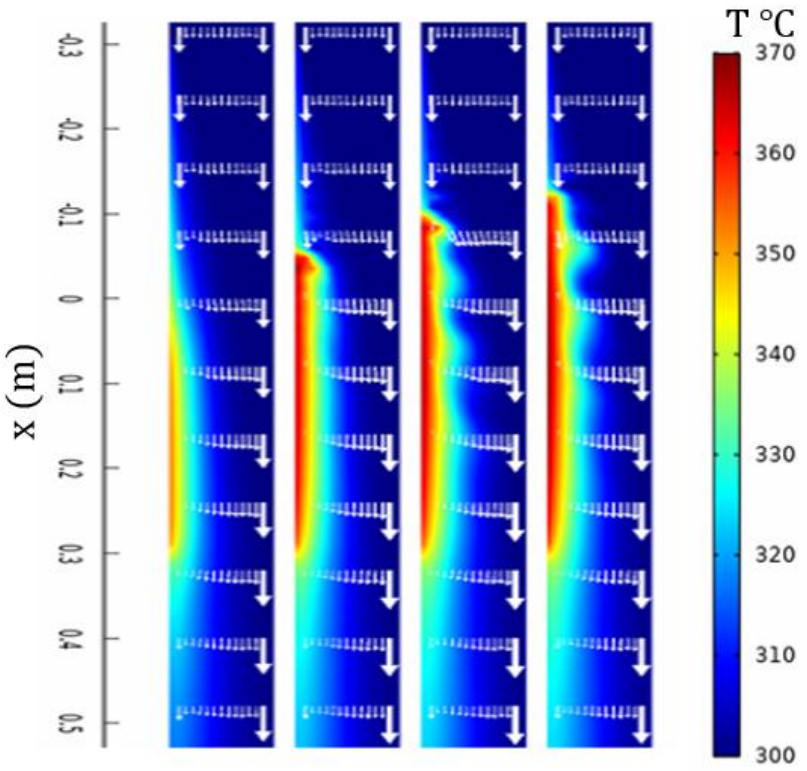

Note. Contour plots of instantaneous temperature T and arrow surface of velocity at different time from left to right: t = 40 s, t = 110 s, t = 170 s, t = 240 s.

Upon entering the heated region, a thermal boundary layer initiates development on the heated wall as heat propagates into the LM flow. The buoyant force, opposite to gravity and flow direction, influences the warm fluid, causing a slow temperature to increase as the LM descends along the heated wall. As the flow becomes more buoyant, the velocity near the heated wall diminishes, resulting in an asymmetric velocity profile (Fig. 21, x = −0.20 m). Moving farther downstream, when the buoyant force surpasses the pressure gradient, the flow near the heated wall stagnates and then reverses, generating sufficient viscous and electromagnetic forces to balance the buoyancy. This leads to the formation of a recirculating flow profile, where hot fluid

moves upward along the hot wall, and cold fluid moves downward at the opposite wall (Fig. 21, x = 0.03 m). The characteristic flow patterns during the transition from the M-shaped velocity profile to the reversed flow include the separation of the boundary layer, occurring shortly downstream from the beginning of the heated region, and the formation of a reversed flow bubble near the heated wall, extending over approximately half of the length of the heated zone.

The prevailing quasi-two-dimensional (Q2D) flow dynamics undergo a shift near the separation point of the boundary layer at the initiation of the reversed flow bubble, where the flow exhibits some three-dimensional (3-D) features. As evident from Fig. 21 and Fig. 21, within the heated zone, the flow achieves near-complete development between x = −0.1 m and x = 0.2 m, covering approximately half of the heated length. Toward the end of the heated region, the boundary layer reattaches to the heated wall, and the flow gradually redevelops toward the M-shaped velocity profile (Fig. 21, x = 0.40 m).

3.4.4 Comparison of COMSOL Simulations against other numerical results

The code-to-code validation of this type of flow scenarios was conducted through an internation cooperation including the author of this thesis involving five existing CMHD codes: HIMAG, COMSOL, ANSYS FLUENT, ANSYS CFX, and OpenFOAM [51]. The results discussed in this entire section (3.4.4) are generated from that research study [51].

In the previous study, results in both Fig.20 and Fig. 21 distinctly showcase the intriguing features of buoyancy-opposed mixed-convection MHD flow, including boundary layer development, formation of near-wall jets in the inlet section upstream of the heated zone, separation of the boundary layer from the heated wall with subsequent reattachment downstream, and the emergence of reversed flow. Notably, the specific details vary among the codes. The axial locations of the boundary layer separation point, and flow reattachment differ, and there are

slight discrepancies in the velocity and temperature distributions in the outlet section downstream of the heated zone. While all the codes effectively capture the fundamental flow physics, there are quantitative distinctions.

These variations are further evident in Fig. 22 and Fig. 23, depicting time-averaged 1-D temperature and velocity distributions. Notably, substantial differences emerge, particularly at the initial measuring station (x = −0.15 m). Among the five codes, COMSOL and OpenFOAM exhibit the lowest wall temperature on the heated side, presenting a velocity profile resembling the M-shaped profile but with a reduced velocity peak near the heated wall. In contrast, other codes manifest a reversed flow velocity profile at this station.

Figure 22: *Time-averaged Temperature at Five Locations along The Heated Section Length*

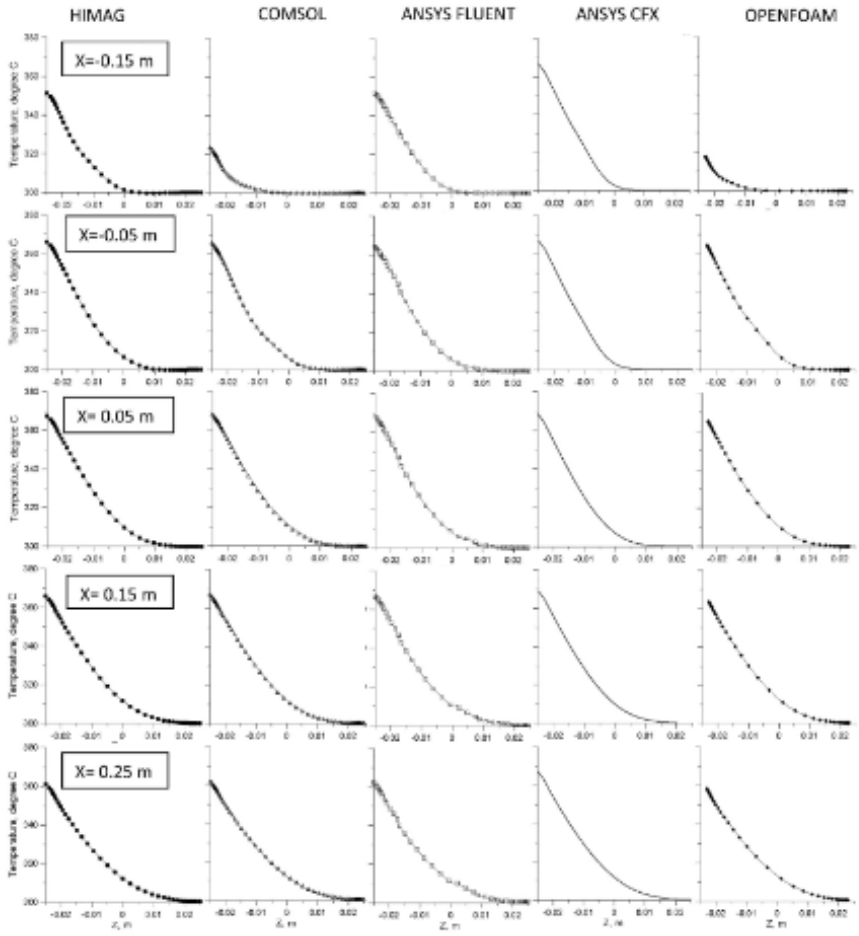

Figure 23: *Time-averaged Axial Velocity at Five Locations along The Heated Section Length*

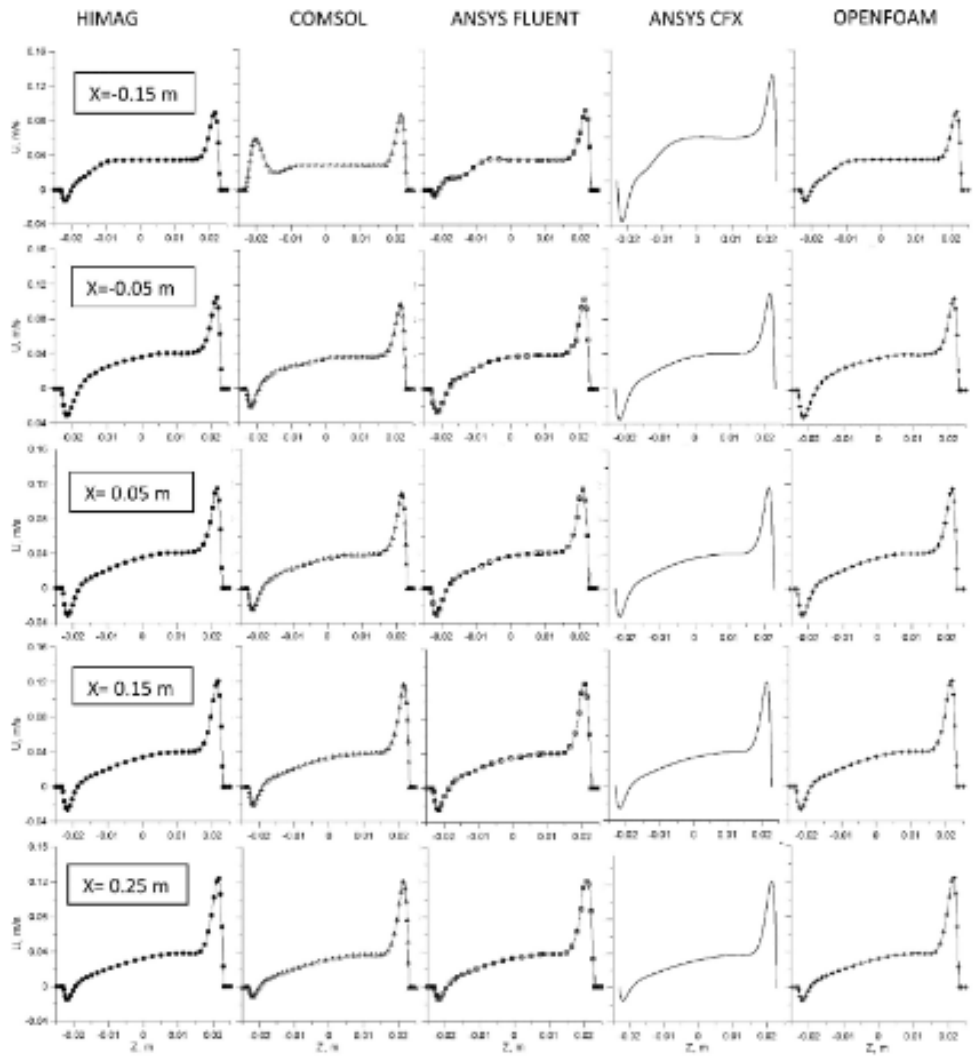

Moving downstream to the second measuring station at x = −0.05 m, which is nearly at the center of the heated zone, all codes converge to display remarkably similar temperature and velocity distributions. Within the region spanning from x = −0.05 to x = 0.15 m, all codes predict a fully developed flow, as indicated by the absence of visible variations in the velocity field (Fig. 23). In this fully developed flow, the velocity profile is highly asymmetric, with a minimum negative velocity of approximately −0.035 m/s near the heated wall and about 0.12 m/s near the opposite wall.

Fig. 24 highlights significant disparities in the time-averaged temperature at the duct axis. Although all codes anticipate a monotonic temperature increase initially, followed by non-monotonic behavior with two local peaks near x ≈ 0.15 and x ≈ 0.9 m, the peak temperatures differ. Specifically, ANSYS FLUENT and ANSYS CFX produce very close temperature curves, distinct from the other three codes. The highest temperature, approximately 19°C, is predicted by COMSOL at the first peak. Moreover, COMSOL exhibits a higher temperature at the first peak and a lower temperature at the second peak, while the other codes follow an opposite trend. These temperature variations along the axial coordinate correspond to significant changes in the velocity field as the flow evolves downstream, initially experiencing buoyancy forces within the heated zone and subsequently being influenced by robust electromagnetic forces linked to the axial currents in the fringing magnetic field zone.

Figure 24: *Time-averaged Temperature at the Center of Transverse Plane*

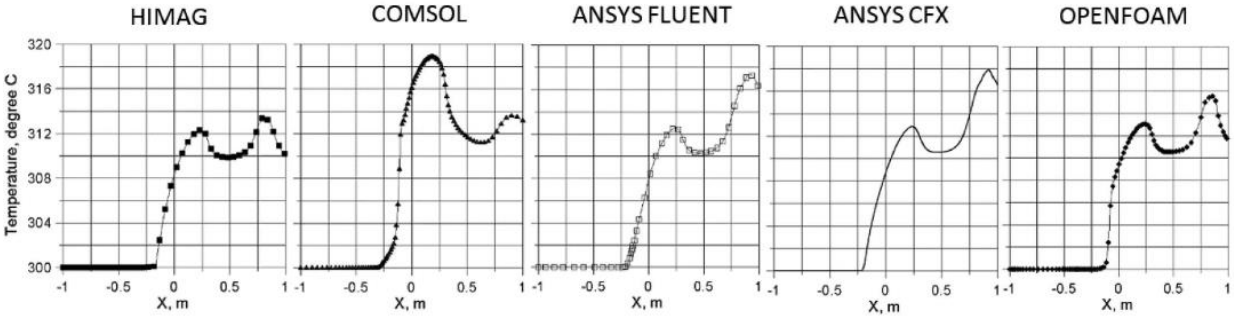

Fig. 25 illustrates the time-averaged mean bulk temperature, providing crucial data for verifying energy conservation in each computation. Specifically, the computed temperature difference ΔT between the flow inlet and outlet should align with a straightforward analytical prediction derived from the energy balance in the flow:

$$q'' S_q = \rho U_0 4b^2 C_p \Delta T \tag{20}$$

where S_q is the area of the heated section and ρ and C_p are the PbLi density and specific heat capacity specified in Table 3.

Figure 25: *Time-averaged Mean Bulk Temperature along Flow Direction*

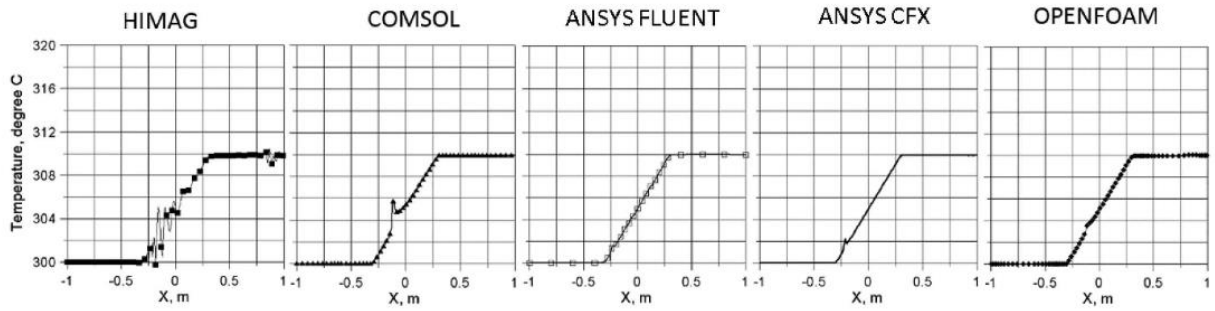

Note. Time-averaged mean bulk temperature was not provided in HIMAG, which used instantaneous mean bulk temperature instead.

From this formula, ΔT is calculated to be 9.95 K. Fig. 25 demonstrates that all five codes predict the same ΔT, which aligns closely with the temperature difference calculated from the formula. An interesting observation is that two codes, COMSOL and ANSYS CFX, exhibit a local peak in the mean bulk temperature near the boundary layer separation point. A minor deviation from linear behavior is also noticeable at the same location in the OpenFOAM results. As mentioned earlier, there are discrepancies among the codes in predicting the location of the boundary layer separation point, as illustrated, for instance, in Fig. 23. To highlight these distinctions, a time-averaged velocity dU/dz on the heated wall is plotted in Fig. 26 as a function of the axial coordinate. The condition dU/dz = 0 indicates the boundary layer separation point.

Figure 26: *Time-averaged Wall Shear Stress at y = -0.023 m and z = 0*

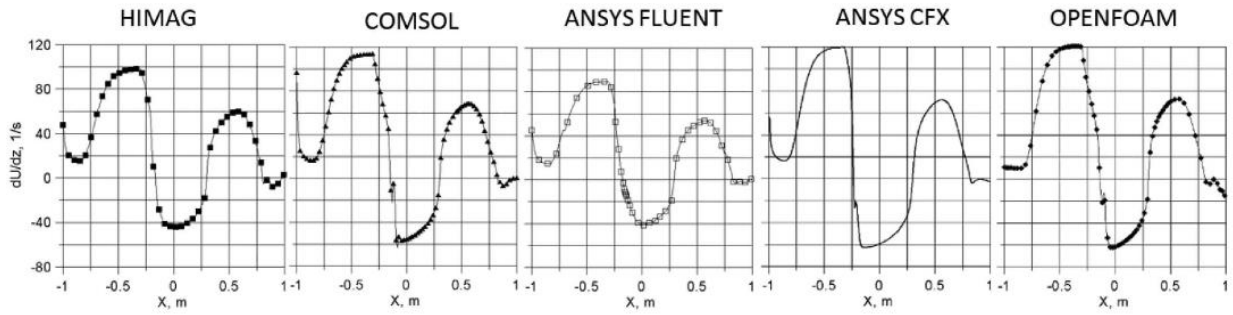

An essential computational consideration involves the capability of a code to accurately replicate the time-dependent behavior of the flow. Many LM MHD flows in a breeding blanket are anticipated to be time-dependent, showcasing quasi-two-dimensional (Q2D) turbulence [29]. Furthermore, experimental conditions often feature buoyant flows with fluctuations [23,24]. Three codes of HIMAG, COMSOL and OpenFOAM have predicted substantial velocity and temperature pulsation, as depicted in Fig. 27 for the temperature field and Fig. 28 for the velocity field. In contrast, the two other codes, ANSYS FLUENT and ANSYS CFX, do not exhibit any fluctuations.

Figure 27: *Temperature Fluctuation Behavior in HIMAG, COMSOL, and OpenFOAM*

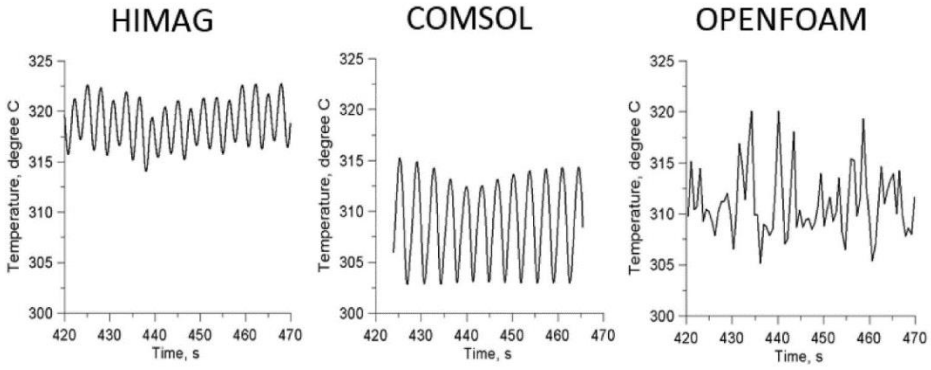

Note. HIMAG data at x = 0, y = 0.00575 m, and z = −0.00575 m. COMSOL data at x = 0, y = 0, and z= 0. OpenFOAM data: x = 0, y = 0, and z = 0. ANSYS CFX and ANSYS FLUENT have shown no fluctuations in time.

Figure 28: *Three Component of Velocity Fluctuation Behavior in HIMAG, COMSOL, and OpenFOAM*

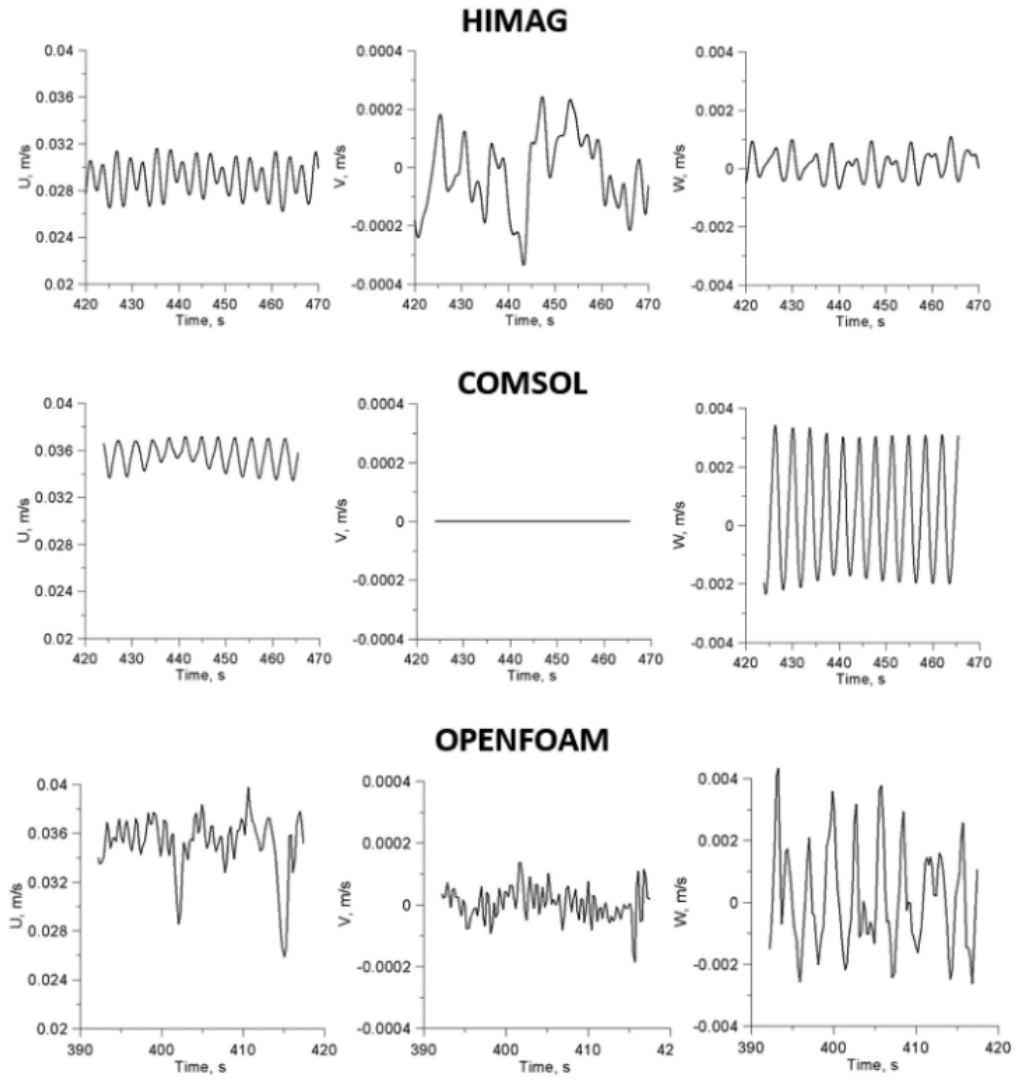

Note. HIMAG data at x = 0, y = 0.00575 m, and z = −0.00575 m. COMSOL data at x = 0, y = 0, and z= 0. OpenFOAM data: x = 0, y = 0, and z = 0. ANSYS CFX and ANSYS FLUENT have shown no fluctuations in time.

Analyzing the velocity pulsations in Fig. 27, it can be inferred that turbulence manifests itself in the unique form of Q2D turbulence. This is evident as the pulsating velocity component in the direction of the applied magnetic field (V) is two orders of magnitude lower than the axial velocity pulsations (U) and at least one order of magnitude lower than the transverse velocity pulsations (W) It is noteworthy that, although COMSOL computations confirm the fluctuating nature of the flow, no fluctuations are visible in Fig. 27 for the V velocity component. This is a consequence of the symmetry boundary conditions employed in the COMSOL computations at the duct midplane y = 0 to reduce the computational domain to half-size.

Velocity and temperature fluctuations displayed in Fig. 27 and Fig. 28 can also serve to estimate the characteristic frequency. Low frequencies dominate in all computations that were able to capture the fluctuating behavior, approximately at 0.3 Hz. Despite the three codes exhibiting similar amplitude and frequency characteristics, the time-dependent behavior is evidently not identical. COMSOL demonstrates near-harmonic fluctuations, whereas results computed by HIMAG and, especially, by OpenFOAM are more irregular. This might be partly attributed to different locations of the monitoring point in the computations. The two ANSYS codes appear too dissipative, possibly due to the use of upwind schemes by both codes. Although both codes employed a second-order upwind scheme, where the schematic viscosity is partially compensated, they were unable to reproduce the fluctuations, unlike HIMAG, COMSOL, and OpenFOAM. The absence of oscillations in the computations by the two ANSYS codes is also evident in Fig. 29 for instantaneous temperature.

Figure 29: *Instantaneous PbLi Temperature Distribution along the Duct Axis (y=0, z=0)*

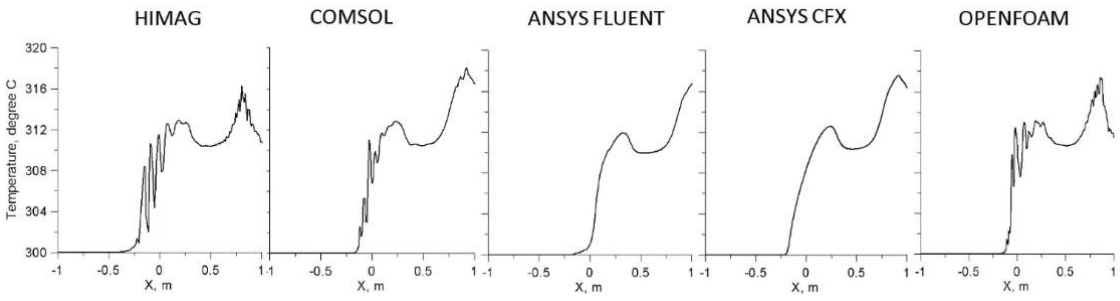

3.5 Conclusion of Code Validation Activity and New Model Development

In conclusion, the numerical methodology employed for solving MHD-heat transfer flow problems in COMSOL Multiphysics demonstrates a systematic approach with the integration of built-in physics modules and user-defined features allowing for tailored modeling, enhancing flexibility and precision. The validation and verification activities, including comparison with analytical solutions and experimental data, further attest to the robustness and accuracy of the implemented methodology.

A novel numerical model in COMSOL Multiphysics that enables the simultaneous coupling of MHD and heat transfer equations for fully developed flows, filling a critical gap in previous estimations that lacked consideration of either heat transfer effects or the coupling between MHD and heat transfer equations. By decomposing the absolute temperature into mean temperature and fluctuation components, the model ensures results independent of flow direction (may lead the elevator effect), facilitating comprehensive analysis. The model is designed to characterize important flow behaviors such as pressure drop, flow reversal, and velocity and temperature distributions, particularly relevant for LM blanket designs in fusion applications.

In the investigation into buoyancy-driven magnetohydrodynamic (MHD) flows, particularly focusing on mixed-convection flow patterns, the predictive capability of flow feature

and heat transfer phenomena have been conducted among five different candidates including: HIMAG, COMSOL, ANSYS FLUENT, ANSYS CFX, and OpenFOAM. While overall predictions for time-averaged flow and heat transfer were consistent across the codes, notable variations were observed in the location of the boundary layer separation point, highlighting the importance of careful consideration of computational methodologies. Among the codes, HIMAG, COMSOL, and OpenFOAM successfully captured pronounced velocity and temperature fluctuations, whereas ANSYS FLUENT and ANSYS CFX struggled to reproduce the time-dependent flow behavior due to potential limitations associated with artificial viscosity. Nevertheless, the comparison suggests that all codes can effectively resolve critical flow features, making them suitable for predicting LM MHD flow behavior in fusion cooling applications. However, the need for caution in accurately capturing unsteady flow features, including instabilities and quasi-two-dimensional turbulence, is emphasized, particularly considering the relatively small magnetic field and duct size studied in this analysis compared to real fusion applications.

CHAPTER FOUR: SIMULATION OF FUSION BLANKET APPLICATION

In the realm of LM breeding blanket concepts for fusion power reactors, lithium or lithium-containing alloys consistently serve as the breeder material owing to lithium's role in tritium breeding, an essential component for sustaining fusion reactions. PbLi emerges as an appealing option due to lead's function as a neutron multiplier in relevant nuclear reactions. The conductive flow of LM, such as PbLi, faces significant MHD effects under the influence of potent plasma-confining magnetic fields, posing critical challenges across all LM blanket designs [1]. Additionally, the flowing liquid metals encounter substantial buoyancy forces due to steep temperature gradients induced by intense volumetric heat loads or surface heating within blanket conduits. The interplay between MHD and buoyancy forces, termed magneto-convection, holds the potential to dominate flow phenomena and influence the feasibility of various fusion LM blanket designs. Furthermore, the intricacies of flow behaviors and heat and mass transfer, influenced by magneto-convection effects, are heavily contingent upon the specific geometry of individual blanket concepts.

4.1 Water-Cooled Lithium-Lead (WCLL) Breeding Blanket

Water-Cooled Lithium-Lead (WCLL) breeding blanket is the most promising liquid breeder blanket concept for DEMO in the EUROfusion Work Package Breeding Blanket (WPBB) – 2018. It is composed of 16 sectors, each of which contains two inboard and three outboard Single Module Segments (SMS) [52,53]. In this thesis, the Water-Cooled Lithium-Lead (WCLL) module situated in the equatorial outboard (see Fig. 30) serves as the reference computational geometry in this study to investigate magneto-convection flow behaviors under fusion-relevant conditions. This outboard breeding module features two identical breeding cells staggered on each other in the poloidal direction, as depicted in Fig. 31. Each breeding cell is reinforced with

five poloidal plates and one long toroidal plate, dividing the breeding zone into six rectangular ducts that link to inlet and outlet manifolds, thereby leaving the breeding zone open (termed the plenum region) from the first wall to the edge of the stiffening plates. Operating within a temperature range of 295°C to 328°C and a pressure of 155 bar [52], cooling water is employed to extract heat via circular pipes immersed in the breeding zone. The geometric complexity introduced by these components in WCLL poses challenges for predicting MHD/heat transfer flow via numerical simulations. While some studies have examined steady-state MHD flow and heat transfer in simplified model geometries of WCLL blankets, none have obtained actual velocity and temperature distributions or the temporal evolution of MHD flows in a prototypical WCLL blanket design. Consequently, this study aims to 1) assess the modeling capability of COMSOL Multiphysics for time-dependent MHD/heat transfer flows in complex geometries, and 2) elucidate the flow behavior and heat transfer phenomena in the WCLL prototypical blanket design under fusion-relevant conditions.

Figure 30: *WCLL Equatorial Outboard Module Cell*

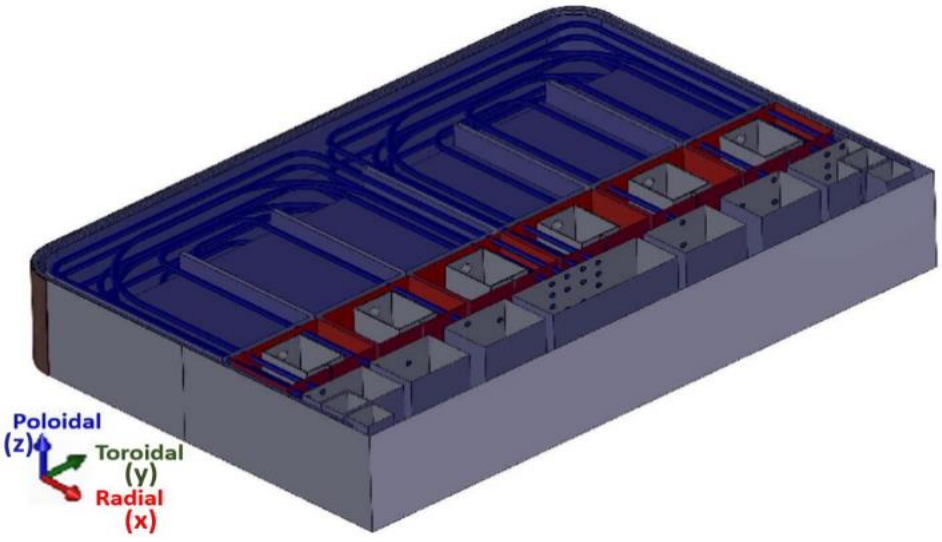

Figure 31: *Section View on Poloidal-radial Plane of WCLL Equatorial Outboard Module Cell*

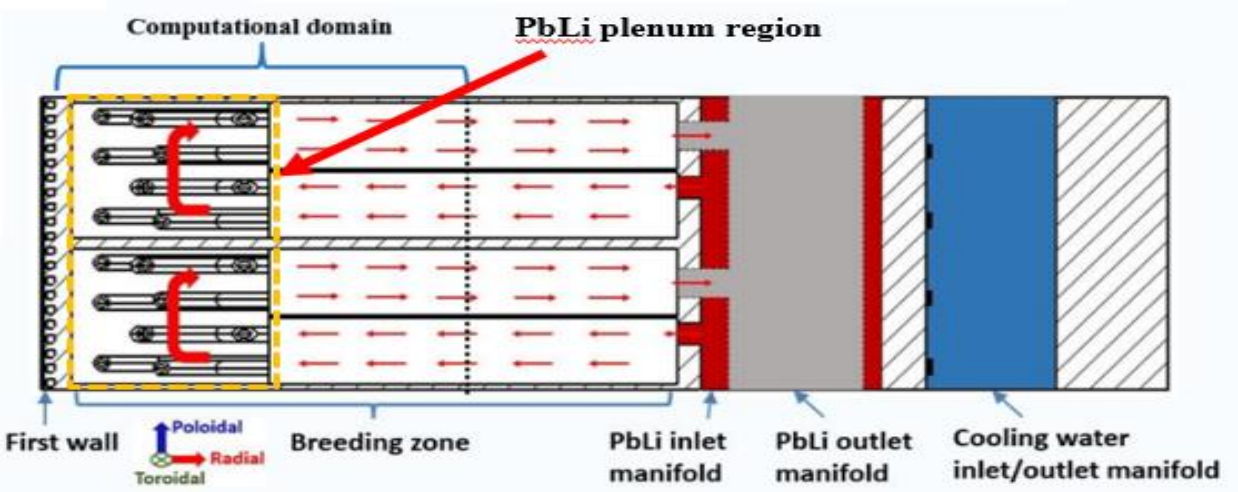

Note. PbLi flow path is demonstrated in red colored arrows and the blacked colored dash line formed the computational size (flow ducts are truncated in half) during the phase I simulations.

4.2 WCLL Blanket Formulation in COMSOL Multiphysics

In this study, the computational domain comprises one breeding cell, but only half of the cell in the toroidal direction is considered due to geometrical symmetry. Additionally, owing to the available in-house computational resources, the breeding cell is further simplified. The final simulation geometry (depicted in Fig. 32) is achieved through four key simplifications of the original blanket cell.

1: Simulating just one of the two identical breeding cells stacked in the poloidal direction proves to be adequate. This approach accounts for the electrical couplings present on the wall interface between the two cells, with such interactions being sufficiently addressed through special treatment, namely periodic boundary conditions.

2: A symmetry condition is applied to reduce the geometry by half, as all components within the WCLL blanket module exhibit symmetry relative to the central poloidal-radial plane.

This symmetry extends to the cooling effect generated by the water pipes within the breeding zone coolant, which also remains symmetric to the central plane.

3: The original module cell's first wall geometry, containing embedded cooling pipes, is excluded. In its place, a uniform negative surface heat flux (acting as a heat sink) is introduced to mimic the cooling effect. Although the flow of water coolant within the first wall may be technically asymmetric, this approach closely approximates symmetry with respect to the central.

4: In order to align with our current in-house computational hardware capacity, approximately 20 cm of inlet/outlet ducts formed by stiffening plates are excluded from the original blanket cell. This adjustment is not anticipated to impact the PbLi flow characteristics in the plenum region, as the development length of MHD duct flow is projected to be relatively brief in the presence of a strong transverse magnetic field.

Figure 32: *Computational Domain of WCLL Blanket Equatorial Outboard Module Cell*

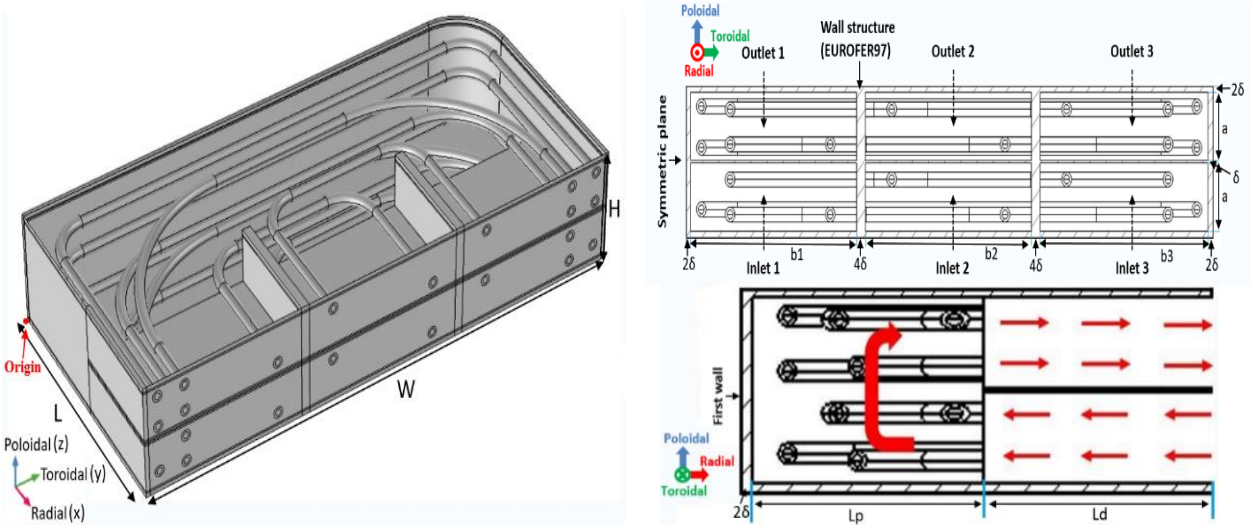

Note. Computational domain of WCLL blanket module cell in isometric view (left), section view on toroidal-poloidal plane (top right) and section view on radial-poloidal plane (bottom right)

Certain geometric parameters are illustrated in Fig. 32, appearing on both the side view and the front view of the computational domain, with their corresponding values listed in Table 4.

Table 4: *Computational WCLL Blanket Geometry Parameters, Length in (mm)* [53]

Parameter (Symbol)	Value	Parameter (Symbol)	Value
Radial length (L)	330	Inlet/outlet 1 width (b1)	231
Toroidal length (W)	731	Inlet/outlet 2 width (b2)	231
Poloidal length (H)	135	Inlet/outlet 3 width (b3)	233
Water pipe ID (d_i)	8	Inlet/outlet height (a)	61.5
Water pipe OD (d_o)	13	Breeder zone Inlet/outlet length (Ld)	150
Wall thickness (δ)	3	PbLi plenum length (Lp)	174

The magneto-convection flow in this thesis is governed by a combination of the incompressible Navier-Stokes equations with Boussinesq's approximation, Ohm's law, the electrical current continuity equation, and the energy equation, akin to the governing equations outlined in Chapter 3, section 1. The simulation utilizes the physical properties of the liquid breeder (PbLi) and the structural wall (EUROFER 97 steel), which are assessed at a temperature of 710 K (the midpoint within the PbLi operational range of 597 K to 823 K [53]). These properties are detailed in Table 5 for the structural wall, and Table 6 for the liquid breeder.

Table 5: *EUROFER97 Physical Properties, Evaluated at* $\boldsymbol{T_{ref} = 710\ K}$

Parameter (symbol)	Unit	Value
Thermal conductivity (κ_w)	$W/(m * K)$	29.21
Electrical conductivity (σ_w)	S/m	1.004×10^6

Table 6: *PbLi Physical Properties, Evaluated at* $\boldsymbol{T_{ref} = 710\ K}$

Parameter (symbol)	Unit	Value

Density (ρ)	kg/m^3	9672
Dynamic viscosity (μ)	Pa $*$ s	1.343×10^{-3}
Thermal conductivity (κ)	$W/(m * K)$	15.80
Specific heat (c_p)	J/(kg $*$ K)	188.5
Thermal expansion coeff. (β)	$1/K$	1.230×10^{-4}
Electrical conductivity (σ)	S/m	7.562×10^5

4.3 Numerical Modeling Procedures

4.3.1 Mesh Processes

A hybrid mesh, depicted in Fig. 33, is employed for the computational domain, comprising a combination of non-uniform parallelepiped, triangular prism, and free tetrahedral geometries. To evaluate the sensitivity of the mesh and ensure sufficient spatial resolution in boundary layers, the adequacy of the mesh resolution was assessed as the initial step using solutions from fully developed MHD flow applied to the geometry of the inlet 1 surface, illustrated in Fig. 34 (similar to the geometry in the study conducted by Bühler and Mistrangelo [54]). The calculated electrical potential and streamlines of electrical current density, depicted in Fig. 34, indicate the presence of internal boundary layers near the water pipes, a crucial feature for MHD flow in a duct with immersed pipes [54]. Comparison of pressure drop and maximum velocity quantities among different mesh cases, summarized in Table 7, reveals that case #3 exhibits insignificant changes with a continuously refined mesh. The element sizes corresponding to case #3 in boundary layers (Table 7) are 0.016 mm and 0.14 mm near the Hartmann walls and sidewalls, respectively.

Figure 33: *Example Overall Mesh Distribution in the Computational Domain*

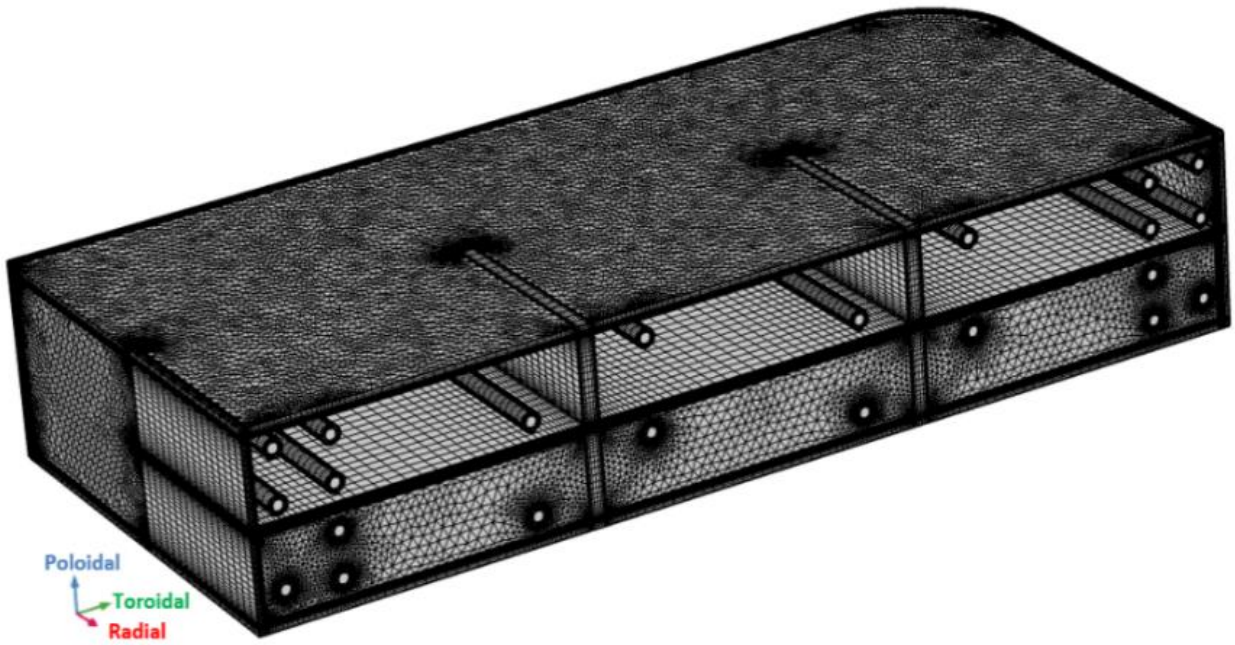

Figure 34: *Electrical Potential Distribution and Current density Streamline of Fully Developed MHD Flow on Inlet 1 Surface*

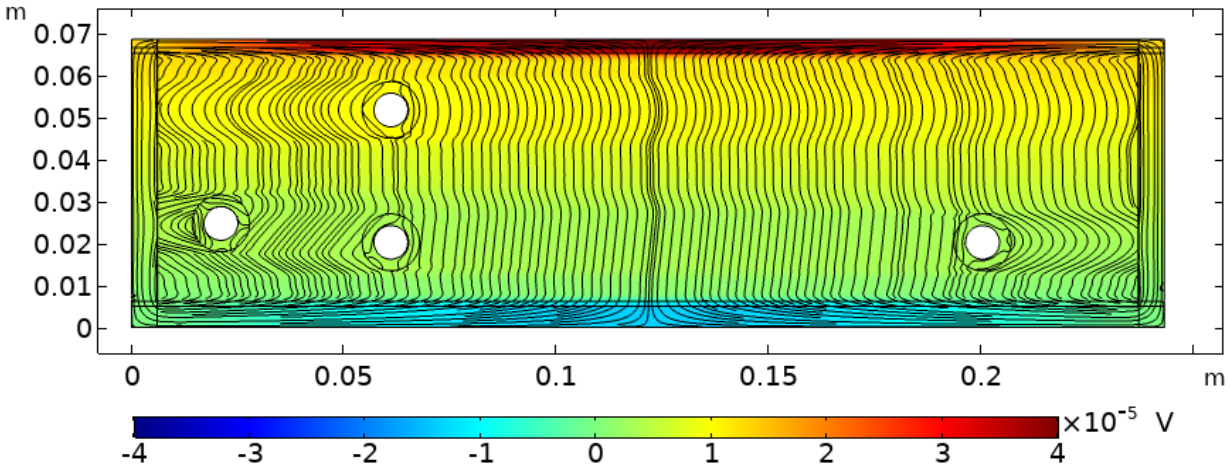

Table 7: *Mesh Refinement Study on Boundary Layers of Inlet 1*

Case	No. of Ele. within boundary layers			Pressure drop (Pa/m)	Maximum velocity (mm/s)
	Hartmann wall (δ_{Ha})	Side wall (δ_{Side})	Water pipe wall (δ_{WP})		
#1	4	5	5	70.279	1.299
#2	5	6	6	50.238	3.528
#3	6	8	8	50.151	3.518
#4	10	10	10	50.151	3.517

Note. The boundary layer thickness is defined as $\delta_{Ha} = b * \frac{\ln(Ha)}{Ha}, \delta_{Side} = \frac{b}{Ha^{0.5}}, \delta_{WP} = \frac{b}{Ha^{0.5}}$. Hartmann number in this study is defined as $Ha = bB_0\sqrt{\sigma/\mu} = 11530$, where the length scale $b = 0.5 * \frac{b_1+b_2+b_3}{3}$.

The subsequent phase of the mesh sensitivity investigation involved conducting 3D simulations of MHD/heat transfer using various mesh resolutions in the bulk region of the breeding zone, employing free tetrahedral elements to meet the resolution requirements established in the previous stage. Specifically, attention was given to examining and discussing the tetrahedral elements meshed in the bulk region, determined by the three parameters outlined in Table 8.

Table 8: *Mesh Refinement Study on Bulk Region of Breeding Zone*

Mesh case	No. of Ele.	Max. Ele. size (mm)	Min. Ele. size (mm)	Max. Ele. Growth rate (mm)	Max/Ave U (mm/s)	Max/Ave T (K)	Max T on pipe or structure wall (K)
Coarse	2.20 M	21.1	6.34	1.25	24.6/1.21	704/610	704/673
Normal	2.76 M	8.5	4.23	1.2	28.2/0.75	764/630	762/667
Fine	3.23 M	7.5	3.73	1.2	28.9/0.78	763/630	762/667

Based on the results in Table 8, the smallest element size in the bulk region measures 3.73 mm in the case of a fine mesh, upon which the present results were based. To counteract the

considerable increase in element size from the thin boundary layers to the bulk region, four stretching layers were introduced in between. The mesh analysis concluded with the initial layer thickness defined by δ_{Ha} and δ_{Side} (as specified in Table 7), with subsequent sizes increasing by 20% from one layer to the next. Consequently, the element sizes in these transitional regions adjacent to the bulk region measure 0.53 mm and 6.1 mm in the vicinity of the Hartmann walls and sidewalls, respectively.

4.3.2 Inlet/outlet and Boundary Conditions

Being relevant to fusion WCLL operational conditions [52,53,55], the input parameters and boundary conditions in this numerical modeling are listed in Table 9 and Table 10 respectively. Due to the fact that the decreased nuclear heating power (Eq. 22) in WCLL blanket at the end of the simulation domain is still nontrivial in this study (since in this simulation the radial length of the WCLL unit cell has been cut out to overcome the insufficient computational hardware capability), the gradient of velocity deduced from the buoyancy force normal to the outlets would be inconsistent with the boundary condition there. To eliminate this conflict, the nuclear heating

$$q_V(x) = \begin{cases} -98.962x + 9.5968, \left(\frac{MW}{m^3}\right) & \\ 365.35x^4 + 443.1x^3 + 215x^2 & \begin{matrix} 0<x<0.05\ (m) \\ 0.05\ (m)\leq x\leq L \end{matrix} \\ +54.376x + 6.8831, \left(\frac{MW}{m^3}\right) & \end{cases} \tag{22}$$

$$H(x) = \begin{cases} 1, \quad x < 0.03\ (m) \\ 0.5 + 0.9375 \cdot \left(\frac{0.18-x}{0.15}\right) \\ -0.625 \cdot \left(\frac{0.18-x}{0.15}\right)^3 + 0.1875 \cdot \left(\frac{0.18-x}{0.15}\right)^5 \end{cases}, \quad 0.03\ (m) \leq x \leq L \tag{23}$$

profile in this study is ramped down by multiplying a smoothed Heaviside function (Eq. 23) [56] from the unity to zero value at the last 10 cm from the outlets. Since our interest was to discover

the MHD/heat transfer phenomena in the plenum region and it should not be affected as the heating profiles in that region are prototypical to the WCLL nuclear heating profiles. Such modification should also not hinder our evaluation of this numerical code's capability - as one of the objects of this work. In Table 10, the effective thermal conductance on the interface between PbLi and cooling pipes (CP) is calculated from the thermal resistance circuit theory as

$$h_{PbLi/CP} = (1/h_{CP} + 1/h_{water})^{-1} = 3480\ \mathrm{W/m^2}K,$$

where $h_{CP} = 2\kappa_{wall}/d_i ln\ (d_o/d_i)$, and h_{water} is evaluated from Dittus-Boelter Correlation [57]

Table 9: *Input Conditions of WCLL Blanket Module Cell Simulation*

Parameter (symbol)	Unit	Value
PbLi inlet velocity (u_0)	mm/s	0.178
PbLi inlet temperature (T_0)	℃	325
First wall heat flux (q_0)	kW/m^2	-130
Cooling water temperature (T_{ext})	℃	312
Toroidal magnetic field strength (B_0)	Tesla	4
Nuclear heating power (q_V)	MW/m^3	$Eq.$ 22

Table 10: *Boundary Conditions of WCLL Blanket Module Cell Simulation*

Governing equations	Inlet	Outlet	Wall/PbLi interface
Navier-Stokes ($\boldsymbol{u}$, p)	$\boldsymbol{u}_0$	$p = 0$, $\nabla \mathbf{u} \cdot \mathbf{n} = 0$	Non-slip
Heat transfer (T)	T_0	$-\mathbf{n} \cdot \boldsymbol{\kappa} \nabla T = q$, $q = h_{PbLi/CP}(T_{water} - T_{wall})$ at PbLi/CPs $q = q_0$ at PbLi/first wall; $q = 0$ at other walls and outlet	
Electrical potential (ϑ)	Continuous at PbLi/wall interface; $\mathbf{n} \cdot \nabla \vartheta = 0$ at other walls and inlet/outlet		

4.3.3 Initial and Terminal Conditions

Prior to simulating magneto-convection flows in the WCLL blanket module cell, the temperature distribution with stagnant PbLi flow ($u = 0$) was initially computed shown in Fig. 35. Subsequently, the complete set of governing equations was solved using this temperature

field in conjunction with zero values of velocity and electrical potential fields as the initial conditions. The simulations were concluded by monitoring the temporal evolution of the averaged velocity magnitude (U_{avg}) and temperature (T_{avg}), as depicted in Fig 36 and Fig. 37. The simulations were terminated when the change in U_{avg} stabilized and the rate of decrease in T_{avg} became less than 0.05 K/s, corresponding to approximately 5% of the internal energy loss ($Q_{PbLi} = \iiint \rho C_p \frac{dT}{dt} dV$) compared to the total volumetric heating input power ($Q_v = \iiint q_v dV$). Although the temperature field may exhibit slight variations with increased computational time, any additional changes in thermal energy balance would not significantly affect the primary flow features and heat transfer behaviors.

Figure 35: *Temperature Distribution on Whole WCLL Blanket Computational Domain at Different Time*

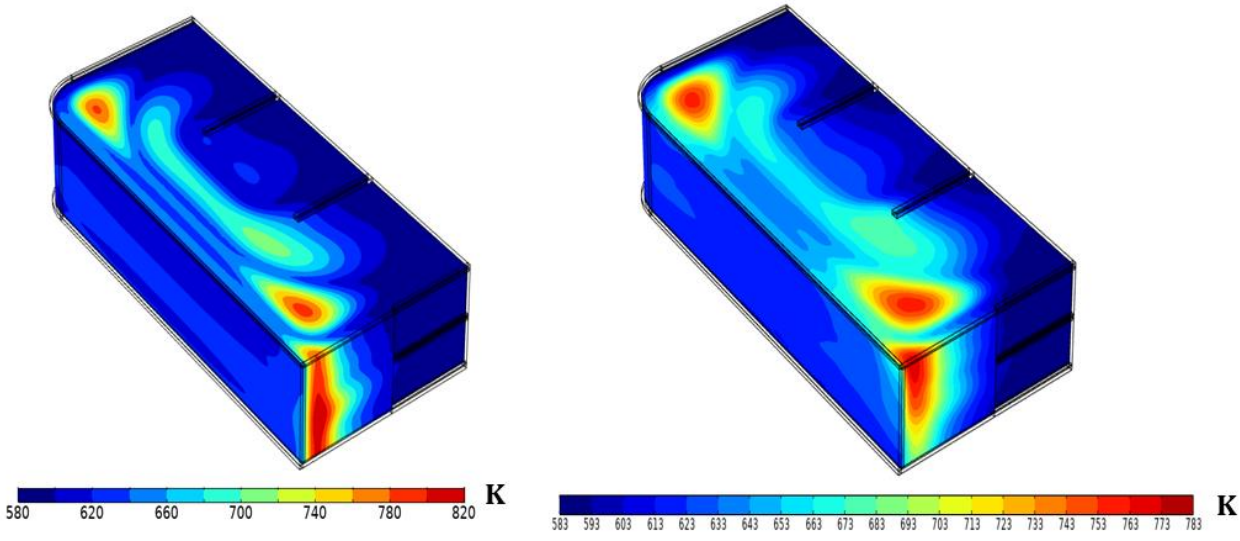

Note. The figure on the left is the temperature distribution at t = 0 s with PbLi is stagnant, and the figure on the right is the temperature distribution at t=68 s when the simulation is terminated.

Figure 36: *Time Evolution of Domain Averaged Velocity Magnitude on Normal and Fine Mesh Studies*

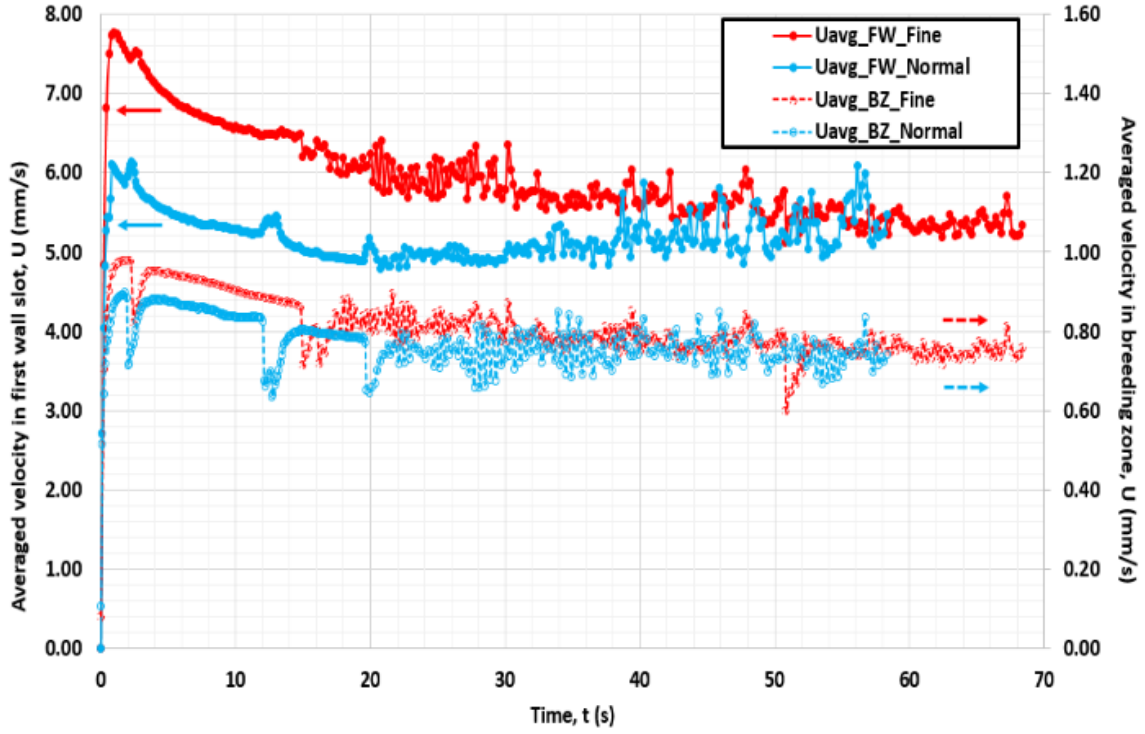

Figure 37: *Time Evolution of Domain Averaged Temperature on Normal and Fine Mesh Studies*

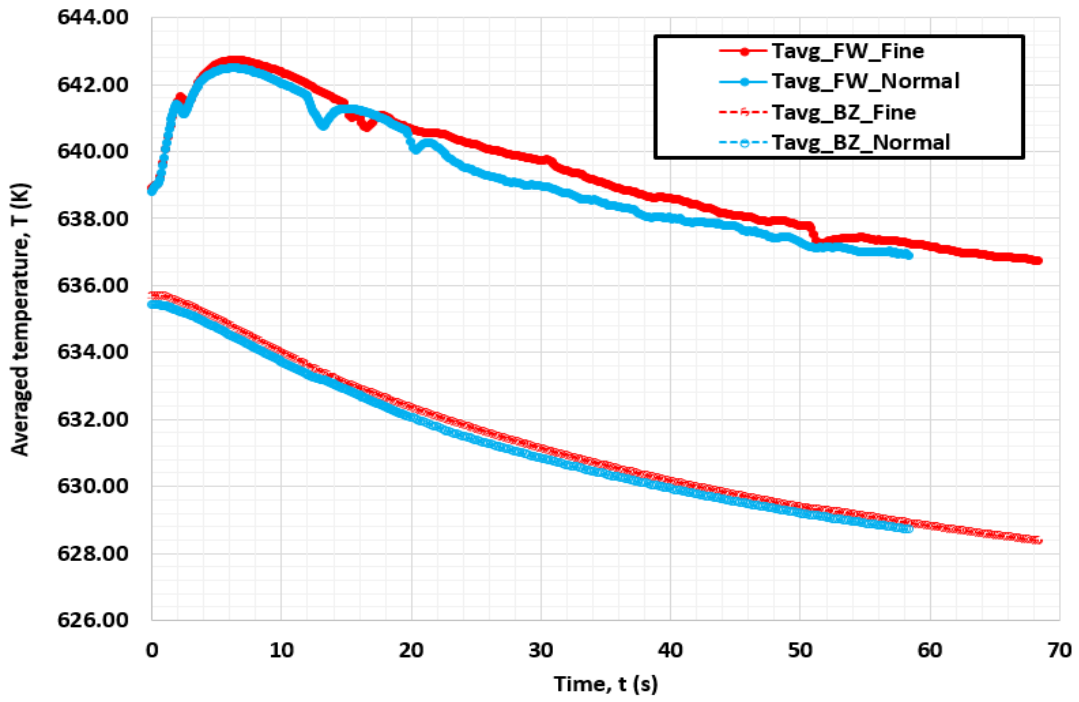

4.4 Results and Discussion

4.4.1 Mesh Sensitivity Study

To assess the feasibility of various mesh configurations (refer to Table 8), the simulation was initially conducted using a coarse mesh, revealing inadequate flow behaviors. As depicted in Fig. 38, which illustrates the mass flow rate calculated on all three inlet and outlet surfaces across three different mesh resolutions, the coarse mesh simulation yielded significantly lower flow rates in outlet duct 2, contrary to design expectations. Specifically, apart from the geometric asymmetry effects of inlet/outlet duct 3, the flow was not anticipated to deviate into neighboring ducts, suggesting that the outlet flow rates of each duct should be roughly equal. Considering the rounded corner of inlet/outlet duct 3, one would anticipate a slightly lower outflow in outlet duct 3 and slightly higher outflow in the other two ducts to compensate, as observed in the normal and fine mesh cases.

Figure 38: *Flow Distribution on Different Inlet and Outlet Ducts in Three Mesh Case Studies*

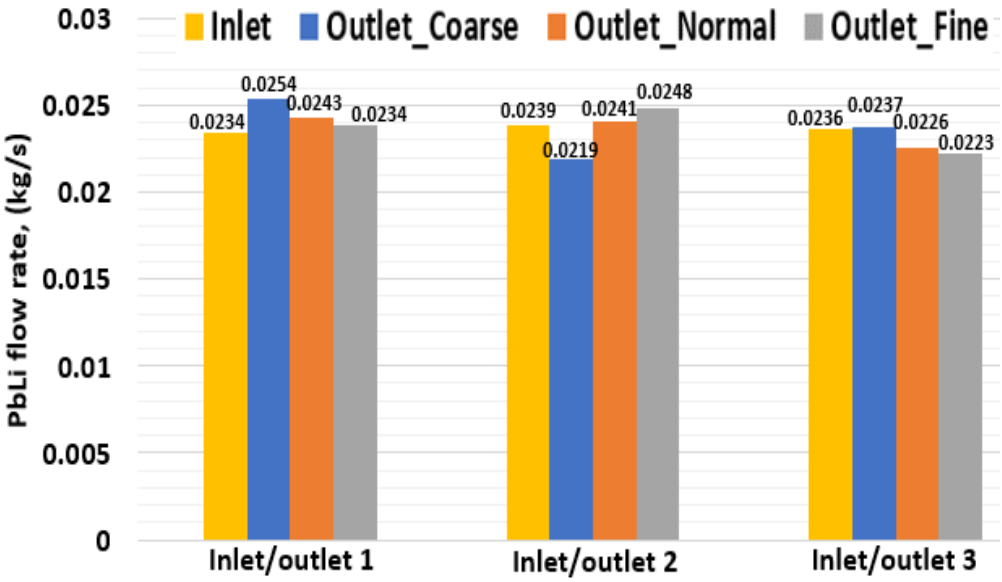

Additionally, apart from the discrepancy in flow rate, the coarse mesh employed a uniform inlet temperature as the initial condition for analysis. It was observed that significant development and computational time were required to meet termination conditions. Further analysis using a normal or fine mesh employed temperature distributions derived from stagnant flow as initial conditions. Time-evolutions of averaged velocity magnitude (U_{avg}) and temperature (T_{avg}) are depicted in Fig. 36 and Fig. 37, respectively, with two spatially averaged domains applied: 1) the entire breeding zone and 2) a y-z slot region (where radial-toroidal-poloidal notation is replaced by x-y-z as the coordinated system in this chapter) near the first wall, extending three times the side-wall boundary layer thickness (δ_{Side}), depicted by the blue shaded area in Fig. 39. As the flow evolution approached the termination timeframe, the variation of U_{avg} over time exhibited a qualitatively and quantitatively good match. Moreover, changes in T_{avg} were nearly identical across all time frames between normal mesh and fine mesh studies. Good agreements were observed in maximum and spatial averaged velocities and temperatures across the entire breeding zone and critical components at the final time step

between normal and fine mesh simulations. Specifically, with mesh refinement from the normal mesh study, differences of 2.5% and 3.7% were observed in maximum and spatial averaged velocities, respectively, with negligible differences in temperature for those areas of interest. Based on the comprehensive comparison presented in Table 8, as well as Fig. 36 and Fig. 37, the numerical data obtained from both mesh strategies were deemed adequate for the present study. Subsequent results discussed in this section were derived from simulations using the fine mesh and a flow time of 68 seconds (refer to Fig. 37).

Figure 39: *Flow Distribution on Different Inlet and Outlet Ducts in Three Mesh Case Studies*

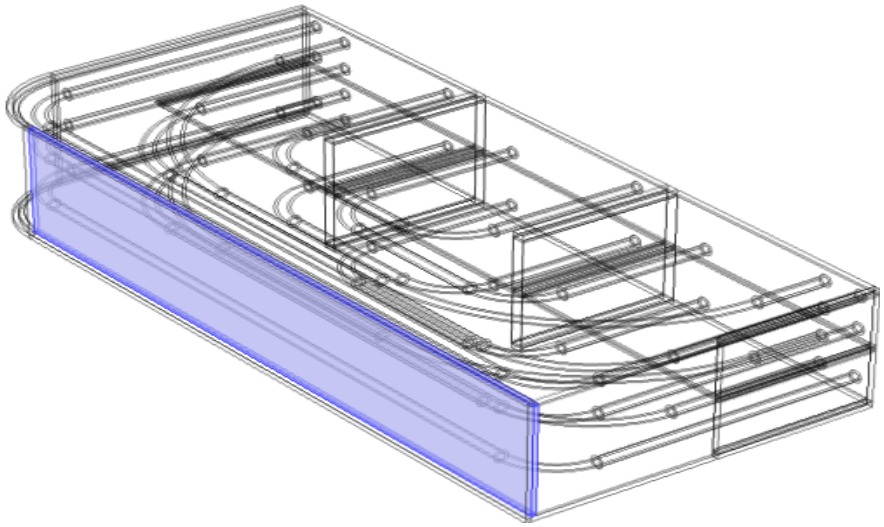

4.4.2 Mixed-convection MHD Flow and Temperature Dynamics in the Prototypical WCLL Module Cell

The simulations commenced with steep temperature gradients resulting from volumetric nuclear heating power, initiating upward flow motion due to buoyancy forces in the bulk PbLi plenum region. This motion evolved into two counterclockwise recirculations through the first wall boundary layer and clockwise through the edge of the stiffening plate (x = 18 cm) as depicted in Fig. 40 at t = 4 s. These counter-rotating flow circulations, varying in size, occupied

the entire PbLi plenum region. Concurrently, high-speed, laminar flow jets formed near the side-walls as shown in Fig. 41 at four different locations (Fig. 42) in plane B depicted in Fig. 43, aligned with the applied magnetic field direction, owing to strong MHD effects [37].

Over time, the temperature gradient in the plenum region decreased, evident from the temperature profile plots in Fig. 44. Consequently, the speed of flow circulations slowed at later times, as depicted in Fig. 40, while retaining their laminar nature and nearly identical shape, covering the entire plenum region. However, side-layer jets began to deform into unsteady vortices in all radial-poloidal planes (Fig. 40) by t = 20 s, transitioning the flow near the sidewalls from a laminar regime to a Type I flow instability regime [45] or unstable regime U1 [58] (fluctuation trend depicted in Fig. 36). These unsteady flow vortices traveled along the sidewalls, interacting with the boundary layers of nearby water pipes (Fig. 36 and Fig. 45). However, due to strong magnetic damping effects, these interactions remained weak and localized, with side-wall flow perturbations confined to the vicinity of the jet region, without spatial or strength growth, as illustrated by flow vortex dynamics identified by the Q criterion (Fig. 45). Such flow behaviors were also observed in experimental studies by Burr et al. [45] and Bühler and Horanyi [58]. By the end of the simulation, the change in temperature field across the breeding zone was insignificant when comparing its distribution between 48 s and 68 s in Fig. 48 (< 5 K temperature reduction in 20 s). Apart from minor and negligible changes in temperature distributions, bulk flow motion in the PbLi plenum region appeared to reach an approximate equilibrium state in the last 15 s of computational time, evident from comparisons between results at t = 68 s and time-averaged

Figure 40: *Surface Contour Plots of Velocity Magnitude and Streamline of u, w Components at Plane A-D Shown from Top to Bottom, and at Different Time Steps Shown from left to right.*

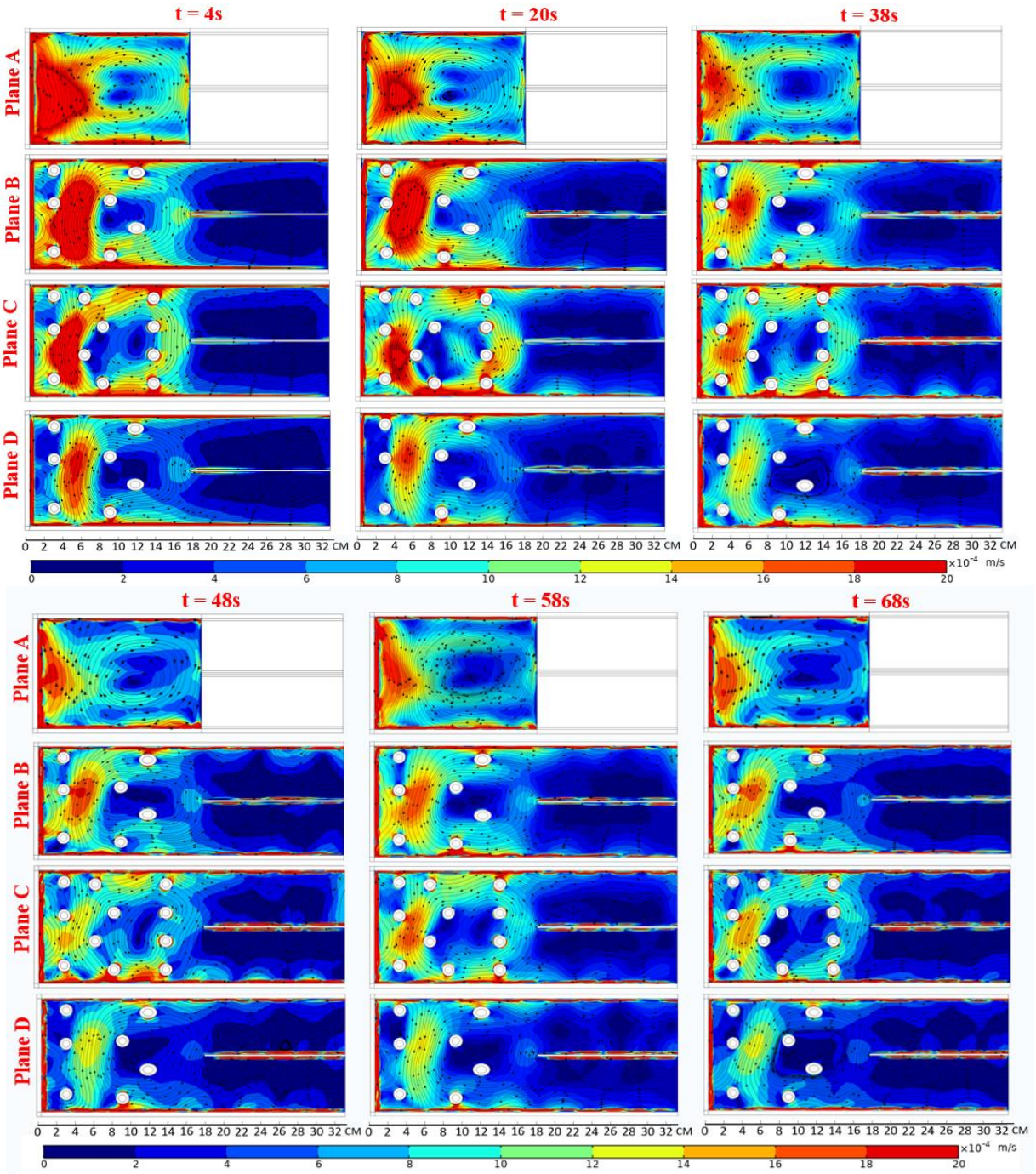

Note. Velocity magnitude exceeding 2mm/s is colored in red.

results from 53 s to 68 s as plotted in Fig. 46. As velocity distributions with three different time integrals in the last 15 s (plotted in Fig. 47) converged to the same profile, fluctuations near side-wall boundary layers also reached a statistically steady state (Fig. 48).

Figure 41: *1D Plot of Velocity u Component Distribution along z direction at different x locations (Fig. 45) in Plane B (Fig. 43)*

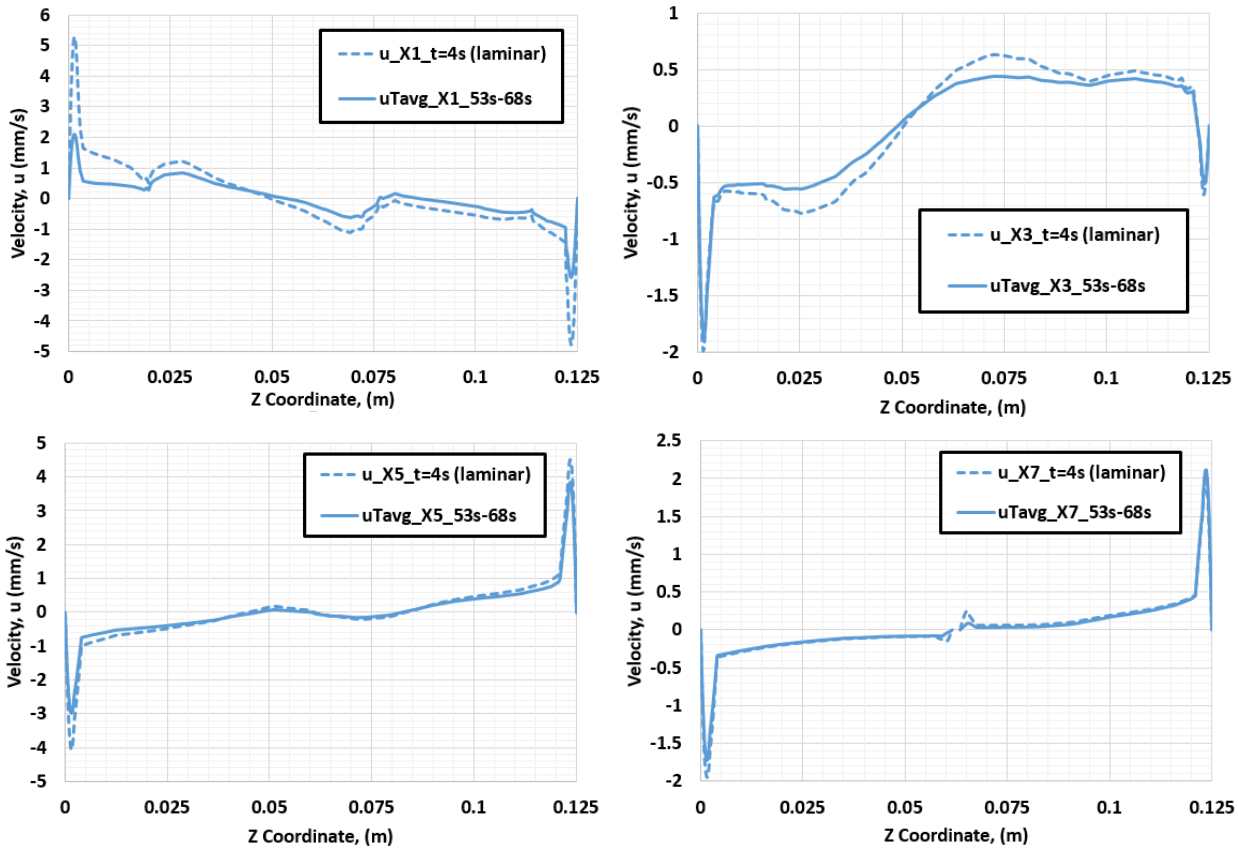

Figure 42: *Location of Four Reference Lines along z at Different x in Plane B (X1: x=23; X3: x=59; X5: x=171; X7: x=281 [mm])*

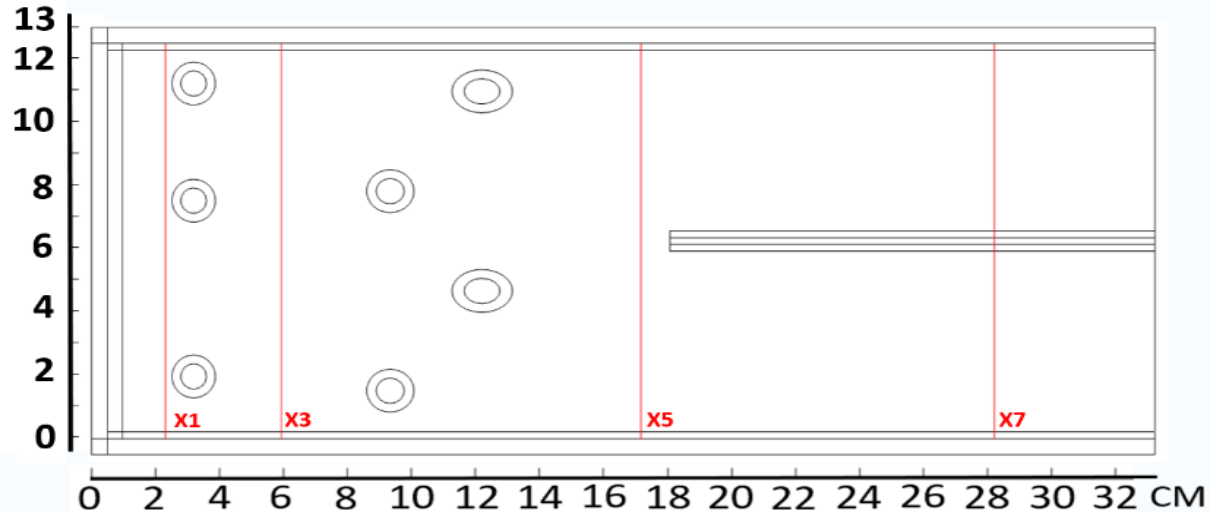

Figure 43: *Location of Four Radial-poloidal (x-z) Planes (A: y=0; B: y=121.5; C: y=346.5; D: y=607.5 [mm])*

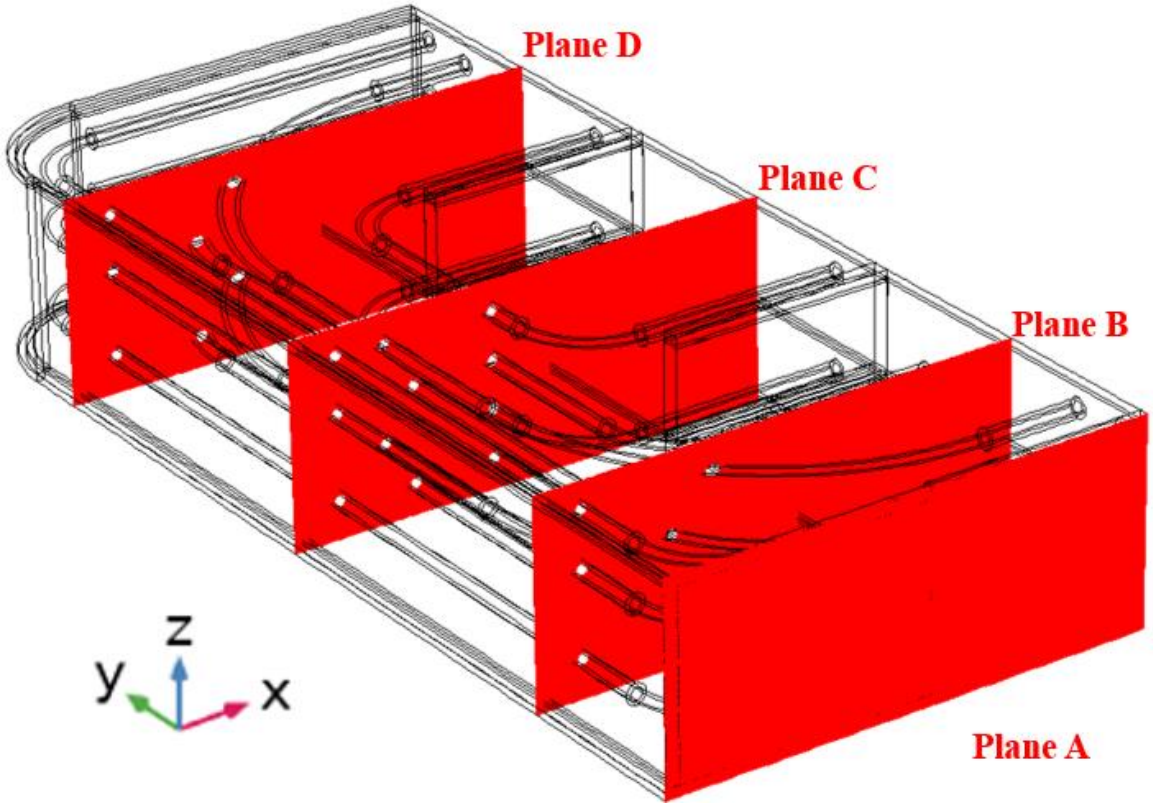

Figure 44: *Surface Contour Plot of Temperature on Plane A-D shown from Top to Bottom, and at Time t=0 s, t=48 s, t=68 s Shown from Left to Right*

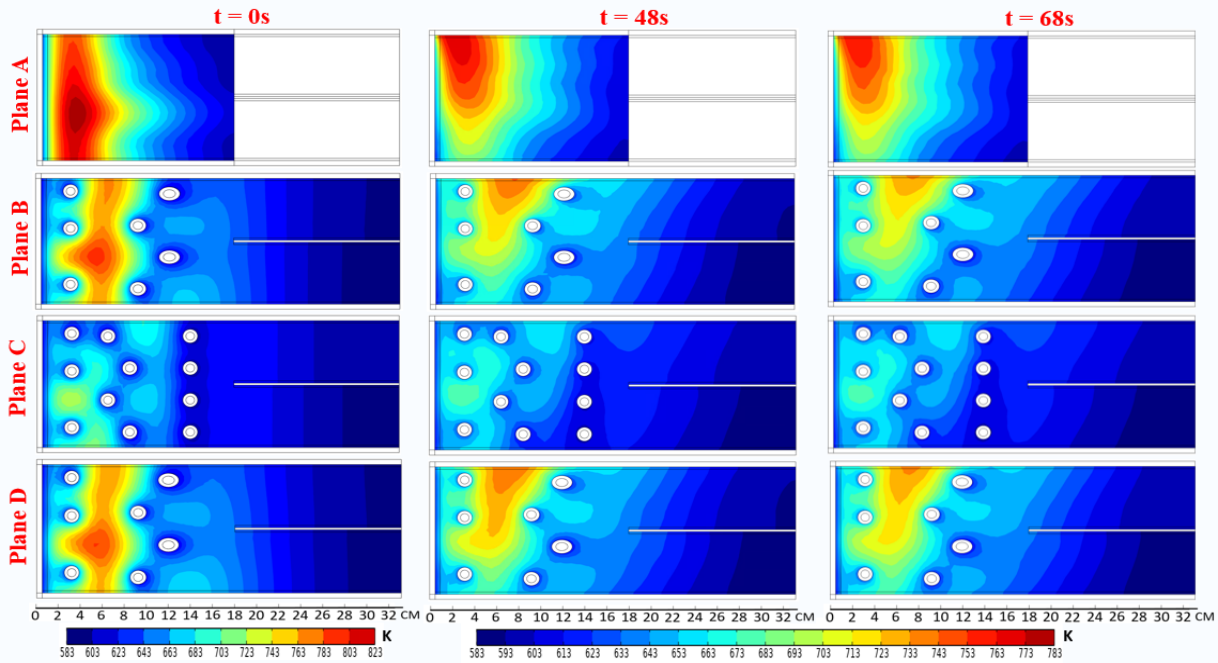

Figure 45: *Surface Contour Plot of Q Variable at Plane B at Different Time Steps Indicating the Flow Motions along the Side-wall Boundary Layers*

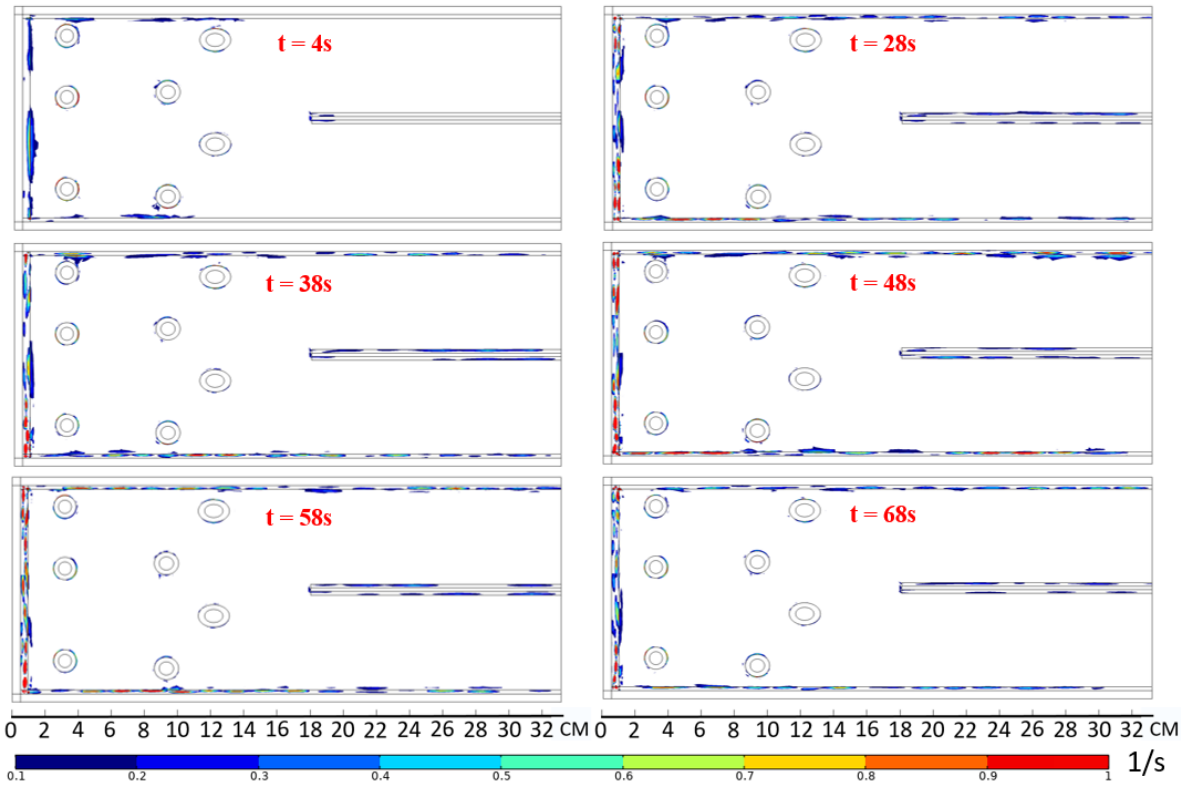

Figure 46: *Surface Contour Plot of Velocity Magnitude and Streamline of u, w Components at Plane A-D Shown from Top to Bottom, and at t=68 s (left) and Averaged from t=53 s to t=68 s (right).*

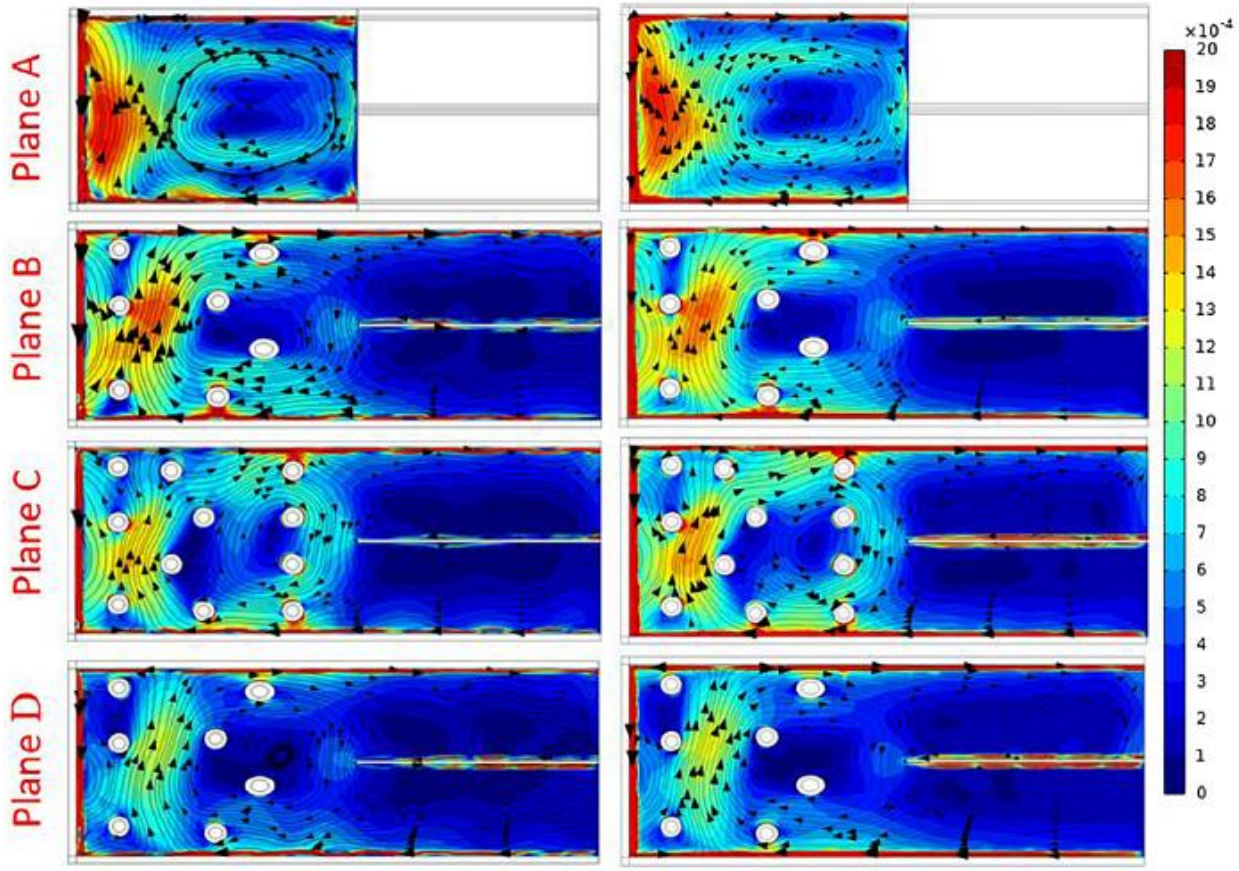

Note: Velocity Magnitude exceeding 2 mm/s is colored in red.

Figure 47: *1D Plots of Time-averaged Velocity Distribution with Different Time Integrals Along z Direction at Different x Locations in Plane B*

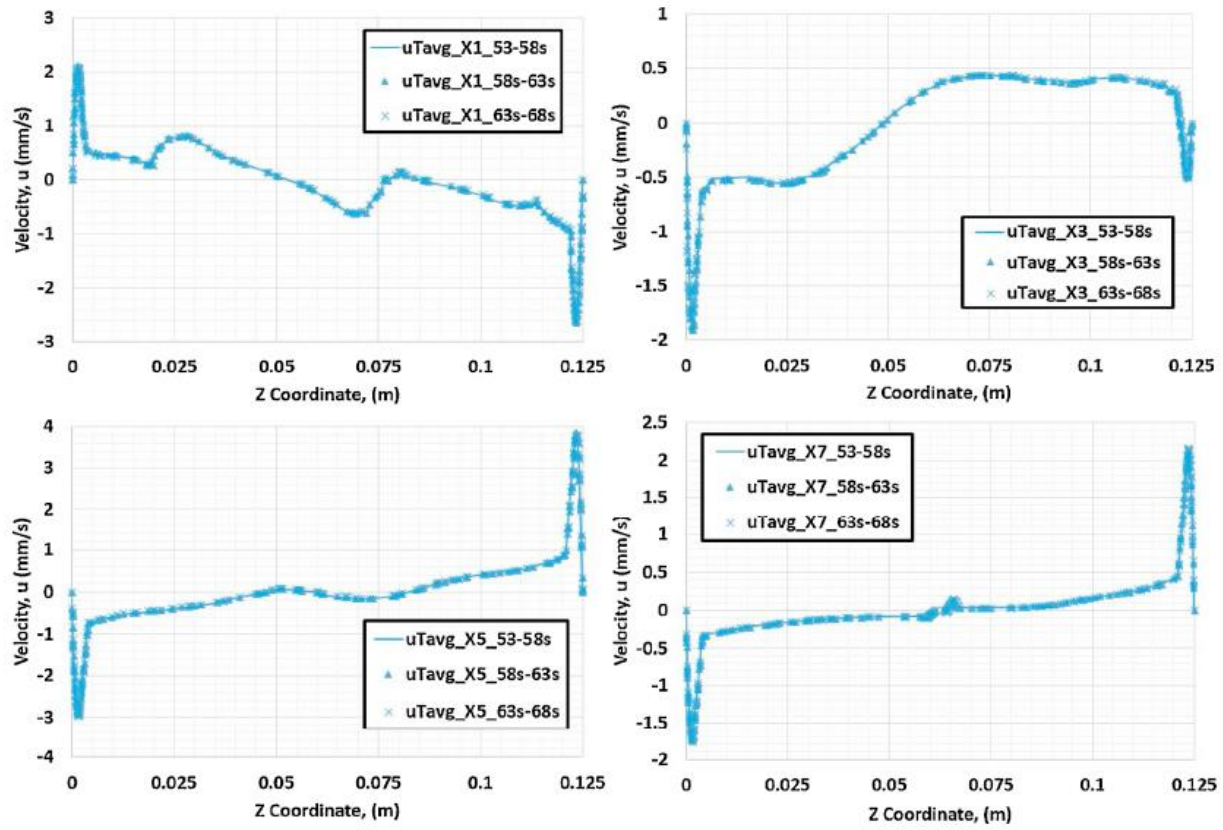

Figure 48: *Temperature Distribution on Whole WCLL Blanket Computational Domain at t=0 s (a) With PbLi is Stagnant and at t=68 s (b) Where the Simulation is Terminated.*

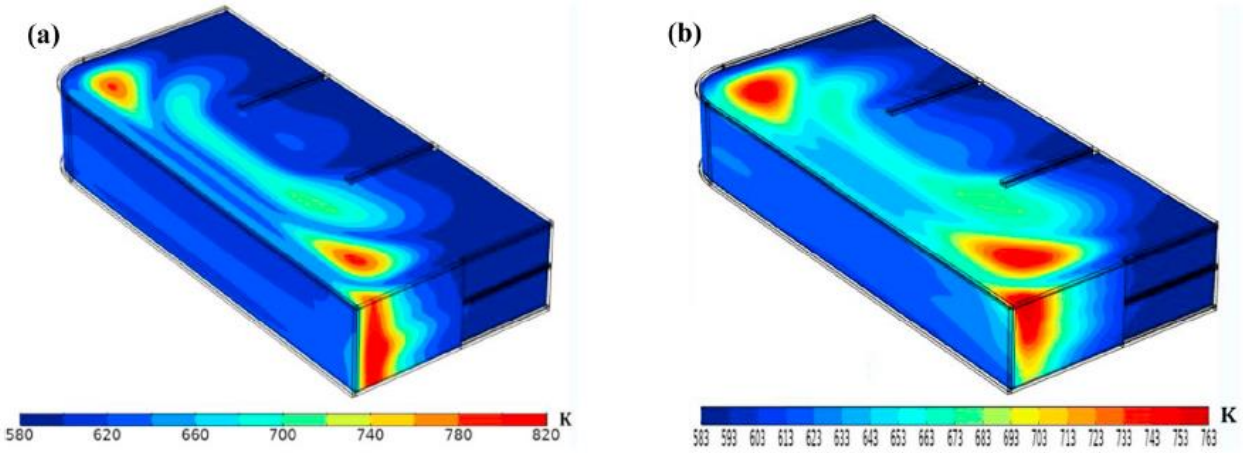

4.4.3 Discussion of the General Flow and Temperature Features of the WCLL Unit Cell Revealed in the Simulations

Due to the vigorous magneto-convection flow motion and the effective water-cooling system, the temperature across the entire domain decreases by 40–50 K from the initial temperature distribution (Fig. 18a–b), ensuring no hot areas with temperatures exceeding 825 K, the material limit of Eurofer 97 steel [59]. However, three spots persist on the top PbLi/wall interface with temperatures surpassing 723 K, potentially exceeding corrosion design criteria [60,61], as illustrated in Fig. 49. In contrast to other liquid metal breeding blankets [1], the PbLi flow in the WCLL blanket recirculates throughout the loop for tritium breeding and transport, without carrying the heat generated in the breeding zone. With fusion-relevant operational parameters applied in this study, the thermal energy removed by the PbLi flow amounts to 0.21% of the total heat generated in the PbLi region.

Figure 49: *Hot Spot Areas on Top Wall with Local Temperature Greater than 723 K in WCLL Module Cell.*

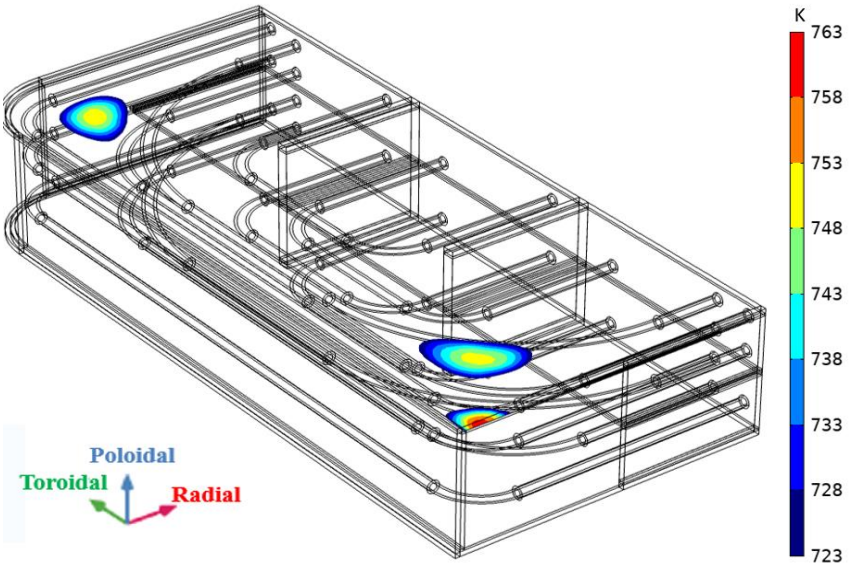

Figure 50: Time Averaged Bulk Velocity Magnitude and Temperature Distribution along Radial Direction at t = 68s

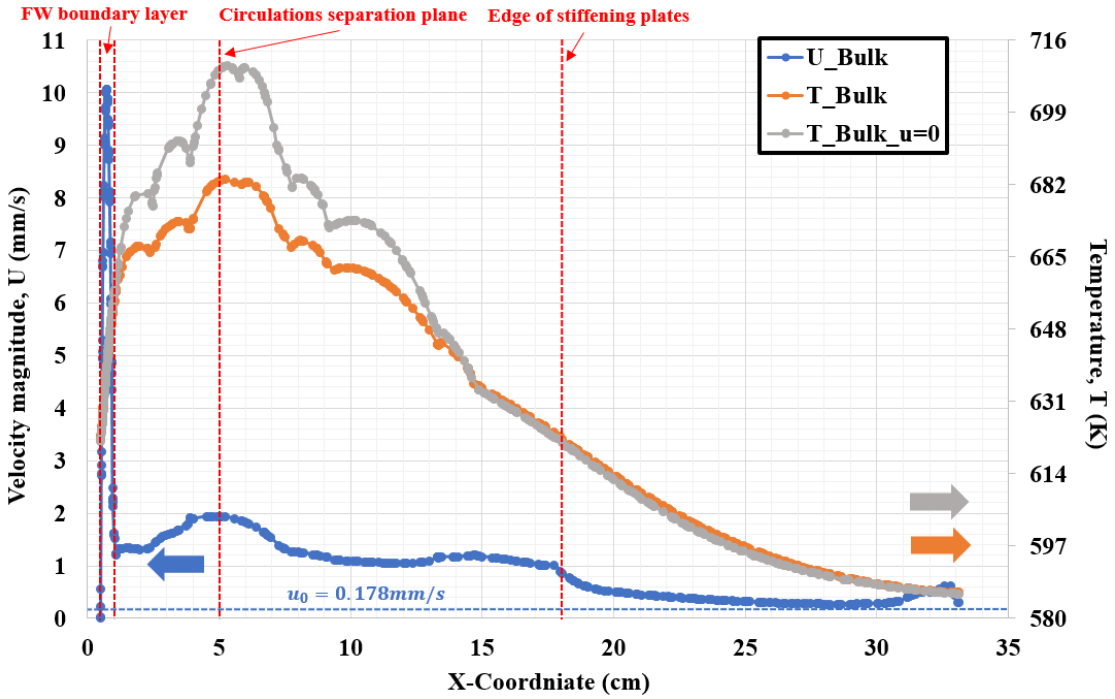

The bulk velocity and temperature distributions at the final time step along the radial direction (x) are plotted in Fig. 50 with calculation expression: $V_{bulk} = \frac{\iint V(x,y,z)dydz}{A(x)}$, where V represents either U or T for velocity magnitude and temperature respectively, and $A(x)$ is the integrated area of y-z plane at different x locations. As illustrated in this figure, the high-flow jet formed near the first wall exhibits a magnitude 70 times larger than the inlet velocity, potentially exerting a significant influence on heat and mass transfer. Despite the cooling effect of the magneto-convection fluid motion on the breeding zone, the temperature distribution in the inlet/outlet duct region remains largely unchanged, confirming that the bulk counter-rotating circulations predominantly recirculate in the plenum region. Moreover, the maximum temperature, with or without the advection effect, is observed at the same y-z plane (x = 5 cm),

indicating a separation of flow circulations at this specific plane, with most hot particles traveling upward toward the top wall.

4.4.4 Discussion of COMSOL Simulation Results

As part of the assessment of COMSOL Multiphysics' modeling capabilities, this simulation successfully captures several anticipated flow phenomena in the Water-Cooled Lithium-Lead (WCLL) concept. Initially, akin to the non-isothermal magnetohydrodynamic (MHD) recirculation in a rectangular enclosure, a natural convection-driven flow arises in the plenum region, depicted in Fig. 40 and Fig. 46. Moreover, due to the uneven volumetric heat generation, this recirculation splits into two counter-rotating circulations separated by the hottest zone, mirroring flow patterns observed elsewhere [62,63].

In addition to these circulations, the pronounced MHD effects engender high-velocity boundary layer flow jets, akin to the well-known MHD side-layer jet phenomenon in duct flows with electrically conducting walls, as documented by Hunt [16] and Hunt and Stewartson [17]. The intense viscous shear forces near the sidewall boundary layers prompt these high-speed jets to undergo transition into unsteady vortices. Prior simulations by Vetcha et al. [29] and experimental observations by Burr et al. [45] and Bühler and Horanyi [58] have noted such vortices, although their formation mechanisms at high Hartmann numbers, close to fusion operating conditions, remain under scrutiny.

Given the significant MHD effect relative to inertial forces in this study, these unsteady vortices remain confined near the sidewalls without penetrating the bulk region, akin to secondary instability observed at higher Reynolds numbers [29,64]. Moreover, comparing flow distribution plots on different x-y planes (Fig. 40) reveals that primary flow motions largely remain consistent along the magnetic field direction, except for localized deformations due to

geometric perturbations. This coherence along the magnetic field direction is characteristic of MHD flows subjected to sufficiently high applied magnetic fields, which tend toward quasi-two-dimensionality (Q2D) [65].

4.5 Conclusion

The modeling capabilities of COMSOL Multiphysics in analyzing magnetohydrodynamic (MHD) and heat transfer flows within a complex geometry, under conditions relevant to fusion applications, are scrutinized through simulations of magneto-convection flow within a representative Water-Cooled Lithium-Lead (WCLL) blanket module cell. This cell embodies significant geometric intricacies, akin to those encountered in a DEMO outboard scenario, while maintaining operational conditions akin to fusion environments.

By elucidating MHD flow characteristics documented in prior literature under similar conditions, COMSOL Multiphysics demonstrates its capacity to simulate fully coupled MHD and heat transfer equations within complex geometries, even under demanding fusion operational constraints. Serving as the inaugural numerical exploration of MHD and heat transfer flows within a prototype WCLL blanket module cell under pertinent fusion operating conditions, the present study unveils vital insights into magneto-convection flow behaviors and temperature distributions critical for assessing current WCLL breeding blanket designs.

Particularly noteworthy is the observation that flow within the PbLi plenum region, of paramount interest, is predominantly governed by natural convection, yielding two stable counter-rotating flow circulations. Despite mild interactions with sidewall-induced unsteady vortices, these flow patterns remain relatively stable. Additionally, this study marks the first calculation of temperature distribution within the domain, revealing that while the maximum temperature across the computational domain remains below the material temperature limit of

550°C, potential corrosion concerns arise as localized areas on the top structure wall exceed the corrosion temperature threshold of 475°C (723 K). Furthermore, the calculated thermal energy removed by the PbLi flow amounts to a mere 0.21% of the total heat generated within the breeding cell.

CHAPTER FIVE: CONCLUSION AND ACHIVEMENT

In conclusion, the transformation of the MaPLE facility into MaPLE-U highlights a significant advancement in magnetohydrodynamics (MHD) research, particularly regarding mixed convection MHD flows. Overcoming previous spatial constraints, enhancements to MaPLE-U have enabled experiments with various flow orientations relative to gravity. Key modifications, such as implementing a hydraulic lifting and tilting system, reconstructing the loop, and enhancing data acquisition and control systems, have greatly expanded the facility's capabilities. Although the extensive experimental investigations with MaPLE-U for mixed convection MHD flow have not yet carried out at UCLA by the time of this thesis, some of the preliminary results of temperature measurements have been acquired as the first world-wide mixed-convection MHD downward flow with the same fusion reactor breeding fluid (PbLi) and demonstrated the existence of flow reversal under strong buoyancy effect. Moreover, the design of the new test article reflects a meticulous approach to capturing complex flow behaviors, including flow reversal, across a wider parameter range. Incorporating elements with higher heating power and thermal insulation ensures precise control and analysis of temperature and heat transfer phenomena within the test section. Additionally, this new test article, currently in operation at the MaPLE-U facility at KIT, boasts increased heat flux capability and enhanced diagnostics, further advancing research capabilities. These advancements in MaPLE-U and the development of the new test article underscore a commitment to pushing the boundaries of MHD research. Furthermore, they challenge existing assumptions in LM MHD R&D by identifying a significant flaw in the global strategy, which had assumed complete laminarization of flow under strong magnetic fields. Correct modeling and experimentation must now simultaneously consider multiple factors such as heating, temperature gradient, buoyancy, and magnetic field.

The utilization of COMSOL Multiphysics for solving MHD-heat transfer flow problems reflects a methodical approach, leveraging built-in physics modules and user-defined features to customize modeling, thus enhancing adaptability and accuracy. Validation and verification activities, including comparisons with analytical solutions and experimental data, bolster the reliability and robustness of this methodology. The innovative numerical model developed in COMSOL Multiphysics, addressing a crucial gap in previous estimations, enables the fast simulation of MHD-heat transfer flow problems with simultaneous coupling of MHD and heat transfer equations with wide range of flow and thermal parameters relevant to nuclear fusion reactor conditions. It characterizes the vital flow phenomena like pressure drop, flow reversal, and generates velocity and temperature distributions, crucial for LM blanket designs in fusion applications and useful for future numerical code development and validation.

The development of liquid breeder blanket concepts for fusion power reactors, exemplified by the Water-Cooled Lithium-Lead (WCLL) breeding blanket, presents substantial engineering challenges due to intricate physical phenomena. Utilizing COMSOL Multiphysics, computational modeling offers crucial insights into flow patterns, temperature distributions, and heat transfer characteristics in prototypical blanket designs. These simulations underscore the importance of robust numerical modeling techniques to optimize blanket performance under fusion-relevant conditions. The extension of COMSOL modeling capability to complex LM blankets with 3D mixed-convection MHD flows has identified several issues for WCLL breeding blanket design including vital flow stagnation zones and hot spots crucial for tritium transport and heat transfer [66]. Moreover, the results from WCLL simulations highlight the importance of full geometry simulations in capturing essential flow features missed in truncated geometrical modeling.

Appendix A: MaPLE-U Facility and PbLi Flow Loop

Picture (A): a lift/tilting magnet system

Picture (B): a new how PbLi flow loop

Picture (C): data acquisition & control system

Picture (D): test article for first experiments

Picture (E): transverse movable probe assembly

Picture (F): programmed actuator

Picture (G): test chamber

Picture (H): New test article with higher heating flux capability and improved diagnostics


(C)

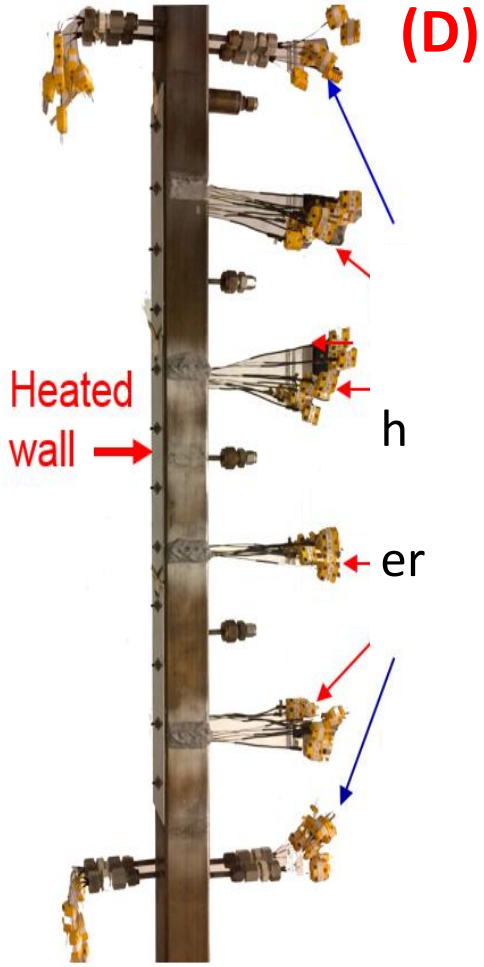
(D)
Heated
wall
h
er

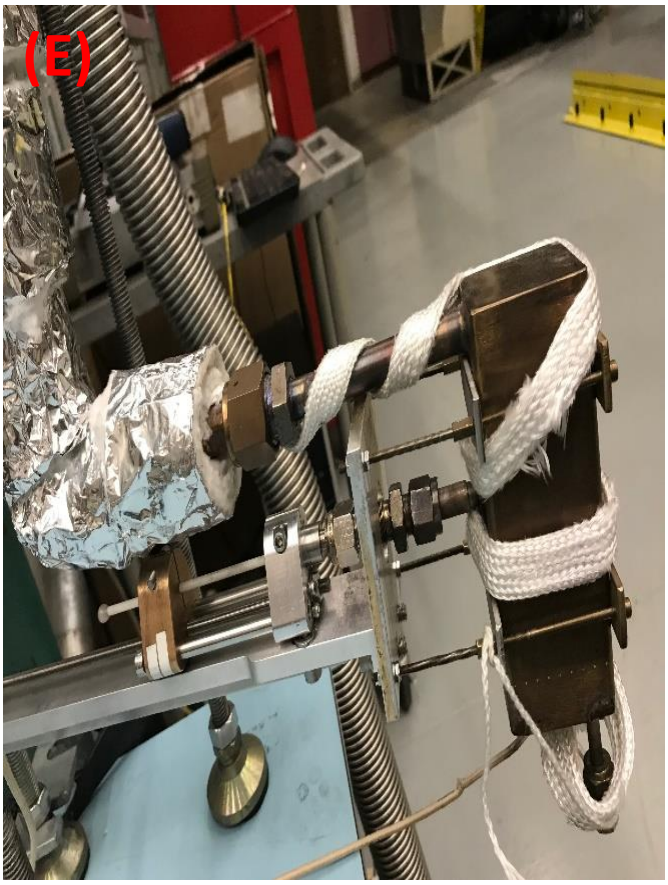
(E)

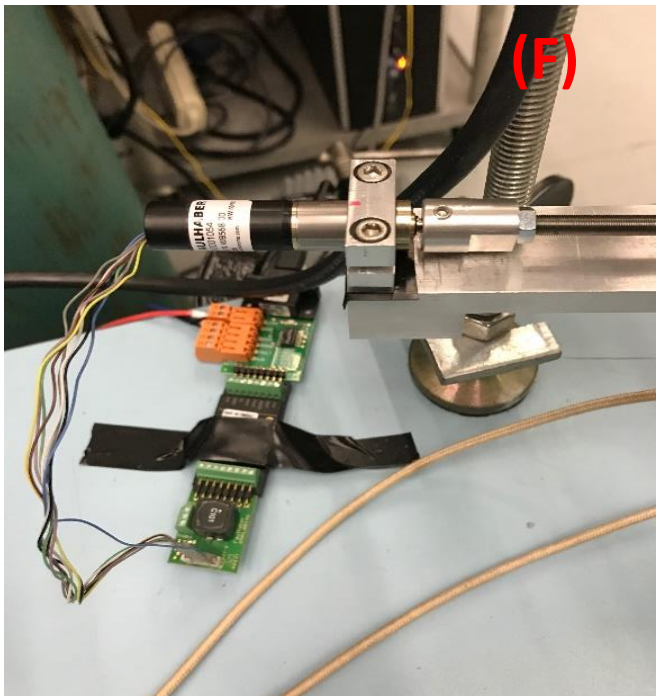
(F)

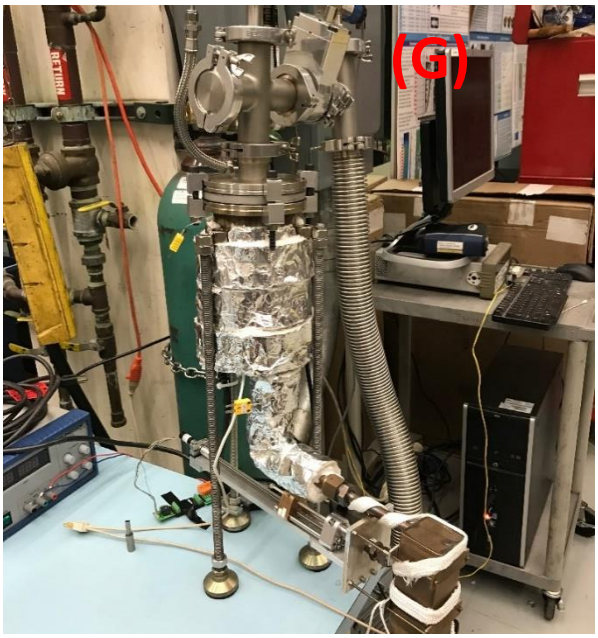
(G)

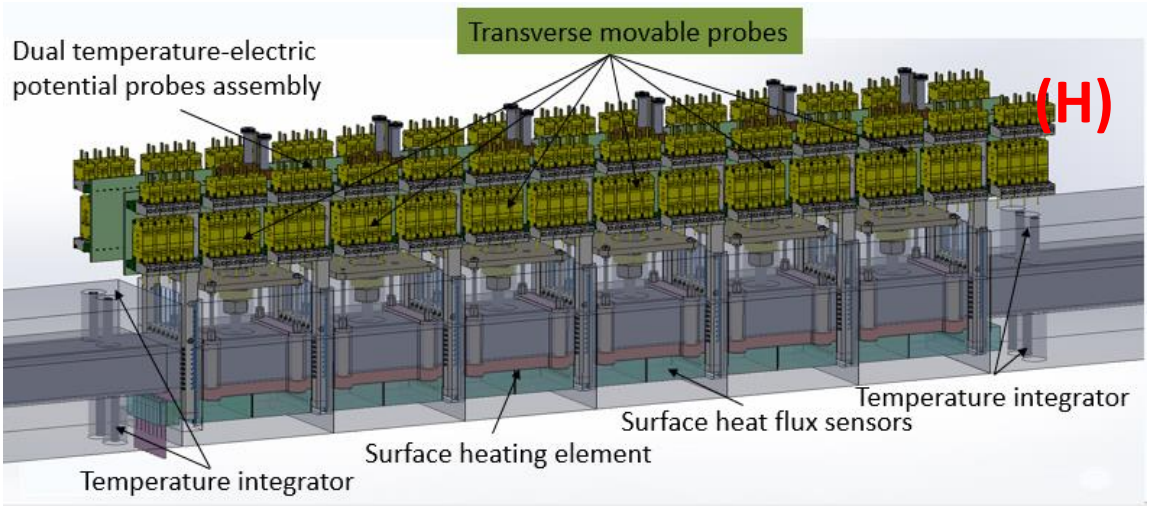
Transverse movable probes
Dual temperature-electric potential probes assembly
(H)
Temperature integrator
Surface heating element
Surface heat flux sensors
Temperature integrator

Appendix B: MaPLE-U First Experiment Results

Chart: Flow regime in different flow operating parameter in first experimental results

Flow Regime	Unidirectional flow	Transitional flow	Reversal flow
Color			

Chart 1: B = 0.00 T (Ha = 0)

q'' / U	2 W/cm² (Gr = 1.43E7)	4 W/cm² (Gr = 2.86E7)	5 W/cm² (Gr = 3.58E7)
1 cm/s (Re = 1015)			
2 cm/s (Re = 2030)			
3 cm/s (Re = 3045)			
4 cm/s (Re = 4060)			
5 cm/s (Re = 5075)			
10 cm/s (Re = 10150)			
15 cm/s (Re = 15225)			

Chart 2: B = 0.53 T (Ha = 234)

q'' / U	2 W/cm² (Gr = 1.43E7)	4 W/cm² (Gr = 2.86E7)	5 W/cm² (Gr = 3.58E7)
1 cm/s (Re = 1015)			
2 cm/s (Re = 2030)			
3 cm/s (Re = 3045)			
4 cm/s (Re = 4060)			
5 cm/s (Re = 5075)			
10 cm/s (Re = 10150)			
15 cm/s (Re = 15225)			

Chart 3: B = 1.00 T (Ha = 440)

q'' / U	2 W/cm² (Gr = 1.43E7)	4 W/cm² (Gr = 2.86E7)	5 W/cm² (Gr = 3.58E7)
1 cm/s (Re = 1015)			
2 cm/s (Re = 2030)			
3 cm/s (Re = 3045)			
4 cm/s (Re = 4060)			
5 cm/s (Re = 5075)			
10 cm/s (Re = 10150)			
15 cm/s (Re = 15225)			

Figure: Time averaged temperature measurements on Hartmann walls at different flow parameters

U=2 cm/s, B=0.53 T, q''=2 W/cm2

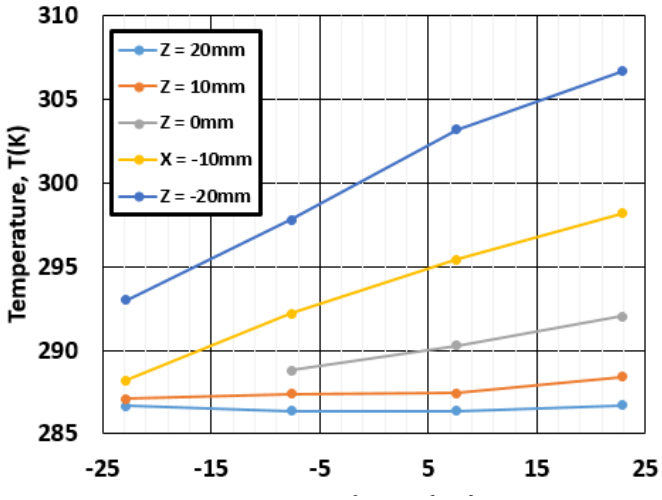

U=1 cm/s, B=0.53 T, q''=2 W/cm2

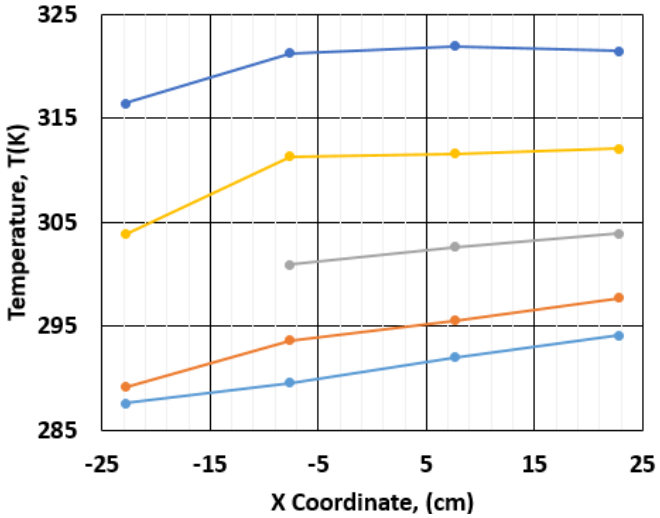

U=1 cm/s, B=0.53 T, q''=4 W/cm2

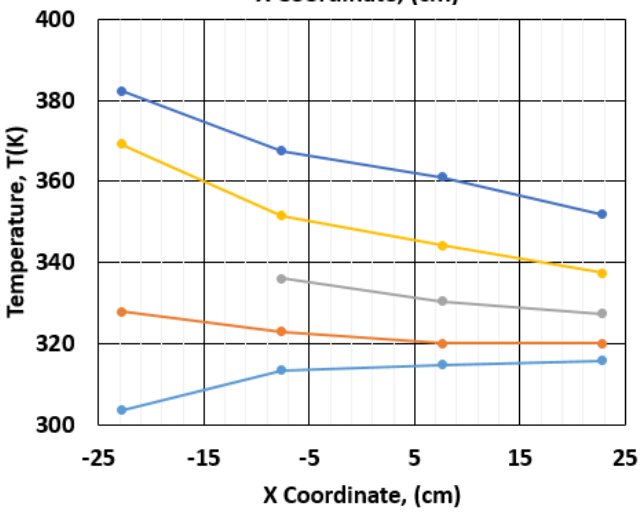

REFERENCES

[1] M. Abdou, N. Morley, S. Smolentsev, et al., "Blanket / First Wall Challenges and Required R & D on the pathway to DEMO," *Fus. Eng. Des.* **100**, 2–43 (2014)

[2] Y. Mori, "On a laminar free-convection flow and heat transfer of electrically conducting fluid on a vertical plate in the presence of a transverse magnetic field," *Trans. Japan Soc. Aero. Space. Sci.* **2**, 22-26 (1959)

[3] E. M. Sparrow, R. D. Cess, "THE EFFECT OF A MAGNETIC FIELD ON FREE CONVECTION HEAT TRANSFER," *Int. J. Heat Mass Transfer.* **3**, 267-274 (1961)

[4] H. K. Yang, C. P. Yu, "COMBINED FORCED AND FREE CONVECTION MHD CHANNEL FLOW IN ENTRANCE REGION," *Int. J. Heat Mass Transfer.* **17**, 681-691 (1974)

[5] I. Michiyoshi, O. Takahashi, A. Serizawa, "Natural Convection Heat Transfer From a Horizontal Cylinder to Mercury Under Magnetic Field," *Int. J. Heat Mass Transfer.* **19**, 1021-1029 (1976)

[6] M. Seki, H. Kawamura, K. Sanokawa, "Natural Convection of Mercury in a Magnetic Field Parallele to the Gravity," *ASME JOURNAL OF HEAT TRANSFER*, **101**, 227-232 (1979)

[7] O. Takahashi, N. Nagase, I. Michiyoshi, N. Takenaka, "Natural Convection Heat Transfer From a Vertical Cylinderical Heaer to Liquid Metals Under Horizontal Magnetic Field," *J. Heat Transfer* **3**, 1317-1322 (1986)

[8] K. Okada, H. Ozoe, "Experimental Heat Transfer Rates of Natural Convection of Molten Gallium Suppressed Under an External Magnetic Field in Either the X, Y, or Z Direction," *ASME JOURNAL OF HEAT TRANSFER*, **114**, 107-114 (1992)

[9] T. Tagawa, H. Ozoe, “Enhancement of Heat Transfer Rate by Application of a Static MAgnetic Field During Natural Convection of Liquid Metal in Cube,” *J. Heat Transfer, 119*, 265-271 (1997)

[10] N. O. Weiss, “Convection in an imposed magnetic field, Part 1. The development of nonlinear convection” *J. Fluid Mech.* **108**, 247-272 (1981)

[11] H. Ozoe, A. Mouri, M. Hiramitsu, S.W. Churchill, N. Lior, “Numerical calculation of three-dimensional turbulent natural convection in a cubical enclosure using a two-equation model for turbuelnce,” *J. Heat Transfer.* **108**, 806-813 (1986)

[12] H. Ozoe, K. Okada, “The effect of the direction of the external magnetic field on the three-dimensional natural convection in a cubical enclosures,” *Int. J. Heat Mass Transfer.* **32**, 1939-1954 (1989)

[13] R. Mößner, U. Müller, “A numerical investigation of three-dimensional magneto-convection in rectangular cavities,” *Int. J. Heat Mass Transfer.* **42**, 1111-1121 (1999)

[14] S. Smolentsev, R. Moreau, M. Abdou, “Study of MHD mixed convection in the DCLL blanket conditions,” *Procedding 7th PAMIR Ineternal Conference*, 81-85 (2008)

[15] G. Sposito, M. Ciofalom, P. A. Di Maio, G. Vella, “Mixed Magnetohydrodynamic Convection in Poloidal Helium Cooled Lithium-Lead Blanket Modules of a Fusion Reactor,” *22nd Congresso Nazionale Sulla Trasmissione Del Calore*, **17**, 21-26 (2004)

[16] N. Vetcha, S. Smolentsev, M Abdou, “Theoretical Study of Mixed Convection in Poloidal Flows of DCLL Blanket,” *Fus. Sci. Tech.,* **56**, 851-855 (2009)

[17] N. Vetcha, S. Smolentsev, M. Abdou, “Stability analysis for buoyancy-opposed flows in poloidal ducts of the DCLL blanket,” *Fus. Sci. Tech.,* **60,** 581-522 (2011)

[18] H. Saleh, I. Hashim, “Flow Reversal of Fully-Developd Mixed MHD Convection in Vertical Channels,” *Chinese Phys. Lett.,* **27**, No.2, (2010)

[19] C. Mistrangelo, L. Bühler, “Numerical Analysis of Buoyant-Convective Liquid Metal Flow in Channels Exposed to Strong Magnetic Fields,” *Procedding 24th Symposium on Fusison Engineering*, 81-85 (2011)

[20] H. Sun, R. Lim E. Chenier, G, Lauriat, “On the modeling of aiding mixed convection in vertical channels,” *Heat Mass Transfer*. **48**, 1125-1134 (2012)

[21] R. Alizadeh, “The Effect Of MHD On Laminar Mixed Convection Of Newtonian Fluid Between Vertical Parallel Plates Channel,” *Advances in Modern Mechanical Engineering*, 146-151 (2013)

[22] A. Gul, I. Khan, S. Shafie, A. Khalid, A. Khan, “Heat transfer in MHD mixed convection flow of a ferrofluid along a vertical channel,” *PLOS one.*, 1-14 (2015)

[23] X. Zhang, O. Zikanov, “Convection instability in a downward flow in a vertical duct with strong transverse magnetic field,” *Physics of Fluids,* **30**, 117101 (2018)

[24] I. A. Melnikov, E. V. Sviridov, V. G. Sviridov, N. G. Razuvanov, “Experimental investigation of MHD heat transfer in a vertical round tube affected by transverse magnetic field,” *Fus. Engi. Des.* **112**, 505-512 (2016)

[25] O. Zikanov, Y. Listratov, “Numerical investigation of MHD heat transfer in a vertical round tube affected by transverse magnetic field,” *Fus. Eng. Des.*, **113**, 151-161 (2016)

[26] I. R. Kirillov, D. M. Obukhov, et al., “Buoyancy effects in vertical rectangular duct with coplanar magnetic field and single sided heat load,” *Fus. Eng. Des.*, **104**, 1-8 (2016)

[27] X. Zhang, O. Zikanov, “Thermal convection in a toroidal duct of a liquid metal blanket. Part I. Effect of poloidal magnetic field,” *Fus. Eng. Des.*, **116**, 52-60 (2016)

[28] X. Zhang, O. Zikanov, “Thermal convection in a toroidal duct of a liquid metal blanket. Part II. Effect of axial mean flow,” *Fus. Eng. Des.*, **116**, 40-46 (2017)

[29] N. Vetcha, S. Smolentsev, M. Abdou, R. Moreau, “Study of instabilities and quasi-two-dimensional turbulence in volumetrically heated magnetohydrodynamic flows in a vertical rectangular duct,” *Physics of Fluids*, **25**, 024102 (2013)

[30] S. Smolentsev, F-C. Li, N. Morley, Y. Ueki, M. Abdou and T. Sketchley, Construction and initial operation of MHD PbLi facility at UCLA, Fusion Engineering and Design 88 (2013) 317-326.

[31] C. Courtessole, S. Smolentsev, T. Sketchely, M. Abdou, “MHD PbLi Experiments in MaPLE Loop at UCLA,” *Fus. Eng. Des.*, vol. 109-111,Part A (2016)

[32] MJ. Ni, R. Ramakanth, N.B. Morley, et al., “A current density conservative scheme for incompressible MHD flows at a low magnetic Reynolds number. Part I: On a rectangular collocated grid system,” *Journal of Computational Physics.*, vol. 227, 174-204 (2007)

[33] G. Federici, L. Boccaccini, F. Cismondi, et al., “An overview of the EU breeding blanket design strategy as an integral part of the DEMO design effort,” *Fus. Eng. Des.*, vol. 141, 30-42 (2019)

[35] S. Smolentsev, S. Badia, R. Bhattacharyay, et al., “An approach to verification and validation of MHD codes for fusion applications,” *Fus. Eng. Des.*, **100**, 6572 (2015)

[36] J. A. Shercliff, , “Steady motion of conducting fluids in pipes under transverse magnetic fields,” *Mathematical Proceedings of the Cambridge Philosophical Society*, **49(1)**, 136-144 (1953)

[37] J. C. R. Hunt, “Magnetohydrodynamics flow in rectangular ducts,” *Journal of Fluid Mechanics*, **21(4)**, 577-590 (1965)

[38] Y. Yan, S. Smolentsev, and M. Abdou, "Vadilation of COMSOL Multiphysics for Magntohydrodynamc (MHD) Flows In Fusion Applications," *COMSOL Conference*, Boston, USA, October 6, 2017

[39] B. F. Picologlou, C. B. Reed, "Experimental investigation of 3-D MHD flows at high Hartmann number and interaction parameter," *IUTAM Symposium on liquid metal MHD*, Riga, USSR, May 16, 1988

[40] C. B. Reed, B. F. Picologlou, T. Q. Hua, J. S. Walker, "Alex results - a comparison of measurements from a round and a rectangular duct with 3-D code predictions," *IEEE 12 Symposium on Fusion Engineering*, Monterey, California, October 12-16, 1987

[41] S. Sahu and R. Bhattacharyay, "Validiaiton of COMSOL code for analyzing liquid metal magnetohydrodynamic flow," *Fusion Engineering and Design*, **127**, 151-159 (2018)

[42] C. Alberghi, L. Candido, R. Testoni, M. Utili, and M. Zucchetti, "Verification and Validation of COMSOL Magnetodydrodynamic Models for Liquid Metal Breeding Blankets Technologies," *Energies*, **14(17)**, 5413 (2021)

[43] R. Munipalli, R. Y. Huang, C. Chandler, C. Rowell, M, Ni, N. Morley, S. Smolentsev, M. Abdou, "Physical Model Development and Benchmarking for MHD Flows in Blanket Design," *A final report for the Phase-II SBIR porject*, (2008)

[44] C. Mistrangelo and L. Bühler, "Magneto-convective instabilities in horizontal cavities," *Physics of Fluids*, **28**, 024104 (2016)

[45] U. Burr, L. Barleon, U. Müller, A. Tsinober, "Turbulent transport of momentum and heat in magnetohydrodynamic rectangular duct flow with strong sidewall jets," *Journal of Fluid Mechanics*, **406**, 247-279, (2000)

[46] L. Bühler, “Laminar buoyant magnetohydrodynamic flow in vertical rectangular ducts,” *Physics of Fluids*, vol. 10, no. 1, pp. 223-236, (1998)

[47] J. C. Umavathi, I. C. Liu, J. P. Kumar, “Fully developed magneto convection flow in a vertical rectanular duct,” *Heat Mass Transfer,* **47,** 1-11 (2011)

[48] G. Sposito, M. Ciofalo, “Fully Developed Mixed Magnetohydrodynamic Convection in a Vertical Square Duct,” *Numerical Heat Transfer*, Part A, **53**, 907-924 (2008)

[49] L. Liu, O. Zikanov, “Elevator mode convection in flows with strong magnetic fields,” *Physics of Fluids*, vol. 27, 044103 (2015)

[50] S. Smolentsev, N. Morley, M. Abdou, S. Malang, “Dual-coolant lead-lithium (DCLL) blanket status and R&D needs,” *Fusion Engineering and Design*, **100**, 44-54 (2015)

[51] S. Smolentsev, T. Rhodes, Y. Yan, A. Tassoune, C. Mistrangelo, L. Bühler, and F. R. Urgorri, “Code-to-Code Comparison for a PbLi Mixed-Convection MHD Flow,” *Fusion Science and Techonoloty*, **76**, 653-669, (2020)

[52] A. Tassone et al., "Recent Progress in the WCLL Breeding Blanket Design for the DEMO Fusion Reactor," *IEEE Transactions on Plasma Science*, **46(5)**, 1446-1457, May 2018, doi: 10.1109/TPS.2017.2786046

[53] Del Nevo, A., Martelli, E., Agostini, P., Arena, P., Bongiovì, G., Caruso, G., & R. Villari, "WCLL breeding blanket design and integration for DEMO 2015: status and perspectives," *Fusion Engineering and Design*, **124**, 682-686, (2017)

[54] L. Bühler, C. Mistrangelo, "MHD flow and heat transfer in model geometries for WCLL blankets," *Fusion Engineering and Design*, **124**, 919-923, (2017)

[55] E. Martelli, A. Del Nevo, P. Arena, "Advancements in DEMO WCLL breeding blanket design and integration," *International Journal of Energy Resource*, **42**, 27-52, (2018)

[56] COMSOL Multiphysics Reference Manual, COMSOL, 2019 Version COMSOL 5.5

[57] I. Tosun, Modeling in Transport Phenomena - a Conceptual Approach, 2nd edition, Elsevier Science, 2007.

[58] L. Bühler, S. Horanyi, "Measurements of time-dependent liquid-metal magnetohydrodynamic flows in a flat rectangular duct," *Fusion Engineering and Design*, **84**, 518-521, (2009)

[59] E. Martelli, G. Caruso, F. Giannetti, and A. Del Nevo "Thermo-hydraulic analysis of EU-Demo Wcll breeding blanket," *Fusion Engineering and Design*, **130**, 48-55, (2018)

[60] P. Martelli, J. DeVan, "Corrosion of ferrous alloys exposed to thermally convective Pb-17 at % Li," *L. Nucl. Mater.* **131–143,** 592-598, (1986)

[61] J. Sannier, M. Broc, T. Flament, et al., "Corrosion of austenitic and martensitic stainless steels in flowing Pb17Li alloy," Fusion Engeering and Design, **14**, 299-307, (1991)

[62] I.E. Sarris, S.C. Kakarantza, et al., "MHD natural convection in a laterally and volumetrically heated square cavity," *Int. J. Heat Mass Transf.* **48,** 3443-3453, (2005)

[63] M. Obayedullah, M.M.K. Chowdhury, "MHD natural convection in a rectangular cavity having internal energy sources with non-uniformly heated bottom wall," *Procedia Eng.* **56,** 76-81, (2013)

[64] M. Kinet, B,Knaepen, and S. Molokov, "Instabilities and Transition Magnetohydrodynamic Flows in Ducts with Electrically Conducting Walls," Phys. Rev. Lett. 103, 154501, (2009)

[65] P.A. Davidson, "An Introduction to Magnetohydrodynamics," Cambridge University Press, 2001.

[66] Y, Yan, A. Ying, and M. Abdou, “Numerical study of magneto-convection flows in a complex prototypical liquid-metal fusion blanket geometry,” *Fusion Engineering and Design*. **159,** 111688 (2020)